



저작자표시-비영리-변경금지 2.0 대한민국

이용자는 아래의 조건을 따르는 경우에 한하여 자유롭게

- 이 저작물을 복제, 배포, 전송, 전시, 공연 및 방송할 수 있습니다.

다음과 같은 조건을 따라야 합니다:



저작자표시. 귀하는 원저작자를 표시하여야 합니다.



비영리. 귀하는 이 저작물을 영리 목적으로 이용할 수 없습니다.



변경금지. 귀하는 이 저작물을 개작, 변형 또는 가공할 수 없습니다.

- 귀하는, 이 저작물의 재이용이나 배포의 경우, 이 저작물에 적용된 이용허락조건을 명확하게 나타내어야 합니다.
- 저작권자로부터 별도의 허가를 받으면 이러한 조건들은 적용되지 않습니다.

저작권법에 따른 이용자의 권리는 위의 내용에 의하여 영향을 받지 않습니다.

이것은 [이용허락규약\(Legal Code\)](#)을 이해하기 쉽게 요약한 것입니다.

[Disclaimer](#)

공학박사 학위논문

Embedded Nanostructures for High-Efficiency  
Organic Light Emitting Devices

나노구조 내장 고효율 유기발광소자

2014 년 2 월

서울대학교 대학원

재료공학부

전 소 희

**Embedded Nanostructures**  
**for High-Efficiency Organic Light Emitting Devices**

나노 구조 내장 고효율 유기 발광 소자  
지도교수 윤 재 루

이 논문을 공학박사 학위논문으로 제출함  
2013년 12월

서울대학교 대학원

재료공학부

전 소 회

전 소 회의 공학박사 학위논문을 인준함  
2013년 12월

위 원 장 \_\_\_\_\_ (인)  
부위원장 \_\_\_\_\_ (인)  
위 원 \_\_\_\_\_ (인)  
위 원 \_\_\_\_\_ (인)  
위 원 \_\_\_\_\_ (인)

**Embedded Nanostructures for High-  
Efficiency Organic Light Emitting Devices**

DISSERTATION

ADVISOR: PROFESSOR JAE RYOUN YOUN

Sohee Jeon

February 2014

Department of Materials Science and Engineering

Graduate School

Seoul National University

# Abstract

Organic light emitting diodes (OLEDs) have been successfully applied to various mobile electronics because the display, which utilizes a spontaneous emission of light from organic molecules by nature, is a very energy efficient way to produce vibrant images. However, only around 20-30% of the light generated by a typical bottom emission OLED is extracted into the air because the light intensity is decreased by a factor of  $1/2n^2$  as the light passes through each layers, where  $n$  is the refractive index (RI).

The light extraction efficiency, which is one of the most important factors, can be enhanced by applying photonic implements to each layer. In this thesis, a nano-hole array (NHA) embedded OLEDs were proposed for light extraction. The NHA structure is proposed as a strategy for escaping the loss mode wasted by the substrate, waveguided and surface plasmon polaritons. Various methods have been proposed to convert the loss modes into the radiation mode, e.g., polymer/Si<sub>3</sub>N<sub>4</sub> nano hole array embedded OLEDs (chapter 3), vacuum/Si<sub>3</sub>N<sub>4</sub> nano hole array embedded OLEDs (chapter 4 and chapter 7), corrugated OLEDs (chapter 5) and their combinations (chapter 6).

The enhanced performance of the nanostructure embedded OLEDs is evaluated by using in terms of photoluminescence (PL) and electroluminescence (EL), and the finite difference time domain (FDTD) simulation was carried out to analyze the optical performance of the NHA structure for extraction of the emission. We explored the effect of the NHA structure on the extraction improvement converted from waveguide mode by measuring EL intensities of the devices with hemisphere lens. The reduction of power dissipation to waveguide and surface plasmon modes by applying the NHA structure leads to strongly enhance the out-coupling efficiency of OLEDs.

Especially the robust reverse transfer process was newly developed for confining the nano hole array in the vacuum state. The periodic nano hole array is inserted in the vacuum state to maximize the refractive index contrast of the PhC slab for a

given background high-refractive index material. In addition, the transfer process employed in VNHA fabrication yielded extremely low surface roughness, and thus outstanding electrical characteristics. We obtained an extremely high efficiency OLEDs with over 50% of external quantum efficiency (EQE) and low roll-off by inserting vacuum nano hole array (VNHA) into phosphorescent OLEDs (PhOLEDs), and it is the highest EQE for bottom-emitting OLEDs.

**Keywords:** Organic Light Emitting Diodes (OLEDs), Light Extraction, Nanostructure, Nanoarray, Photonic Crystals, Finite Difference Time Domain (FDTD), Diffraction Strength, Surface Plasmon Polaritons,

**Student Number:** 2010-30181

## Contents

<b>Abstract</b>	<b>i</b>
<b>List of Figures</b>	<b>vii</b>
<b>List of Tables</b>	<b>xiv</b>
<b>Chapter 1. Introduction</b>	<b>..... 15</b>
1.1 OLED fundamentals	..... 15
1.2 Electroluminescence quantum efficiency	..... 16
1.3 Optical loss modes	..... 22
1.4 Bibliography	..... 25
<b>Chapter 2. Motivation</b>	<b>..... 27</b>

## Part I

### Nano Hole Array Embedded Organic Light Emitting Diodes

---

<b>Chapter 3. Polymer Nanostructure Embedded Organic Light Emitting Diodes</b>	<b>..... 30</b>
3.1 Introduction	..... 30
3.2 Experimental	..... 32
3.2.1 Imprinted polymer nano hole array fabrication	..... 32
3.2.2 Polymer/Si <sub>3</sub> N <sub>4</sub> PhCs slab characterization	..... 32
3.3 Finite Difference Time Domain Simulation	..... 35
3.4 Electroluminescence Performance	..... 37
3.5 Conclusions	..... 40
3.6 Bibliography	..... 40

<b>Chapter 4. Vacuum Nano Hole Array Embedded Organic Light Emitting Diodes: Fluorescent Molecules as an Emitter</b>	<b>42</b>
4.1 Introduction	42
4.2 Experimental	44
4.2.1 VNHA substrate fabrication	44
4.2.2 VNHA OLEDs characterization	48
4.3. FDTD Analysis	48
4.3.1 Effect of the refractive index contrast	48
4.3.2 Emission energy for the three primary colors	50
4.4 Angular Dependence of Photoluminescence	55
4.5 Electroluminescence of VNHA OLEDs	57
4.5.1 Intensified CCD measurement	57
4.5.2 EL intensity of half-sphere lens attaching OLEDs	61
4.5.3 Diffraction pattern induced from substrate modes	61
4.5.4 J-V-L curves of VNHA OLEDs	62
4.6 Conclusions	66
4.7 Bibliography	67

## Part II

### Corrugated Organic Light Emitting Diodes

---

<b>Chapter 5. Corrugated Organic Light Emitting Diodes</b>	<b>70</b>
5.1 Introduction	70
5.2 Experimental	73
5.2.1 Corrugated OLEDs fabrication	73
5.2.2 Characterization of corrugated OLEDs	75
5.3 Electroluminescence Performance	75

5.3.1 J-V-L characteristics of corrugated OLEDs	75
5.3.2 EL enhancement evaluated by intensified CCD	76
5.3.3 Radiation profile of corrugated OLEDs	77
5.3.4 Device stability and life-time	81
5.4 FDTD Analysis	84
5.4.1 FDTD structure for considering Bragg gratings	84
5.4.2 Comparison between theoretical and empirical results	85
5.5 Conclusions	87
5.6 Bibliography	87
<b>Chapter 6. Corrugated OLEDs Embedding Vacuum Nano Hole Array</b>	<b>89</b>
6.1 Introduction	89
6.2 Multiple Nano Patterned Substrate	90
6.2.1 MNHA substrate fabrication	90
6.2.2 MNHA substrate characterization	92
6.3 FDTD Analysis	96
6.3.1 Corrugated OLEDs embedding VNHA	
: Localized surface plasmon at the distorted metal surface	96
6.3.2 Poynting energy depending on the overlay shift	101
6.4 Angular Photoluminescence	105
6.5 Electroluminescence	108
6.5.1 Intensified CCD measurement	108
6.5.2 J-V-L characteristics	113
6.6 Conclusions	116
6.7 Bibliography	116

## Part III

### Ultrahigh-Efficiency OLEDs

---

<b>Chapter 7. Vacuum Nano Hole Array Embedded OLEDs with Ultimate Efficiency: Phosphorescent Molecules as an Emitter</b>	<b>119</b>
7.1 Introduction	119
7.2 Experimental	121
7.2.1 VNHA substrate fabrication	121
7.2.2 VNHA-PhOLEDs fabrication	124
7.2.3 VNHA-PhOLEDs characterization	127
7.3 Mode Analysis by Optical Modeling	127
7.4 Photoluminescence Performance	130
7.4.1 Polarized angular photoluminescence	130
7.4.2 Comparison of PL with dipole orientations	131
7.5 Electroluminescence Performance	133
7.5.1 External quantum efficiency and power efficiency	133
7.5.2 Hemi-sphere attaching VNHA-PhOLEDs	134
7.6 Conclusions	139
7.7 Bibliography	139
<b>Appendix A. VNHA Substrate Characterization Details</b>	<b>142</b>
<b>Appendix B. FDTD Simulation Details</b>	<b>147</b>
<b>Appendix C. Angular PL Measurement Details</b>	<b>154</b>
<b>Appendix D. EL Measurement Set-up</b>	<b>157</b>
<b>Korean Abstract</b>	<b>158</b>

## List of Figures

- Figure 1.1** Schematic diagram of HOMO/LUMO levels of highly efficient OLEDs. The holes and electrons are injected, transported, blocked and then finally recombined at the emission layer. .... 18
- Figure 1.2** The shadow mask used for the deposition of each layer. The active area is defined by the overlap of the anode, organic and the anode layer as depicted by the green area. The PL and EL devices were encapsulated in a dry nitrogen atmosphere using a glass lid and UV cured epoxy edge seal. A CaO desiccant was added inside the package to react with any by-products of the epoxy cure and any residual water or oxygen present within the encapsulated volume. 19
- Figure 1.3** The selection of organic molecules used in this study ..... 20
- Figure 1.4** Schematic diagrams of the parameters determining the external quantum efficiency of OLEDs ..... 21
- Figure 1.5** (a) Schematic illustration of OLEDs showing all optical modes, (b) Various methods have been proposed to convert the waveguide and glass modes into the radiation mode. .... 23
- Figure 1.6** Schematic illustration of OLEDs showing all optical loss modes (a) With hemisphere lens, the glass mode is directly emitted to air as shown in right part of the figure, and (b) the nanostructure inserting to between substrate and transparent conductive oxide (TCO) electrode can scatter the light emitted under angles larger than the critical angle of the interface of TCO and substrate..... 24
- Figure 3.1** Schematic diagram of the UV-nanoimprint lithography procedure for the direct fabricating of a polymer pillar substrate ..... 31
- Figure 3.2** (a) Vertical structure and materials of OLED, (b) SEM image of the imprinted polymer pillars. The pillar array is hexagonal lattice and its lattice constant and diameter are 530 nm and 265 nm, respectively (c) Top view of the PhC slab. The surface of PhC slab is honeycomb

	shape because buffer layer is deposited on a hexagonal lattice pillar.	
	(d) Cross-sectional view of the PhC slab. The polymer pillars in the PhC slab can be observed.	..... 34
<b>Figure 3.3</b>	FDTD simulation results with variation in the glass thickness..	36
<b>Figure 3.4</b>	(a) Radiation profile represented in terms of luminance efficiency ( $\text{cd A}^{-1}$ ), (b) EL intensity using integrating sphere measurement.	..... 38
<b>Figure 3.5</b>	(a) The light-output power from the OLEDs with and without the PhC, (b) J-V characteristics	..... 39
<b>Figure 4.1</b>	(a) Schematic diagram for fabrication of the 2D nano-hole array with $\text{Si}_3\text{N}_4$ as the high-index material and the novel process used in this fabrication is called $\text{R}^2\text{T}$ , (b) scanning transmission electron microscopy (STEM) image of the NHA substrate fabricated by $\text{R}^2\text{T}$ process, and (c) vertical structure of the NHA-OLED	..... 46
<b>Figure 4.2</b>	Illustration of a standard Cartesian Yee Cell used for FDTD, about which electric and magnetic field vector components are distributed.	..... 51
<b>Figure 4.3</b>	(a) Boundary conditions, (b) FDTD structure used for optical simulations	..... 52
<b>Figure 4.4</b>	FDTD analysis results: (a) Different PhC substrates were modeled by varying the RI contrast ( $n_1/n_2$ ) for a given background material ( $\text{Si}_3\text{N}_4$ , $n_2=2.02$ ). (b) Enhancement of the emission energy was estimated for three different wavelengths of the primary colors when the NHA structure was inserted. (c) Contours of Poynting energy emitted from $d_x$ , $d_y$ , and $d_z$ dipoles on the bare (control), 1.5/2.02 PhC array, and 1.0/2.02 PhC array substrate devices. .	53
<b>Figure 4.5</b>	PL intensity measured as a function of the viewing angle for (a) the p-polarized and (b) the s-polarized light emission with the wavelength of 520 nm.	..... 56

<b>Figure 4.6</b>	(a) EL intensity measured for each device as a function of wavelength, (b) The enhancement factor and Snapshot of the emission from (c) the control OLED (bare glass) is shown and that from (d) the NHA-OLED is provided. Snapshot of the emission from the NHA-OLED with the hemisphere lens attached is shown in (e). .....	58
<b>Figure 4.7</b>	(a) J-L curves of the OLEDs on the bare glass and on the NHA substrate, Inset: Far field radiation profiles of the reference and the NHA-OLEDs, (b) EL intensity contours of the reference and NHA-OLEDs depending upon the wavelength and the viewing angle, (c) J-V curves of the OLEDs on the bare glass and on the NHA substrate with angstrom level roughness, (d) J-V curve of the OLED fabricated on the polymer nanoarray (PNA)/Si <sub>3</sub> N <sub>4</sub> substrate that were covered by the successive planarization layer using PECVD. ....	64
<b>Figure 5.1</b>	Fabrication process of corrugated OLEDs .....	72
<b>Figure 5.2</b>	SEM image of one of the stamps used in the UV-NIL process (a), and DB-FIB images of the cross-sections of fabricated corrugated OLED samples with (b) 15 nm corrugation depth, (c) 50 nm corrugation depth, (d) 65 nm corrugation depth, (e) 80 nm corrugation depth and (f) 100 nm corrugation depth .....	74
<b>Figure 5.3</b>	Voltage-current characteristics of the corrugated OLEDs with different corrugation depths .....	78
<b>Figure 5.4</b>	(a) Light-output power versus current density, (b) light-output power versus electrical input power density and (c) The relative extraction efficiencies with respect to corrugation depth normalized to the OLEDs without pillars .....	79
<b>Figure 5.5</b>	The angular emission characteristics of OLEDs with (a) planar and (b) 50 nm corrugated substrates, (c) The radiation profiles normalized by the EL intensity of reference device in the normal	

	direction and (d) photographs of the reference OLED and corrugated OLEDs with pillar heights of 50 nm and 100 nm....	82
<b>Figure 5.6</b>	FDTD simulated relative light extraction efficiency versus the corrugation depth for three different structures shown in inset.	86
<b>Figure 6.1</b>	(a) A schematic diagram for fabrication of the multiple nano hole array (MNHA) OLED using the R <sup>2</sup> T and following nano-patterning process, (b) Focused Ion Beam (FIB) images of the MNHA on a glass substrate, (c) cross sectional image of the MNHA embedded OLED (MNHA-OLED) along the line A-A', and (d) cross sectional image of the MNHA-OLED along the line B-B'.	93
<b>Figure 6.2</b>	3D graph of FDTD simulated integrated Poynting energies depending to the substrate	98
<b>Figure 6.3</b>	Contours of electric field intensities induced from the dipoles according to their relative distance from the metal pattern.....	99
<b>Figure 6.4</b>	FDTD results (a) in the case of no metal mirror and (b) in the case of corrugated metal mirror	100
<b>Figure 6.5</b>	Integrated Poynting energy simulated by FDTD analysis according to overlay shift: (a) Eclipsed and (b) staggered positions	101
<b>Figure 6.6</b>	Integrated Poynting energy simulated by FDTD analysis according to overlay shift. Eclipsed/ Staggered/ Mismatched positions	102
<b>Figure 6.7</b>	FDTD analysis results: Integrated Poynting energies according to different dipole positions in the different MNHA substrates modeled by varying the overlay shift between CNA and VNHA	103
<b>Figure 6.8</b>	FDTD analysis results: (a) Integrated Poynting energies according to different dipole positions in the different MNHA substrates modeled by varying the overlay shift between CNA and VNHA.	

	.....104
<b>Figure 6.9</b>	P-polarized angular PL intensity measured as a function of the viewing angle: (a) Corrugated VNHA substrate and (b) comparison with the VNHA and corrugated VNHA substrate .106
<b>Figure 6.10</b>	S-polarized angular PL intensity measured as a function of the viewing angle: (a) Corrugated VNHA substrate and (b) comparison with the VNHA and corrugated VNHA substrate .107
<b>Figure 6.11</b>	The EL intensity measured for each device as a function of wavelength: (a) the EL intensity of the OLEDs measured using an integrating sphere, (b) The EL intensity was also measured for each device by attaching a 10 mm hemisphere lens to the OLEDs .....110
<b>Figure 6.12</b>	All of EL intensities measured at $5\text{mA}/\text{cm}^2$ are represented in one graph for comparison. ....111
<b>Figure 6.13</b>	(a) J-L curves of the OLEDs on the bare glass and on the NHA and MNHA substrates, (b) J-V curves of the OLEDs on the bare glass and on the NHA and MNHA substrates .....114
<b>Figure 6.14</b>	EL intensity contours of (a) the reference, (b) NHA-OLED and (c) MNHA-OLED depending upon the wavelength and the viewing angle .....115
<b>Figure 7.1</b>	Schematic diagram for fabrication of the 2D nano-hole array with $\text{Si}_3\text{N}_4$ as the high-index material and the novel process used in this fabrication is called R <sup>2</sup> T. ....123
<b>Figure 7.2</b>	Device structure and the energy level of the OLEDs .....125
<b>Figure 7.3</b>	Focused Ion Beam (FIB) images of the VNHA substrate fabricated by R <sup>2</sup> T process and vertical structure of the VNHA-PhOLEDs .....126
<b>Figure 7.4</b>	The mode analysis of exciplex forming co-host phosphorescent OLEDs. The power coupling ratio simulated using the classical dipole model for the bottom emission. ....129

<b>Figure 7.5</b>	PL intensity measured as a function of the viewing angle for (a) the p-polarized and (b) the s-polarized light emission with the wavelength of 520 nm	.....132
<b>Figure 7.6</b>	(a) External quantum efficiencies (Inset: angular dependent emission), (b) power efficiencies of reference and VNHA PhOLEDs, (c) EL intensity measured for each device as a function of wavelength and (d) EL intensity measured at the different current densities of 0.5, 1.0, 2.0 and 5.0 mA/cm <sup>2</sup> .	.....135
<b>Figure A.1</b>	SEM images of (a) the nano-hole array substrate: The trapped low vacuum state was periodically arranged by R <sup>2</sup> T process. (b) OLEDs integrated on the NHA substrate, (c) and (d) The Si <sub>3</sub> N <sub>4</sub> /polymer nanoarray (PNA) substrate: The 500 nm (c) and 800 nm (d) planarized dielectric material (Si <sub>3</sub> N <sub>4</sub> ) deposited using PECVD.	.....143
<b>Figure A.2</b>	The photographs (a) after anodic bonding and (b) after removing silicon by dipping KOH solution: The periodic hole is defined over 100×100 mm <sup>2</sup> on 8-inch silicon wafer and (c) Fully patterned wafer in order to increase the number of samples.	.....144
<b>Figure A.3</b>	AFM images of the NHA substrates; the roughness data of several NHA substrates are summarized in the table below.	.....145
<b>Figure A.4</b>	AFM images of (a) the PNA substrates and (b) an electrode surface after sputtering 150 nm-thick ITO layers on the PNA substrates; the roughness data for the PNA substrates and for the electrode on the PNA substrates are summarized in the table below.	.....146
<b>Figure B.1</b>	A unit cell of a hexagonal nanostructure. The integrated Poynting energy was estimated according to the position of dipoles.	.....149
<b>Figure B.2</b>	FDTD analysis according to the lattice constants for green (a), blue (b), and red (c); all of the results are shown in one graph (d).	.....151

<b>Figure B.3</b>	FDTD results of the combination of flat /corrugated organic layer and flat/corrugated metal mirrors	.....152
<b>Figure B.4</b>	Summary of the FDTD results	.....153
<b>Figure C.1</b>	(a) Schematic diagram and (b) photograph of the angle dependent PL measurement set-up	.....156

## List of Tables

<b>Table 4.1</b>	EL enhancement values for different wavelength ranges. The EL enhancement is coupled with the radiation modes converting from both the waveguide loss and the glass loss modes. ....	60
<b>Table 5.1</b>	EL enhancement values for different wavelength ranges .....	112
<b>Table 7.1</b>	EL enhancement values and EQEs for different wavelength ranges .....	138
<b>Table B.1</b>	Classification for FDTD analysis according to the combination of flat /corrugated organic layer and no/flat/corrugated metal mirrors .....	151

# Chapter 1

## Introduction

---

Organic light emitting diodes (OLEDs) have been successfully applied to various mobile electronics because the display, which utilizes a spontaneous emission of light from organic molecules by nature, is a very energy efficient way to produce vibrant images. The first thin film OLEDs was demonstrated by researchers at Eastman Kodak in 1987 using vacuum-deposited small-molecule organic materials and by a group at Cambridge University in 1990 using a solution processed conjugated polymer.<sup>1 2</sup> OLEDs intrinsically provide high energy efficiency compared with other light sources. Inspired by these publications, intense research has been lead to steady improvements in efficiency and life time. Recently, the commercialization of OLEDs for general lighting source has just started.

### 1.1. OLED Fundamentals

As the most primary structure, OLEDs composed of one organic molecule as an emission layer, sandwiched between two electrodes, i.e., the anode and the cathode. However, for more effective operation, OLEDs can consist of several additional layers which have different functional materials. A typical stack of multi layered OLEDs is **figure 1.1**. Mostly, the anode consists of indium tin oxide (ITO) and indium zinc oxide (IZO), which has high transmittance over the range of visible

wavelength and shows a good electrical conductivity. As the counterpart, low work function metals or metal alloy like lithium fluoride doped aluminum (LiF/Al), silver (Ag) and silver/magnesium (Ag/Mg) are generally used for the cathode. In order to effectively inject charges from electrode to the emission layer, the hole transport layer (HTL) and electron transport layer (ETL) are inserted adjacent to the anode and cathode. The emission layer (EML) consists of one or more layers and their combinations. According to the energy band gap between the highest occupied molecular orbital (HOMO) and the lowest unoccupied molecular orbital (LUMO) energy level of organic molecules, the emission wavelength is determined.

Meanwhile, the shadow masks used for the deposition of each layer are illustrated in **figure 1.2**. The active area is defined by the overlap of the anode, organic layers and cathode as depicted by the green color. The four corners in the anode overlap with the cathode are applied a voltage by electrical contacts to the OLEDs. The selection of organic molecules used in this article is represented in **figure 1.3**.

## 1.2. Electroluminescence Quantum Efficiency

The most critical characterizing parameter of an OLED is the external quantum efficiency (EQE) which describes the ratio between the number of emitted photons and injected charge carriers.<sup>3</sup> The EQE of OLED are determined by following equation (1).<sup>3,4 5</sup>

$$\eta_{\text{EQE}} = \eta_{\text{int}} \times \eta_{\text{ext}} = \gamma \times \eta_{\text{S/T}} \times q_{\text{eff}} \times \eta_{\text{ext}} \quad (1)$$

Therein  $\gamma$  is the charge carrier balance factor, indicating whether equal amounts of electrons and holes are injected or not and their fraction of recombination of exciton. The  $\eta_{\text{S/T}}$  gives the fraction of excitons that is allowed to decay radiatively by spin statistics. The  $q_{\text{eff}}$  term indicates how many of the spin-allowed excitons actually do decay by emitting a photon. The last term  $\eta_{\text{ext}}$  determines which

fractions of the generated photons are in the end able to leave the device to the air. Accordingly, the external quantum efficiency is split into an internal quantum efficiency (IQE), that is  $\eta_{IQE} = \gamma \times \eta_{S/T} \times q_{eff}$  as indicated in Eq. (1). The efficiency of OLED is determined by complicated physics, and all terms consisting of the equation affect each other because the generated light of OLEDs is obtained by the behavior of electron in the device.<sup>6,7</sup> The schematic diagram is shown in **figure 1.4** which describes factors consisting of EQE.

The EQE of OLED has been significantly increased by phosphorescent emitters and charge transport materials and their vertical arrangement in device designing to realize nearly 100% charge balance. In this case, it is possible to realize that highly efficient OLED realizes with external quantum efficiency (EQE) of over 29% without any extra structures for light extraction.<sup>8,9</sup> In other words, the IQE of OLEDs can be brought up towards the theoretical limit of 100%. However, only a fraction of 20-30% light in the end is able to leave the device to the air. The other lights are wasted by the region of the OLED stack with higher refractive index than air including anode, substrate and emitted organic layers. A simple ray optics model predicts the light out-coupling efficiency in given by following equation.<sup>10</sup>

$$\eta_{out} = 1/2n^2 \quad (2)$$

where  $n$  denotes the refractive index of the organic, anode and substrate layers. By the generated light passing through the layers, the light is attenuated and only 20% of the light power is actually extracted to the air. However, this is only be taken as a rough estimation, a more sophisticated analysis has to take the coupling of the excited molecules to the modes of the OLED into account, as will be discussed in detail in FDTD sections of main chapters.

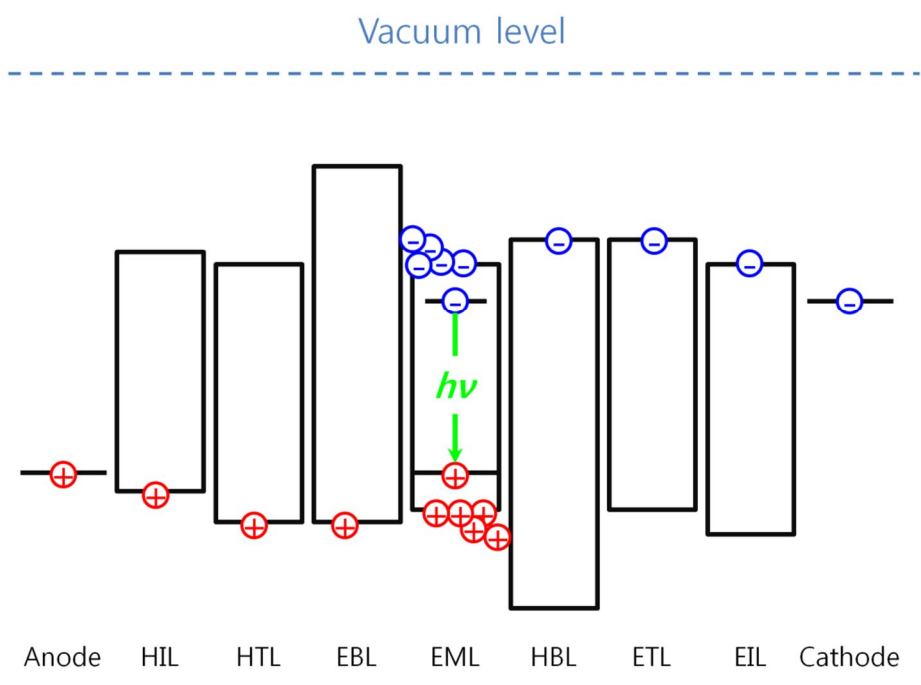
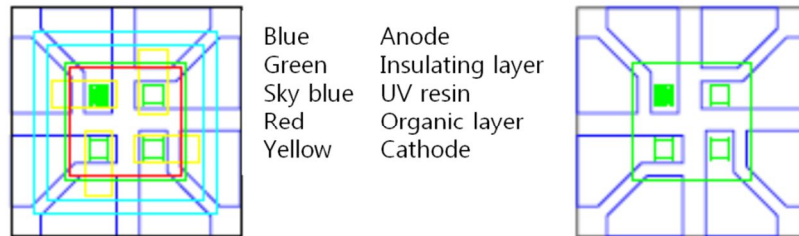


**Figure 1.1.** Schematic diagram of HOMO/LUMO levels of a highly efficient OLED. The holes and electrons are injected, transported, blocked and then finally recombined at the emission layer. <sup>11</sup>

Seoul National University  
25X25 mm<sup>2</sup> Patterned Anode with Insulating layer



20X20 mm<sup>2</sup> Glass Encapsulation

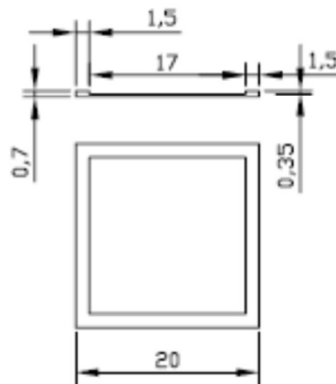


**Figure 1.2.** The shadow mask used for the deposition of each layer. The active area is defined by the overlap of the anode, organic and the anode layer as depicted by the green area. The PL and EL devices were encapsulated in a dry nitrogen atmosphere using a glass lid and UV cured epoxy edge seal. A CaO desiccant was added inside the package to react with any by-products of the epoxy cure and any residual water or oxygen present within the encapsulated volume.

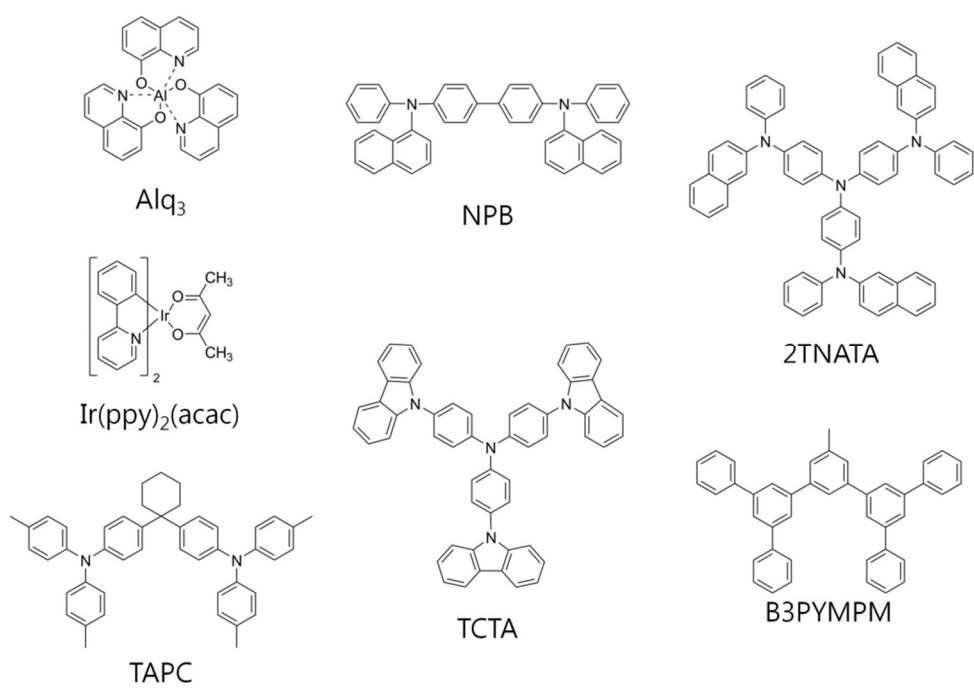


**Figure 1.3.** The selection of organic molecules used in this thesis.

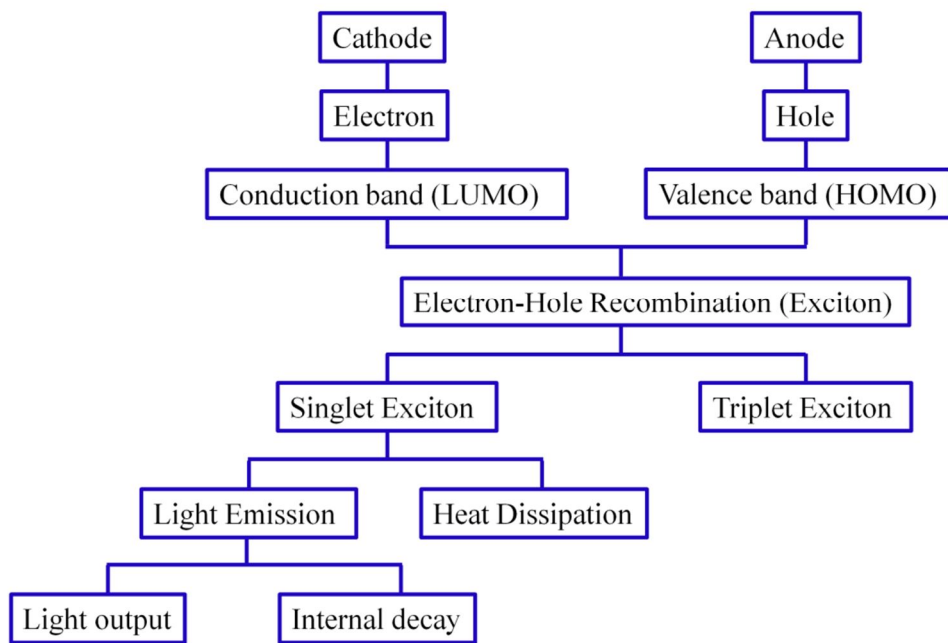


**Figure 1.4.** Schematic diagram of the parameters determining the efficiency of OLEDs.

### 1.3. Optical Loss Modes

As aforementioned, the internal quantum efficiency of OLEDs can be reached to the theoretical limit of 100%. However, the 70% of the internal light is still wasted by the substrate, organic layers and the transparent electrode even in the case of the highest EQE of 30% corresponding to the internal efficiency of 100%. Hence, OLEDs have the potential to enhance the efficiency which can lead to common uses such as general lighting.

On the other hand, the loss modes can convert into the air by photonic implement inside/outside of OLEDs. Various methods have been proposed to convert the waveguide and glass modes into the radiation mode, e.g., textured surfaces,<sup>12,13</sup> microlens arrays,<sup>14-16</sup> scattering medium,<sup>17</sup> Bragg gratings<sup>18,19</sup> and low-index grids,<sup>20</sup> and thus the extraction efficiency has been improved continuously. In general, the loss by glass substrate can be extracted by modifying glass surface, and the waveguide loss can be extracted by inserting a structure between glass and transparent anode.

The main reason of optical losses arises from total internal reflection due to the high refractive index of the organic layers, transparent electrode and substrate, as illustrated in **figure 1.5a**. In general, the generated light from excited dipoles wasted at the interface I, II and III. By modifying the interfaces of inside and outside of the device, the loss modes can be converted the waveguide and glass modes into the radiation mode as shown in **figure 1.5b**.

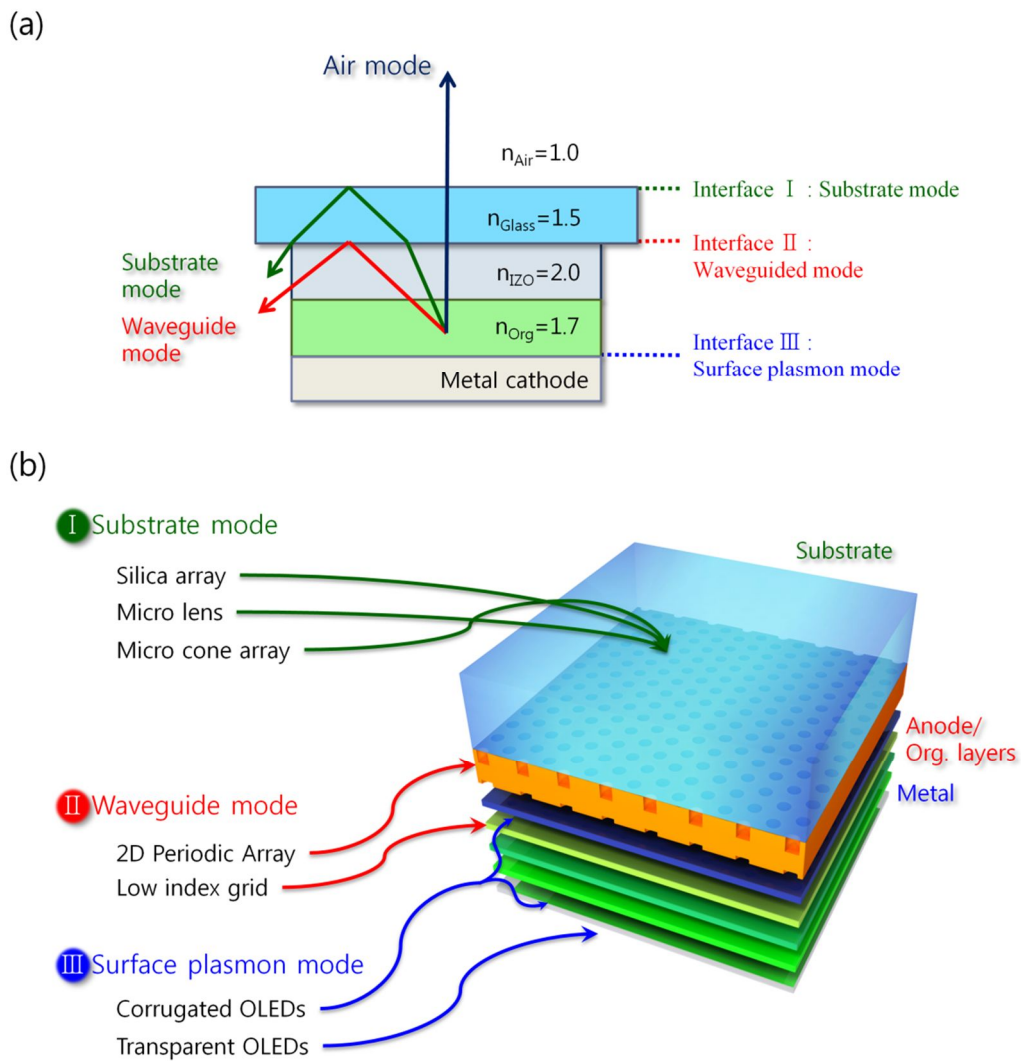


**Figure 1.5.** (a) Schematic illustration of OLEDs showing all optical modes. (b) Various methods have been proposed to convert the waveguide and glass modes into the radiation mode. The loss by glass substrate can be extracted by modifying glass surface, and the waveguide loss can be extracted by inserting a structure between glass and transparent anode.

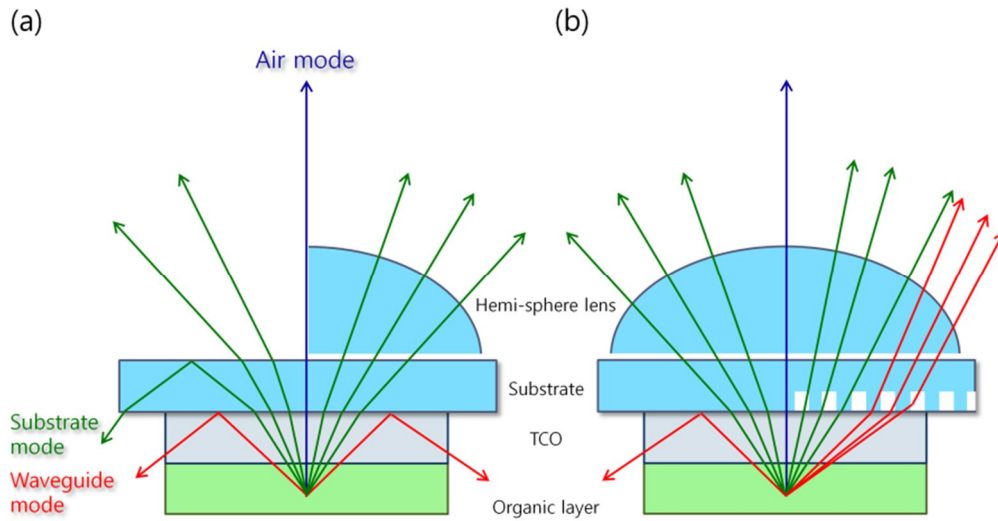


**Figure 1.6.** Schematic illustration of OLEDs showing all optical loss modes. (a) With hemispherical lens, the glass mode is directly emitted to air as shown in right part of the figure, and (b) the nanostructure inserting to between substrate and transparent conductive oxide (TCO) electrode can scatter the light emitted under angles larger than the critical angle of the interface of TCO and substrate.

## 1.4. Bibliography

1. C. W. Tang and S. A. Vanslyke, *Appl Phys Lett*, 1987, **51**, 913-915.
2. J. H. Burroughes, D. D. C. Bradley, A. R. Brown, R. N. Marks, K. Mackay, R. H. Friend, P. L. Burns and A. B. Holmes, *Nature*, 1990, **347**, 539-541.
3. T. Tsutsui, E. Aminaka, C. P. Lin and D. U. Kim, *Philosophical Transactions of the Royal Society a-Mathematical Physical and Engineering Sciences*, 1997, **355**, 801-813.
4. W. Brütting, J. Frischeisen, T. D. Schmidt, B. J. Scholz and C. Mayr, *physica status solidi (a)*, 2013, **210**, 44-65.
5. M. Furno, R. Meerheim, S. Hofmann, B. Lussem and K. Leo, *Physical Review B*, 2012, **85**, 115205.
6. E. M. Purcell, *Physical Review*, 1946, **69**, 681-681.
7. S. H. Fan, P. R. Villeneuve, J. D. Joannopoulos and E. F. Schubert, *Physical Review Letters*, 1997, **78**, 3294-3297.
8. D. Tanaka, H. Sasabe, Y.-J. Li, S.-J. Su, T. Takeda and J. Kido, *Japanese Journal of Applied Physics*, 2007, **46**, L10-L12.
9. M. G. Helander, Z. B. Wang, J. Qiu, M. T. Greiner, D. P. Puzzo, Z. W. Liu and Z. H. Lu, *Science*, 2011, **332**, 944-947.
10. N. C. Greenham, R. H. Friend and D. D. C. Bradley, *Advanced Materials*, 1994, **6**, 491-494.
11. J. Frischeisen, PhD, University of Augsburg, 2011.
12. J. Zhou, N. Ai, L. Wang, H. Zheng, C. Luo, Z. Jiang, S. Yu, Y. Cao and J. Wang, *Org Electron*, 2011, **12**, 648-653.
13. Y. H. Cheng, J. L. Wu, C. H. Cheng, K. C. Syao and M. C. M. Lee, *Appl Phys Lett*, 2007, **90**, 091102.
14. J. Lim, S. S. Oh, D. Y. Kim, S. H. Cho, I. T. Kim, S. H. Han, H. Takezoe, E. H. Choi, G. S. Cho, Y. H. Seo, S. O. Kang and B. Park, *Optics*

- Express*, 2006, **14**, 6564-6571.
15. Y. Sun and S. R. Forrest, *J Appl Phys*, 2006, **100**, 073106.
  16. J.-B. Kim, J.-H. Lee, C.-K. Moon, S.-Y. Kim and J.-J. Kim, *Advanced Materials*, 2013, **25**, 3571-3577.
  17. R. Bathelt, D. Buchhauser, C. Gärditz, R. Paetzold and P. Wellmann, *Org Electron*, 2007, **8**, 293-299.
  18. J. H. Jang, M. C. Oh, T. H. Yoon and J. C. Kim, *Appl Phys Lett*, 2010, **97**, 123302.
  19. A. O. Altun, S. Jeon, J. Shim, J.-H. Jeong, D.-G. Choi, K.-D. Kim, J.-H. Choi, S.-W. Lee, E.-S. Lee, H.-D. Park, J. R. Youn, J.-J. Kim, Y.-H. Lee and J.-W. Kang, *Organic Electronics*, 2010, **11**, 711-716.
  20. Y. Sun and S. R. Forrest, *Nature Photonics*, 2008, **2**, 483-487.

# Chapter 2

## Motivation

---

The reduction of power dissipation to substrate, waveguide and surface plasmon modes will be the major topics of this work. Several novel techniques will be proposed and analyzed theoretically and empirically regarding light extraction in OLEDs. Fundamental discussions of light extraction strategies and of the fundamental physics behind each approach will be proposed and compared by means of photoluminescence, electroluminescence and theoretical simulation. In detail, this thesis is organized in the following chapters:

**Chapter 3.** The polymer nano array (PNA) embedded OLEDs is demonstrated. An etchless simple method was developed to fabricate two-dimensional nanostructures on glass substrate directly by using ultraviolet (UV) curable polymer resin and UV nanoimprint lithography in order to improve output coupling efficiency of OLEDs. The enhancement of the light extraction was predicted by the three-dimensional finite difference time domain method.

**Chapter 4.** The diffraction strength of inserted nanostructure is maximized. Vacuum nano-hole arrays (NHA) were embedded to the sub-nano scale planarized substrate to maximize RI contrast for the given background material,  $\text{Si}_3\text{N}_4$  ( $n_{\text{high}}=2.02$ ). Low vacuum nano-holes ( $n_{\text{low}}=1$ ) were generated periodically over the  $xy$ -plane and 2D PhCs were inserted into OLEDs in order to extract the light trapped in the waveguide mode into the air without any change of electrical

properties. In addition, it was demonstrated by the FDTD simulation and experiments that the inserted NHA was efficient for extraction of the propagating light generated from both the vertical (as expected) and horizontal dipoles, which means that the NHA structure affects not only the waveguide mode but also the glass mode.

**Chapter 5.** Corrugated OLEDs fabricated on polymer based photonic crystals to enhance the light extraction. The photonic crystals are fabricated using ultraviolet nano imprint lithography (UV-NIL) process at room-temperature and low-pressure. Improvement of the efficiency in the corrugated OLEDs is achieved due to the coupling of the PhC effect on the polymer, anode and organic layers and the Bragg reflection effect by the corrugated metallic mirror. The corrugated OLEDs with various PhC heights are fabricated and evaluated. FDTD calculation is carried out to understand the contribution of the coupling to PhC and the reflection from the corrugated metallic mirror to light extraction.

**Chapter 6.** Corrugated OLED embedding vacuum nano hole array is demonstrated. The multiple nano hole array patterned (MNHA) substrate is designed to maximize the light extraction by reducing the light loss wasted by substrate mode, waveguide mode and surface plasmon polaritons. The periodic patterned metal mirror contributes the light extraction by acting as Bragg reflector, and the pattern depth of the metal hole is set to be several 10 nm scale in order to maintain the electrical stability during operation of the device.

**Chapter 7.** Extremely high efficiency OLEDs with over 50% of EQE is demonstrated by inserting vacuum nano hole array (VNHA) into phosphorescent OLEDs (PhOLEDs) with ultimate efficiency and low roll-off. The extraction enhancement obtained from the implement is quantified exactly in terms of EQE by comparing with the result of the optical modeling analysis due to the almost perfect electric characteristics of the device.

# **Part I**

## Nano Hole Array Embedded Organic Light Emitting Diodes

# Chapter 3

## Polymer Nano Array Embedded OLEDs

---

### 3.1. Introduction

Light extraction efficiency of a normal bottom emission OLED is limited to approximately 20 % and 80% because the emitted light is trapped in the waveguide and glass modes.<sup>1-2</sup> Light extraction from OLEDs becomes the most serious factor limiting the overall efficiency of OLEDs for displays and solid state lighting. There have been many efforts to improve the output coupling efficiency of OLEDs by modifying the substrate surface.<sup>3-11</sup> Recently, two-dimensional (2D) slab photonic crystal (PhC) structures had been used and the output coupling efficiency was enhanced by more than 50%.<sup>12-16</sup> One of the difficulties in the 2D slab PhC is the complicated and expensive process, since photolithography including holographic interference patterning followed by an etching process is frequently used to fabricate the PhC structure on a glass substrate. Nano-imprint lithography (NIL) process is an attractive method to replace the expensive photolithography and etching process for fabrication of nano scale photonic crystals.<sup>17</sup> It has been applied to direct fabrication of a PhC structure in a glass substrate by using a so called “hot embossing” technique, where high pressure of about 20 bar and high temperature of about 300°C are required.<sup>16</sup> A simple and cost-effective PhC patterning method is still needed to achieve high manufacturing throughput in the atmosphere.

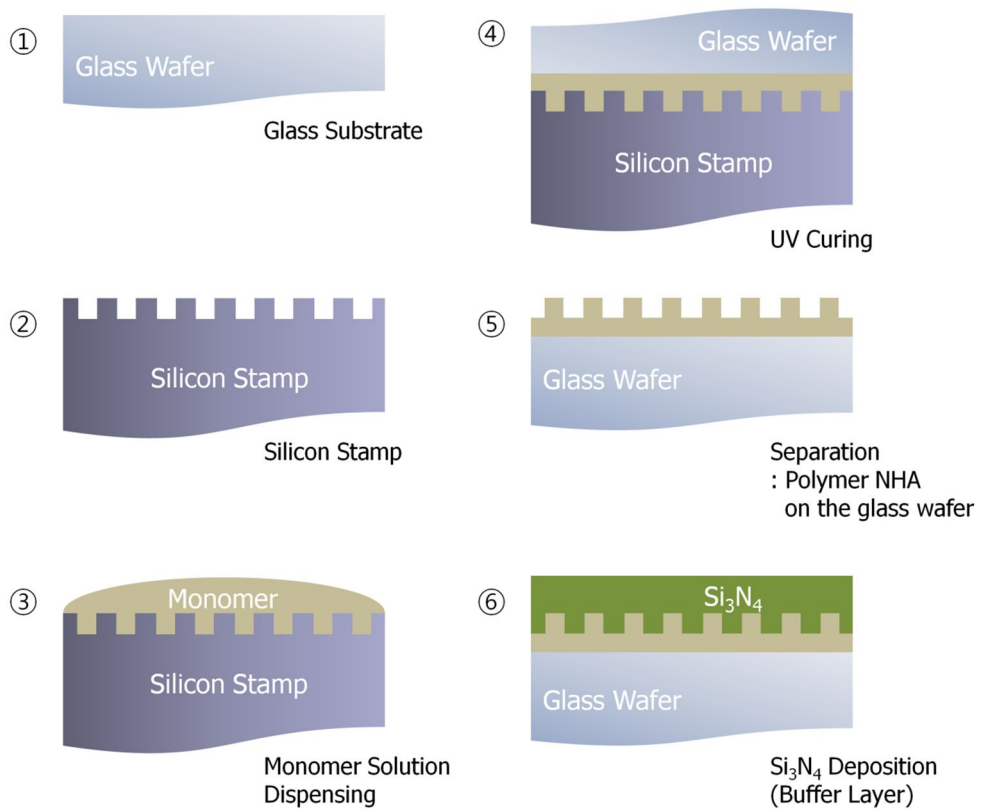


**Figure 3.1.** Schematic diagram of the UV-nanoimprint lithography procedure for the direct fabricating of a polymer pillar substrate.

## **3.2. Experimental**

### **3.2.1. Imprinted polymer nano array fabrication**

The UV-NIL process for the direct patterning of polymer pillars is depicted in **Figure 3.1**. Surface of the stamp was coated by a self-assembled monolayer of trichloro-(1H,1H,2H,2H-perfluorooctyl) silane (FOTS) for easy separation of the polymer resin after curing. A small amount of 60 micro-liters of a UV curable resin was dispensed onto the Si stamp and a glass wafer was placed on it and finally cured by UV exposure for 3 minutes with an illumination power of  $14.4 \text{ mW} \cdot \text{cm}^{-2}$ . The UV curable resin is composed of two monomers, tri(propylene glycol) diacrylate (Aldrich) and tri(methylol) propane triacrylate (Aldrich). Subsequently, photoinitiator of 2,2-dimethoxy-2-phenylacetophenone (Aldrich) was added to the monomer mixture at 4 wt %. Rad 2200N (TEGO Chemi Service) of 10 wt% was blended as a releasing agent with the prepared mixture. Although a residual layer remains between the glass substrate and the polymer pillar array after imprinting, it does not have to be removed because the refractive index (RI) of the polymer is 1.45, which is close to that of the glass. Deposition of a  $\text{SiN}_x$  layer on the polymer pillar array as the buffer layer completes the formation of photonic crystal structure on the glass substrates. The  $\text{SiN}_x$  layer is transparent and has high refractive index ( $\sim 2.02$ ). It was deposited to make the PhC surface planar and to give higher refractive index than that of polymer pillars. In order to achieve a flat surface,  $\text{SiN}_x$  is deposited on the PhC layer and two types of PhCs with different  $\text{SiN}_x$  layer thicknesses (500 nm and 800 nm) were used.

### **3.2.2. Polymer/ $\text{Si}_3\text{N}_4$ PhCs slab characterization**

The eight-inch silicon wafer was used as the stamp materials after patterned by the DUV lithography and RIE. The silicon stamp pattern has a hexagonal lattice

structure with repeated circular holes. The lattice constant of the holes is 530 nm and both the diameter and the height are 265 nm, which will produce the polymer pillar whose aspect ratio is 1:1. As for the PhC parameters, the photonic band structure of the hexagonal lattice was considered and the lattice constant was set to be close to the wavelength of light. All propagating visible-wavelength light is in the non-guided mode region at that lattice constant and above the band gap of photonic band structure. Hence, greater light intensity can be achieved at oblique viewing angles in the visible region<sup>12</sup>. **Figure 3.2 (b)** shows the scanning electron microscope (SEM) image of the fabricated PhC. SiN<sub>x</sub> completely fills the gap between the polymer pillars without voids and the surface becomes smoother by depositing the buffer layer (**Figure 3.2 (c)-(d)**).

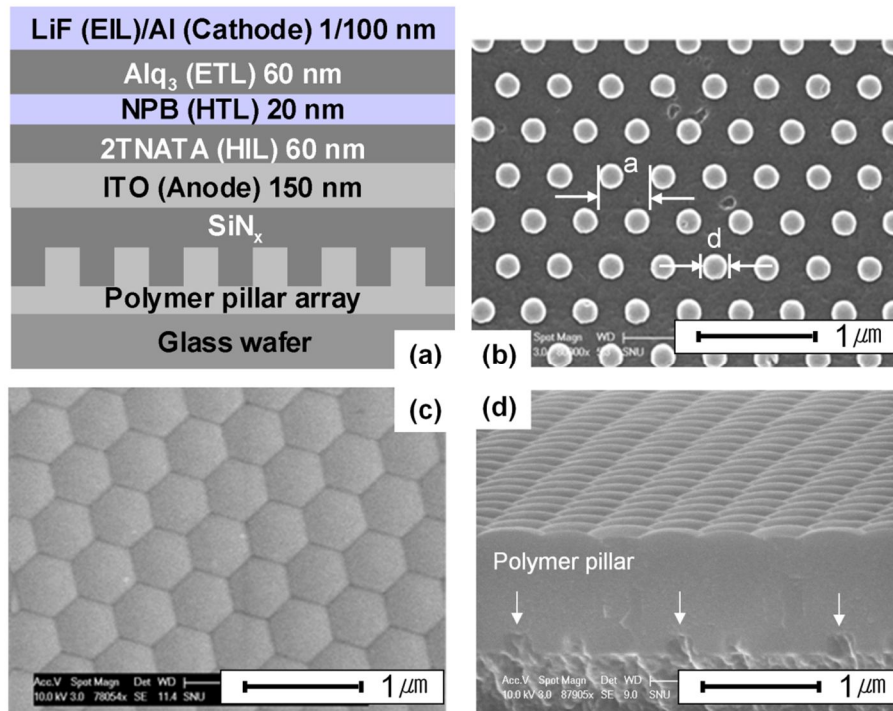


**Figure 3.2.** (a) Vertical structure and materials of OLED (b) SEM image of the imprinted polymer pillars. The pillar array is hexagonal lattice and its lattice constant and diameter are 530 nm and 265 nm, respectively (c) Top view of the PhC slab. The surface of PhC slab is honeycomb shape because buffer layer is deposited on a hexagonal lattice pillar. (d) Cross-sectional view of the PhC slab. The polymer pillars in the PhC slab can be observed.

### 3.3. Finite Difference Time Domain Simulation

In order to predict the performance of the proposed device, a 3D-FDTD (Finite Difference Time Domain) simulation was performed.<sup>18</sup> The simulation structure included air, a glass substrate, a polymer resin, SiN<sub>x</sub>, ITO, organic layers and cathode electrode layers. The polymeric PhC was modeled using a circular rod shape and the measured geometric parameters. The simulation domain size was  $3.13 \times 2.71 \times 6.19 \mu\text{m}^3$  and the time step was 0.0333 fs. The periodic boundary conditions were used on the four vertical sides of the simulation domain in order to reduce the simulation time, and the array size and the two upper and lower horizontal sides were set to have PML (Perfectly Matched Layer) boundary conditions. To model the cathode aluminum electrode, the Auxiliary Differential Equations method was employed where the single-pole Drude model was assumed.<sup>18</sup> Many Gaussian dipole sources were randomly distributed over the emission layer to consider actual light emission process in the organic layer, and the initial phase and the direction of dipole oscillation were randomly assigned at the beginning of the simulation. The center frequency of the each Gaussian dipole source was set to be the value corresponding to the OLED peak emission wavelength of 511nm and the time duration of the Gaussian pulse was determined on the order of fs for the source to have a broad emission wavelength band of about 50 nm. The simulation result is shown in Figure 3. The y axis is the time integration of the Poynting vector in the z-direction over the top surface in air. The integrated z-Poynting vector is a measure of the light emission out of the glass into the air. The extraction efficiency remained nearly constant for various glass thickness as shown in **Figure 3.3**. Therefore, the air layer can be included in calculation structure without excessive time consumption. The predicted light extraction efficiency of the polymer PhC was enhanced by nearly 70%.

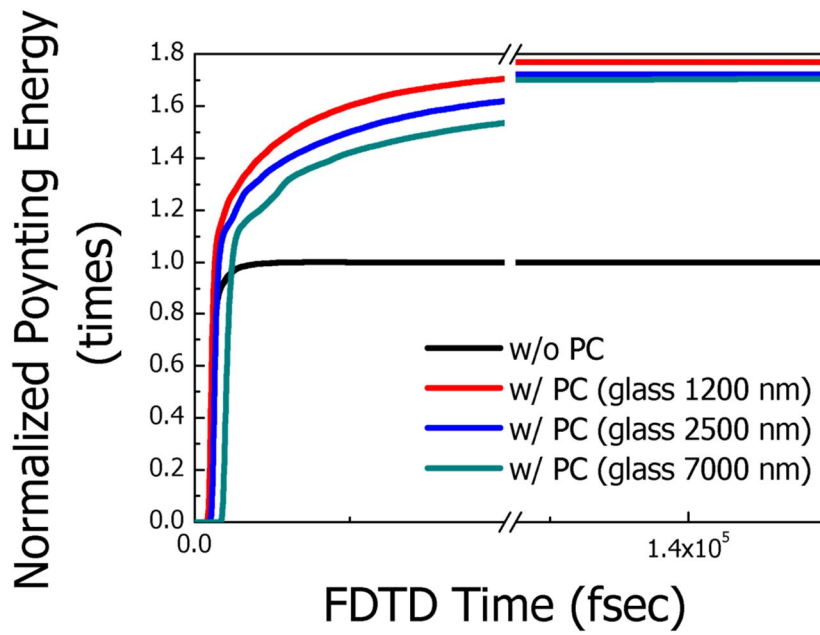


**Figure 3.3.** FDTD simulation results with variation in the glass thickness. The enhancement of the light extraction is nearly constant, with reasonable thickness variation. The simulation shows no thickness effect; therefore, adopting the glass thickness in the calculation is shown to be feasible. The enhancement is nearly 70% compared to a conventional OLED.

### 3.4. Electroluminescence Performance

Enhancement of the light extraction efficiency in the forward direction (glass side) and emission characteristics are also confirmed from the experiments. Relative integrated spectra of the light emitted from the device were measured using an integrating sphere (Labsphere Co., 6" dia) in order to detect all the light emitted in the forward direction. **Figure 3.4** shows the emission spectra of the device with relative EL intensities. The EL intensity of the photonic crystal device increases by more than 50% compared with the conventional device without a photonic crystal. Moreover, the enhancement of the light extraction from the PhC-OLEDs is represented by means of the integrated light-output power versus the current density as shown in **Figure 3.5**. The EL intensity was increased by 54% compared with the conventional device. Thinner SiN<sub>x</sub> buffer layer gives a little higher light extraction efficiency because the thick SiN<sub>x</sub> film causes additional light absorption.

As shown in the emission images in Figure 3.4, the conventional OLED emits light with a symmetric distribution in all in-plane directions, while the photonic crystal device produces a pattern with six-fold symmetry, reflecting the hexagonal structure of the PhC layer. Moreover, the profiles are represented in terms of the luminance efficiency in the inset of Figure 3.4. The maximum luminance efficiency of the photonic crystal device is 5.95 cd A<sup>-1</sup> at a tilted direction of 40 degrees, which is an improvement of nearly 30% of the maximum luminance of the reference. The profile of the reference device is very similar to the Lambertian profile, whereas the photonic crystal device produces a radiation shape that is similar to butterfly wings. The area of butterfly wings is about 1.5 times larger than the reference, and the result is consistent with the EL intensity measured by using an integrating sphere. The OLEDs integrated on PhC structures not only give high luminance efficiency but also exhibit interesting emission patterns depending on the symmetry and dimensions of the pillars such as lattice constant, diameter, height and arrangement.<sup>19-20</sup>

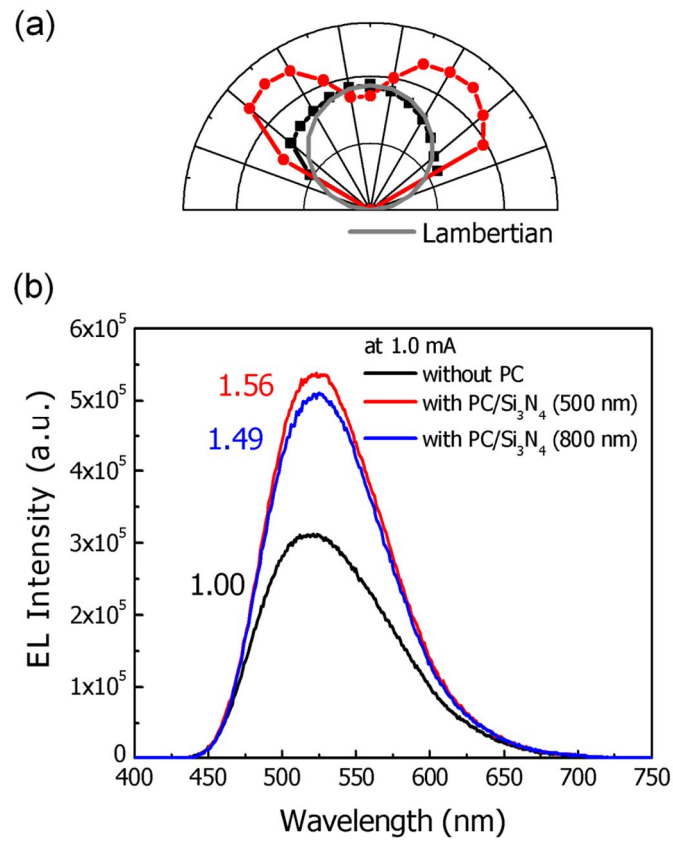


**Figure 3.4.** (a) Radiation profile represented in terms of luminance efficiency ( $\text{cd A}^{-1}$ ).  
 (b) EL intensity using integrating sphere measurement.

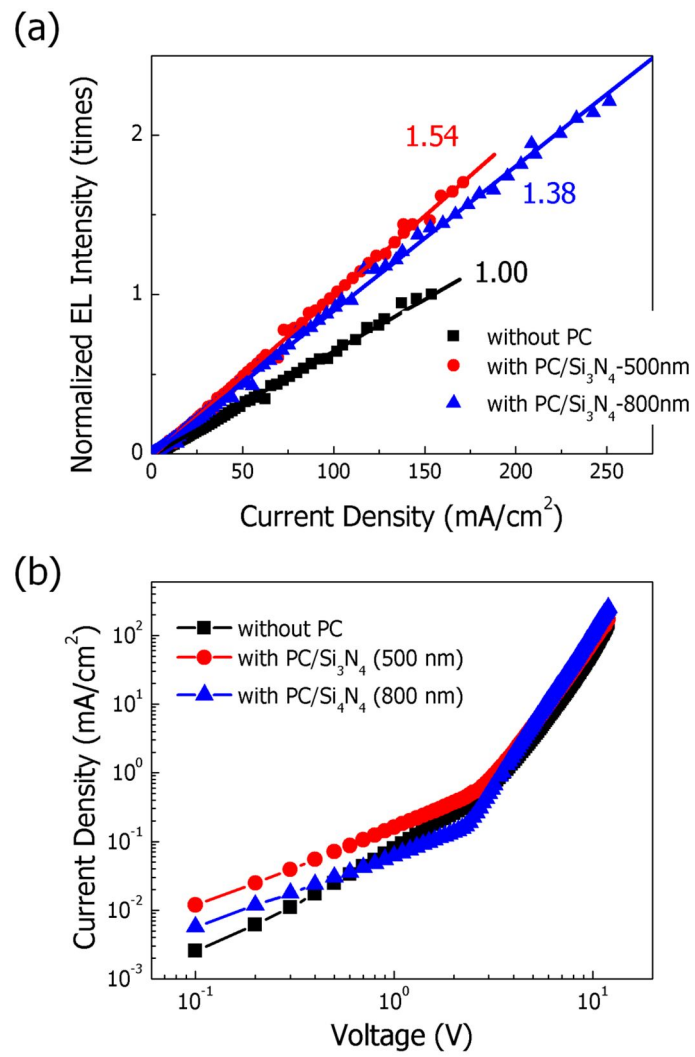


**Figure 3.5.** (a) The light-output power from the OLEDs with and without the PhC, (b)  $J$ - $V$  characteristics.

### 3.5. Conclusions

In conclusion, an etch-less UV-NIL process is developed to fabricate organic PhC structures as an OLED substrate. The developed process is simple and inexpensive because etching step is eliminated. Furthermore the process can be performed at room temperature without application of extra pressure. By applying the etch-less UV-NIL process, 50% enhancement of the device efficiency is achieved. The results demonstrate that the UV-NIL process of the polymer PhC structure is a promising method to enhance the light emission efficiency of OLEDs.

### 3.6 Bibliography

1. C. F. Madigan, M. -H. Lu, and J. C. Sturm, *Appl. Phys. Lett.* **76**, 1650 (2000).
2. N. C. Greenham, R.H. Friend, and D.D.C. Bradley, *Adv. Mater.* **6**, 491 (1994).
3. I. Schnitzer and E. Yablonovitch, *Appl. Phys. Lett.* **63**, 2174 (1993).
4. M. -H. Lu and J. C. Sturm, *Appl. Phys. Lett.* **78**, 1927 (2001).
5. S. Moller and S. R. Forrest, *J. Appl. Phys.* **91**, 3324 (2002).
6. T. Yamasaki, K. Sumioka, and T. Tsutsui, *Appl. Phys. Lett.* **76**, 1243 (2000).
7. T. Tsutsui, M. Yahiro, H. Yokogawa, K. Kawano and M. Yokoyama, *Adv. Mater.* **13**, 1149 (2001).
8. M. Agrawal, Y. Sun, S. R. Forrest and P. Peumans, *Appl. Phys. Lett.* **90**, 241112 (2007).
9. J. M. Ziebarth and M. D. McGehee, *J. of Appl. Phys.* **97**, 064502 (2005).
10. B. J. Matterson, J. M. Lupton, A. F. Safonov, M. G. Salt, W. L. Barnes and I. D. W. Samuel, *Adv. Mater. (Weinheim, Ger.)* **13**, 123 (2001).
11. H. J. Peng, Y. L. Ho, X. J. Yu, and H. S. Kwok, *J. of Appl. Phys.* **96**, 1649 (2004).

12. Shanhui Fan, Pierre R. Villeneuve, and J. D. Joannopoulos, and E. F. Schubert, *Phys. Rev. Lett.* **78**, 3294 (1997).
13. Y.-C. Kim, S.-H. Cho, Y. W. Song, Y.-J. Lee, Y.-H. Lee, and Y. R. Do, *Appl. Phys. Lett.* **89**, 173502 (2006).
14. Y.-J. Lee, S.-H. Kim, J. Huh, G. -H. Kim, Y.-H. Lee, S.-H. Cho, Y.-C. Kim, and Y. R. DO, *Appl. Phys. Lett.* **82**, 3779 (2003).
15. Y. R. Do, Y.-C. Kim, Y.-W. Song, C.-O. Cho, H. Jeon, Y.-J. Lee, S.-H. Kim, and Y. -H. Lee, *Adv. Mater.* **15**, 1214 (2003).
16. K. Ishihara, M. Fujita, I. Matsubara, T. Asano, S. Noda, H. Ohata, A. Hirasawa, H. Nakada and N. Shimoji, *Appl. Phys. Lett.* **90**, 111114 (2007).
17. Stephen Y. Chou, Peter R. Krauss, and Preston J. Renstrom, *J. Vac. Sci. Techno. B.* **14**(6), 4129 (1996). 18.
19. A. Taflove and S. C. Hagness, *Computational Electrodynamics: The Finite-Difference Time-Domain Method 2nd ed.*, Artech House, Norwood **2000**.
20. S. G. Johnson and J. D. Joannopoulos, *Photonic crystals*, Kluwer academic publishers, Boston **2002**.

# Chapter 4

## Vacuum Nano Hole Array Embedded OLED : Fluorescent Molecules as an Emitter

---

### 4.1. Introduction

Organic light emitting diodes (OLEDs) have been successfully applied to various mobile electronics because the display, which utilizes a spontaneous emission of light from organic molecules by nature, is a very energy efficient way to produce vibrant images. OLEDs intrinsically provide high energy efficiency compared with other light sources, but they still have more potential to enhance the efficiency for common uses such as general lighting. Only around 20-30% of the light generated by a typical bottom emission OLED is extracted into the air because the light intensity is decreased by a factor of  $1/2n^2$  as the light passes through each layer, where  $n$  is the refractive index (RI).<sup>1, 2</sup> The light extraction efficiency, which is one of the most important factors, can be enhanced by applying photonic implements to each layer. Various methods have been proposed to convert the waveguide and glass modes into the radiation mode, e.g., textured surfaces, microlens arrays, scattering medium, Bragg gratings and low-index grids, and thus the extraction efficiency has been improved continuously.<sup>3-10</sup>

The light wasted by the waveguide mode can be extracted into the air by inserting photonic layers to the inside of OLED devices. For example, nanoarrays are inserted between the anode and substrate as in the case of two dimensional

photonic crystal (2D-PhC) OLEDs<sup>11-16</sup> and corrugated OLEDs.<sup>15-19</sup> As for the case of corrugated structure, Koo et al. demonstrated high efficiency buckled OLEDs and Jeon et al. reported results on corrugated OLEDs. In these cases, OLEDs were directly fabricated on the nanostructure without additional planarization and the subsequent layers were deposited unevenly above the nanostructure. The uneven thickness variations changed the electronic properties of the anode and lead to undesirable electrical effect. The electric field concentrated on the thinner regions of the layers resulted in degradation of organic materials. Although the corrugated structure enhanced extraction of light, non-uniform distribution of the electric field had a negative influence on the device reliability.<sup>15, 17, 20</sup> Therefore, the planarization of the inserted nanostructure layer is a very important issue from an electrical point of view.

Electrical properties of the 2D PhC OLEDs are stable compared with those of corrugated OLEDs because the 2D PhC OLEDs are fabricated on a relatively smooth surface after nanoarrays have been covered by the successive planarization layer. Various methods were used in order to fabricate an even surface for the 2D PhC OLEDs, i.e., the plasma-enhanced chemical vapor deposition (PECVD),<sup>11, 13</sup> sol-gel spin-coating,<sup>12, 21</sup> and doctor blade process.<sup>14</sup> However, it was not possible to obtain a substrate whose surface was even enough to have sub-nano scale roughness comparable to the average surface roughness of the same level of polished Si wafers and for the OLED to operate normally under electric field over the entire active area.

In this chapter, low vacuum nano-hole arrays (NHA) were embedded to the sub-nano scale planarized substrate to maximize RI contrast for the given background material,  $\text{Si}_3\text{N}_4$  ( $n_{\text{high}}=2.02$ ). Low vacuum nano-holes ( $n_{\text{low}}=1$ ) were generated periodically over the  $xy$ -plane and 2D PhCs were inserted into OLEDs in order to extract the light trapped in the waveguide mode into the air without any change of electrical properties. In addition, it was demonstrated by the FDTD simulation and experiments that the inserted NHA was efficient for extraction of the propagating light generated from both the vertical (as expected) and horizontal

dipoles, which means that the NHA structure affects not only the waveguide mode but also the glass mode.

## 4.2. Experimental

### 4.2.1. NHA Substrate Fabrication

The light extraction efficiency can be improved significantly by means of PhC diffraction and its diffraction strength, i.e., the more the RI difference increases, the higher the extraction efficiency becomes. Since vacuum (or air) has the lowest refractive index, a vacuum hole array in the PhC leads to maximum PhC diffraction strength for any given high index material. However, it is difficult to confine an ordered vacuum hole array in the PhC by using the bottom-up process. In this study, the NHA substrate was fabricated using a novel nanostructuring approach called robust reverse-transfer ( $R^2T$ ). The  $R^2T$  process is developed in order to generate the vacuum state hole inside of the  $Si_3N_4$  slab and it has important implications for the future of photonic optoelectronics engineering.

**Figure 4.1a** shows a schematic diagram for fabrication of a 2D nano-hole array in  $Si_3N_4$  which is the high refractive index material by using the novel process called  $R^2T$ . First, an 800nm thick  $Si_3N_4$  film was deposited on the silicon substrate by means of plasma-enhanced chemical vapor deposition and then a hexagonal hole array was introduced on the silicon nitride film by using a conventional photolithography, the dry etch process. The nano-hole embedded  $Si_3N_4$  on the silicon substrate and the glass wafer were bonded using the anodic bonding procedure. Covalent bonds are formed at the interface between glass and  $Si_3N_4$  substrates by means of the anodic bonding<sup>22</sup> that was generated by drifting of sodium and oxygen ions of  $NaO_2$  molecules present in the glass substrate. Under strong electrostatic field and high temperature (over the glass transition

temperature), positive and negative ions moved to the cathode and the anode, respectively. The  $O^{2-}$  ions moved to the interface and formed covalent bonds with the silicon atoms in the  $Si_3N_4$  film. This is the reason why  $Si_3N_4$  was selected as the background material. The silicon compound was used since  $Si_3N_4$  has good optical properties such as high refractive index and transmittance at the same time. Irreversible bonds are created in addition to acting as an adhesive and thus the subsequent wet etch process does not damage the bond.

The bonded wafers were dipped in a KOH solution to remove the silicon substrate. Consequently, a nanostructure was obtained as the OLED substrate that has vacuum (as low index material, actually the lowest index material) holes and  $Si_3N_4$  (as high index material) matrix alternately. The etch selectivity to a KOH solution for Si is 100 times greater than  $Si_3N_4$  and thereby the top of the  $Si_3N_4$  is not damaged by the etcher, resulting in extremely even surface that actually has a roughness comparable to the  $R_a$  roughness of the silicon wafer, 3-4Å. The low level of surface roughness is a very important aspect for the electrical performance of the OLED devices that will be dealt with in detail later.

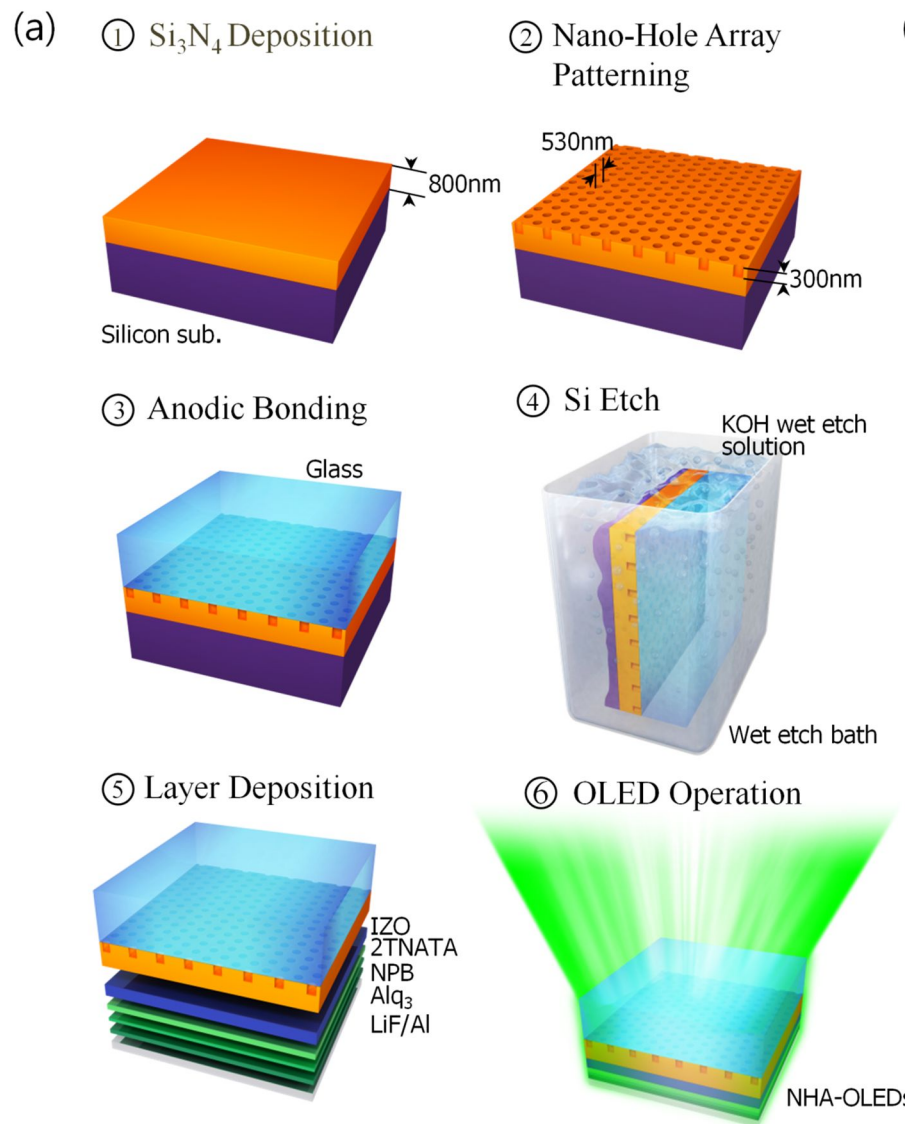


**Figure 4.1.** (a) Schematic diagram for fabrication of the 2D nano-hole array with  $\text{Si}_3\text{N}_4$  as the high-index material and the novel process used in this fabrication is called  $\text{R}^2\text{T}$ .

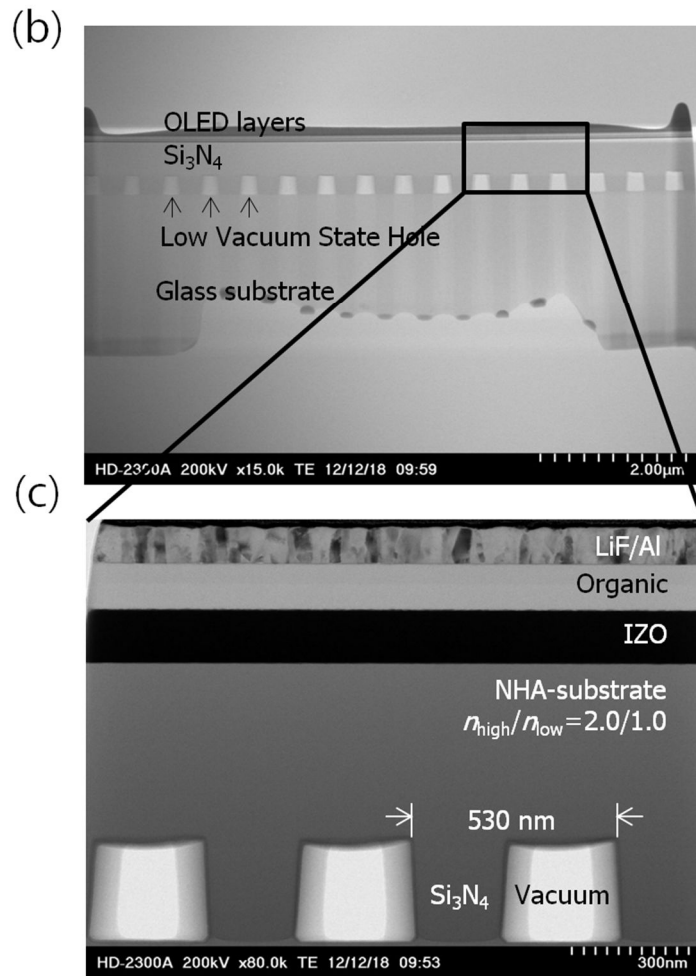


**Figure 4.1.** (b) scanning transmission electron microscopy (STEM) image of the NHA substrate fabricated by R<sup>2</sup>T process, and (c) vertical structure of the NHA-OLED.

## 4.2.2. NHA OLEDs Characterization

The R<sup>2</sup>T process (the bonding process between nano-holes and glass wafer) was carried out in a vacuum chamber, and then the following layers, consisting of inorganic (Si<sub>3</sub>N<sub>4</sub>(500 nm)/IZO(150 nm)), organic (2TNATA/NPB/Alq<sub>3</sub>(60/20/60 nm)) and metal (LiF/Al(1/100 nm)) materials, were deposited under high vacuum whose pressure was around 10<sup>-7</sup> Torr. In general, inorganic materials have low gas permeability, thus it is expected that the nano-holes were at vacuum state, although it is not possible to measure the pressure directly in the nano holes. Furthermore, the RI (i.e. speed of light in the medium) is not changed whether the nano holes are at vacuum state or filled with some gases. Subsequently, the extraction properties are not changed as well. The R<sup>2</sup>T method was based on the 8-inch wafer process, and then OLEDs devices were fabricated on diced substrate into 25×25 mm<sup>2</sup>. The R<sup>2</sup>T bonding is almost a defect-free process over the entire region of an 8-inch wafer (See **Figure A.2** in supplementary information).

**Figure 4.1b** shows scanning transmission electron microscopy (STEM) images of the NHA substrate fabricated by R<sup>2</sup>T process and **Figure 4.1c** shows the vertical structure of the NHA-OLED. Photoluminescence (PL) and electroluminescence (EL) experiments were analyzed by the three dimensional finite difference time domain (FDTD) simulation based on a small molecule bottom emitting OLED using the emitter, tris-(8-hydroxyquinoline) aluminum (Alq<sub>3</sub>) which has a random orientation of dipoles.

## 4.3. FDTD Analysis

### 4.3.1. The effect of the refractive index contrast

FDTD simulation was carried out to evaluate the effect of the RI contrast on the

extraction efficiency of the PhC embedded OLEDs. The simulation is performed for the same structure, consisting of an Al cathode, organic material, anode, glass, and the inserted PhC slab. The emission energy is calculated by varying the RI difference between  $n_{\text{low}}$  and  $n_{\text{high}}$  of the PhC slab. Different PhC substrates were evaluated with respect to orientation angle of the oscillating electric dipole source, e.g., the RI values of the  $n_{\text{low}}/n_{\text{high}}$  were 1.75/2.02, 1.5/2.02, 1.25/2.02, and 1.0/2.02. The lattice constant ( $\Lambda$ ) was set to be 530 nm, the same as the emission peak wavelength of Alq<sub>3</sub> photoluminescence (PL), because the extraction efficiency becomes largest when the lattice constant is similar to the vacuum wavelength.<sup>11,20</sup> A diameter of  $0.5\Lambda$  and height of 300 nm were chosen because the light extraction varied as a function of hole depth and was saturated when the hole depth reached the value of the height. The lattice constant is one of the most important factors of the PhC but the diffraction strength has a profound influence on the extraction efficiency in this study. In other words, the RI difference between  $n_{\text{low}}$  and  $n_{\text{high}}$  is more crucial than the lattice constant of PhCs (studies on the lattice parameters of PhCs are discussed in detail at the supplementary information. See **Figure B.2**). **Figure 4.4a** shows results of the FDTD analysis. Each point represents the enhancement factor of the time integration values of the Poynting energy in the z direction ( $P_z$ ) obtained by dividing the spectrum of the NHA-OLED by that of the reference (on bare glass) OLED. The Poynting energy is integrated over the  $xy$ -surface in glass by using the following equation.

$$P_z = \int_t \int_A \int_\omega \mathbf{P} \cdot \mathbf{n}_z \, d\omega \, dA \, dt \quad (1)$$

where the  $t$ ,  $A$  and  $\omega$  are time, integrated area and frequency, respectively.

### 4.3.2. The emission energy for the three primary colors

It should be noted that the glass substrate was not included in the FDTD simulation because the glass substrate has the thickness about three orders of magnitude larger than that of the other layers in the OLED device. As shown in Figure 2a, the observed Poynting energy increases for all dipole angles as the RI difference of the slab becomes larger. Especially, the energy induced from the vertical dipoles is most improved and the enhancement decreases toward the horizontal dipole. The contours shown in **Figure 4.4c** allow us to intuitively visualize the impact of the RI contrast on the energy extraction. Those are  $P_z$  maps of the  $xy$ -planes inside of the glass that was induced from the horizontal ( $d_x$ ,  $d_y$ ) and the vertical dipoles ( $d_z$ ) on the bare (control), 1.5/2.02 PhC array, and 1.0/2.02 PhC array substrate devices. Particularly, in the case of the vertical dipoles ( $d_z$ ), almost no Poynting energy is observed on the bare glass which has no diffraction media. However, the 1.0/2.02 nano-hole array substrate improved extraction efficiency due to the interaction between the emitted rays and the scattering medium that has the maximum RI contrast of the embedded nanostructure. This means that the light emission from the vertical dipoles is lost by the waveguide mode during propagation and enhanced significantly due to insertion of the PhCs between the anode and the glass. Since the period is also the same as the median of the visible wavelength range, entire range of the visible light can be enhanced using the NHA structure. The emission energy is calculated with respect to the dipole source which emits different wavelength to estimate the extraction property. Enhancement of the emission energy for the three primary colours, which have wavelength of 460, 530, and 620 nm, are plotted in **Figure 4.4b** with or without the NHA structure. As the result, the NHA structure used in this study can be a proper candidate to enhance the extraction of the white OLED for general lighting.

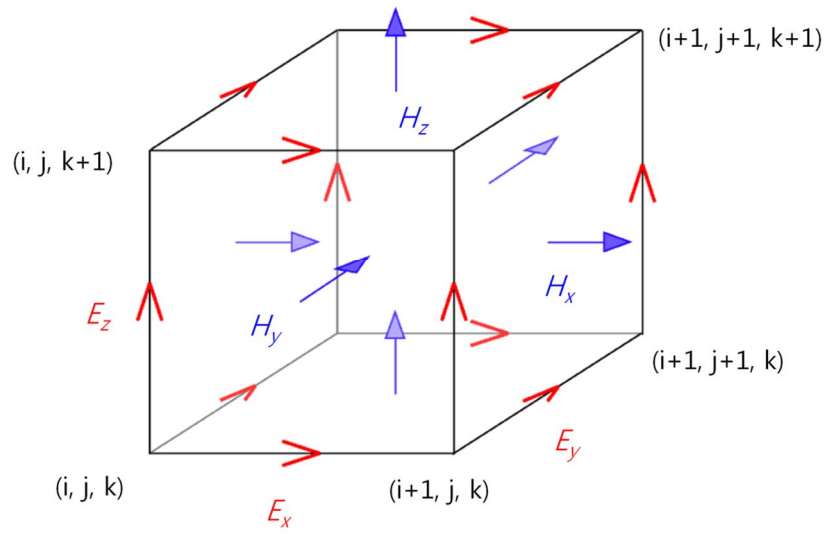


**Figure 4.2.** Illustration of a standard Cartesian Yee Cell used for FDTD, about which electric and magnetic field vector components are distributed.<sup>23</sup>

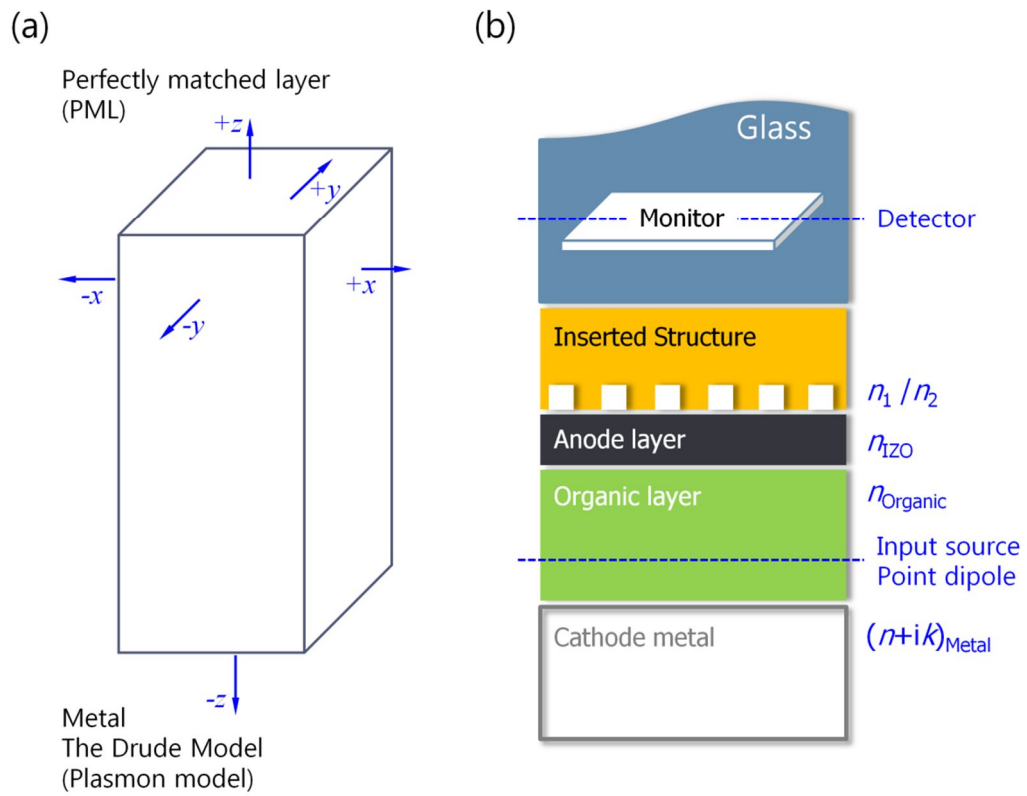


**Figure 4.3.** (a) Boundary conditions. (b) FDTD structure used for optical simulations

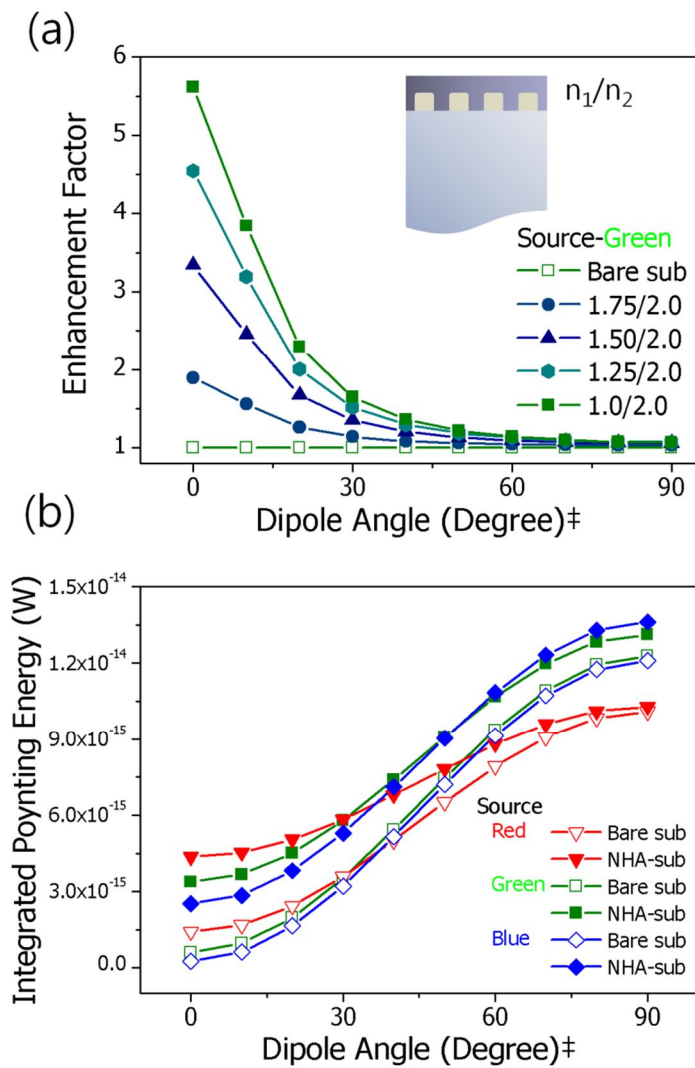


**Figure 4.4.** FDTD analysis results: (a) Different PhC substrates were modeled by varying the RI contrast ( $n_1/n_2$ ) for a given background material ( $\text{Si}_3\text{N}_4$ ,  $n_2=2.02$ ). (b) Enhancement of the emission energy was estimated for three different wavelengths of the primary colors when the NHA structure was inserted.

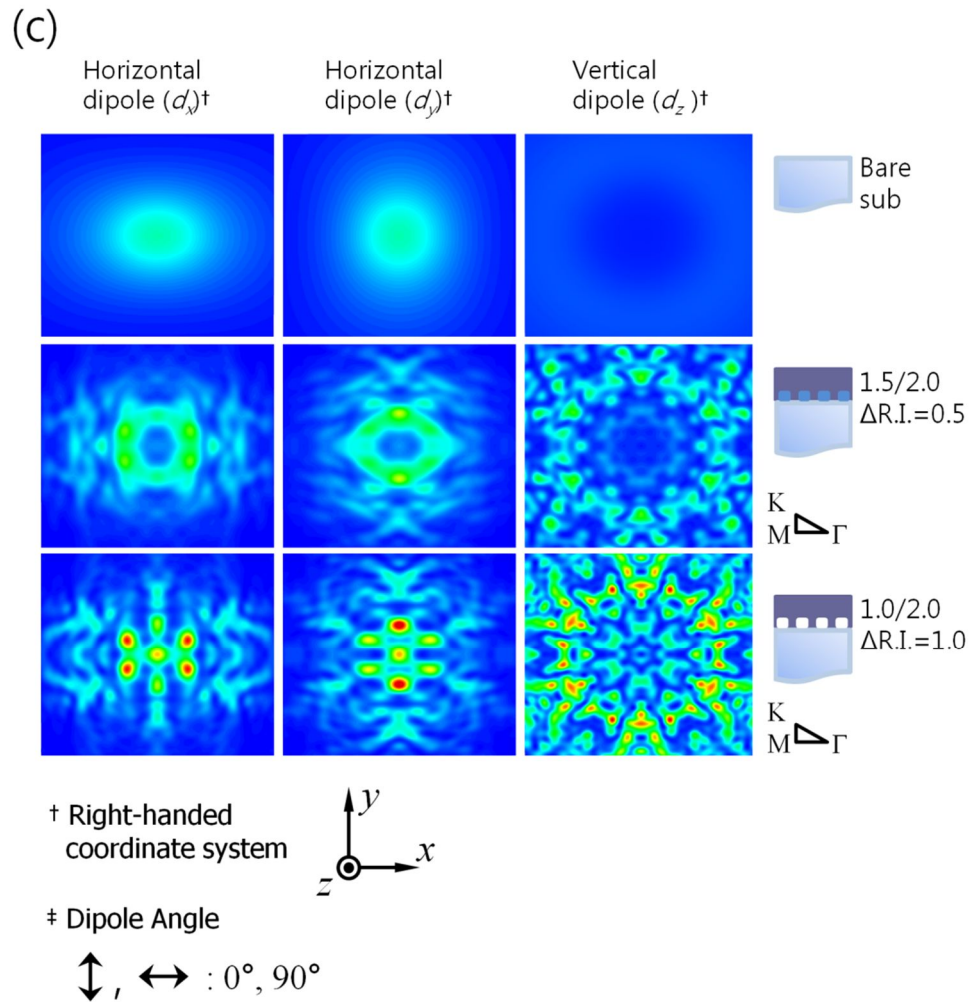


**Figure 4.4.** (c) Contours of Poynting energy emitted from  $d_x$ ,  $d_y$ , and  $d_z$  dipoles on the bare (control), 1.5/2.02 PhC array, and 1.0/2.02 PhC array substrate devices.

#### 4.4. Angular Dependence of Photoluminescence

Prior to fabricating the OLEDs, the angular dependence of the photoluminescence (PL) is measured and compared with the numerical simulation. The schematic diagram of PL intensity measurement is illustrated in the supplementary information.<sup>24</sup> **Figure 4.5a** and **4.5b** show the s- and p-polarized light emission from the waveguide mode for the wavelength of 520 nm, corresponding to the PL peak wavelength of the organic molecules. It is meaningful that the measured PL intensity is compared with that of the FDTD simulation because both results showed improvement from the waveguide mode, not from the glass mode, and the results are consistent with each other. In the case of the p-polarized light induced from the  $d_x$  and  $d_z$  dipoles, the PL intensity is improved by more than two times for all viewing angles (five times at most for certain angles), whereas it shows little improvement for the s-polarized light induced from the  $d_y$  dipole as shown in Figure 3a and 3b. These experimental results are the same as expected by the FDTD analysis. However, the s-polarized light is also improved by the NHA structure over the range of  $\pm 45^\circ$ . The insertion of NHA also leads to improvement of the s-polarized light by changing the intensity distribution and focusing the light on the center area. As the result, the extraction is enhanced when the intensity is measured in the air because the critical angle at the glass ( $n=1.47$ )/air ( $n=1.0$ ) is  $41.8^\circ$ . Therefore, the proposed NHA structure is adequate for extraction of the emission induced from both vertical and horizontal dipoles.

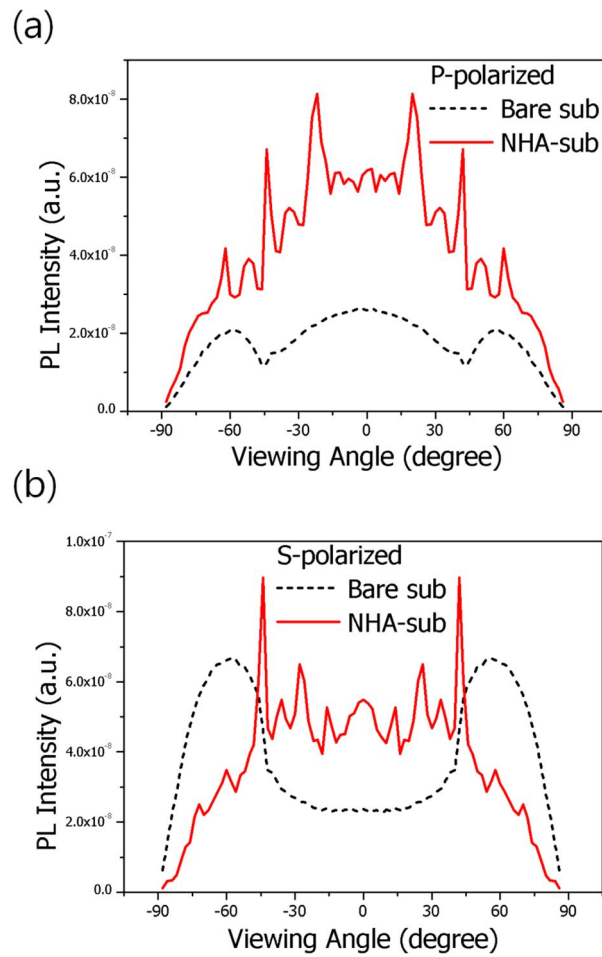


**Figure 4.5.** PL intensity measured as a function of the viewing angle for (a) the p-polarized and (b) the s-polarized light emission with the wavelength of 520 nm.

## 4.5. Electroluminescence of NHA-OLEDs

### 4.5.1. Intensified CCD measurement

**Figure 4.6a** shows the device performance of the NHA inserted and reference OLEDs. Each layer thickness of the OLED device is determined by optimizing the control device (OLEDs integrated on the bare glass), and the extraction structure is examined from the optimized control device which has high efficiency of 5.04 cd/A. The EL intensity of each device was measured using an integrating sphere to detect the light emitted into the air in all directions. The experimental data were obtained from the representative device selected among more than a dozen cells. The EL intensity is the spectra accumulated 100 times by controlling the recording system of the measurement. It was found by integrating over the FWHM wavelength range of 488 to 574 nm that the relative spectrum was improved by 1.89 times when the NHA implemented device was compared with the reference one. The enhancement factor was obtained by dividing the spectrum of the NHA-OLED by that of the reference at each wavelength. The maximum value of the enhancement factor is 2.01 and the maximum enhancement was obtained at the maximum peak of the spectrum, which means that the inserted nanostructure did not cause a spectrum shift or a change of colour coordinates. The results are summarized in **Table 4.1**.

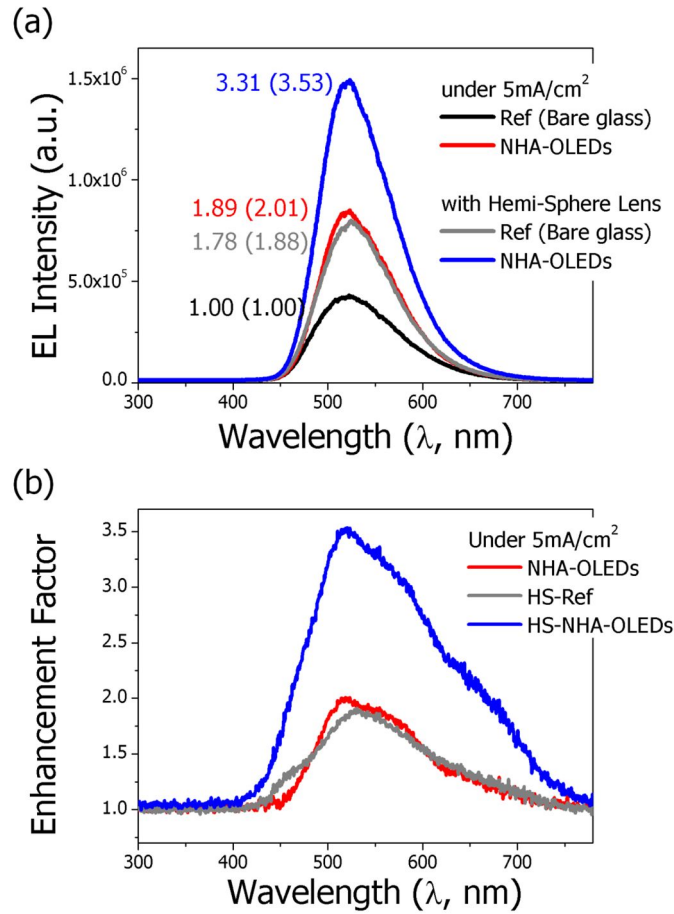


**Figure 4.6.** (a) EL intensity measured for each device as a function of wavelength: (a) the EL intensity of the NHA-OLED (red solid line) and the control (black dashed line) device measured using an integrating sphere. The EL intensity was also measured for each device by attaching a 10 mm hemisphere lens to the NHA-OLED (blue solid line) and the control device (gray dashed line). The inset value represents enhancement ratio which is obtained by dividing the integrated area of each spectrum by that of the control spectrum. Ratio of the EL intensity of each spectrum to that of the control spectrum at the peak wavelength ( $\lambda = 523$  nm) is given in the parenthesis. (b) The enhancement factor is obtained by dividing the spectrum of the NHA-OLED by that of the reference at each wavelength.

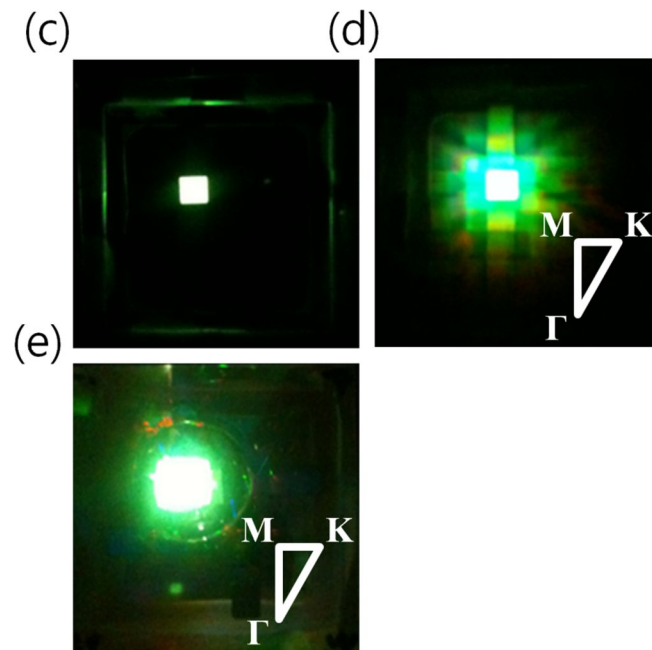


**Figure 4.6.** Snapshot of the emission from (c) the control OLED (bare glass) is shown and that from (d) the NHA-OLED is provided. Snapshot of the emission from the NHA-OLED with the hemisphere lens attached is shown in (e). All the photographs were taken at the same scale.

**Table 4.1.** EL enhancement values for different wavelength ranges. The EL enhancement is coupled with the radiation modes converting from both the waveguide loss and the glass loss modes.

Device	At 523 nm		488-574 nm		450-650 nm		Efficiency (cd A <sup>-1</sup> )
	Max. peak		FWHM		Whole range		
Reference (Bare)	1.0	-	1.0	-	1.0	-	5.04
NHA-OLEDs	2.01	-	1.89	-	1.76	-	8.87 <sup>b)</sup>
HS-Reference (Bare)	1.88	(1.00) <sup>a)</sup>	1.78	(1.00)	1.69	(1.00)	8.52
HS-NHA-OLEDs	3.53	(1.87)	3.31	(1.86)	3.09	(1.83)	15.57

<sup>a)</sup>The relative enhancement was obtained by dividing the EL intensity of the NHA device with the hemisphere (HS) lens attached by that of the reference HS-OLED and given in the parenthesis. It means enhancement of the light extraction from only the waveguide mode influence by the NHA structure; <sup>b)</sup>The efficiency is calibrated with the measured efficiency of the control device by using spectrum of figure 4(a).

### 4.5.2. EL-intensity of half-sphere lens attaching OLEDs

The EL intensity was also measured for each device by attaching a 10 mm diameter hemisphere lens to the device. Insertion of a nanostructure between an anode and the glass substrate affects not only the emitted light from the organic layer but also the re-entering light due to total internal reflection (TIR) at the glass-air interface. The observed light in the air is the combination of the light extracted from the waveguide and glass modes into the air mode. Therefore, we can exclude TIR by attaching a hemisphere lens at the glass-air interface and making a spherical surface such that the light which reaches the glass directly should escape from the device. Magnitude of the waveguide loss, which is converted into light by modifying the interface between the organic anode and the glass, can be determined quantitatively by comparing the two devices with hemisphere lenses attached. The relative values are represented in parentheses in Table 1 and the values in the parentheses mean that the extracted energy is increased by about 80% from the waveguide mode due to the nanostructure. When the wavelength gets closer to the maximum peak, both loss modes are converted into the radiation mode and thus the extraction enhancement is maximized at the peak wavelength.

### 4.5.3. Diffraction pattern induced from substrate modes

The enhancement factor was calculated as a function of the wavelength by dividing the emission spectra of the NHA-OLED by that of the OLED without the nanostructure in order to evaluate the wavelength dependence of the emission. As shown in **Figure 4.6b**, the enhancement factor has a maximum value at the same wavelength as the peak of the emission spectra and shape of the enhancement factor curve is similar to that of the emission spectra. **Figure 4.6c** and **4.6d** provide snapshots of the OLED devices fabricated on the bare glass and on the NHA embedded substrate without the hemisphere lens. **Figure 4.6e** provides an image of

the NHA-OLED with the hemisphere lens attached. The NHA-OLED yields the light with 6-fold diffraction pattern induced from the nanostructure symmetry whereas the 6-fold symmetry disappears when the hemisphere lens is attached to the NHA-OLED although there is a triangular structure below the surface as well. It is found that the diffraction pattern results from diffraction of the glass mode. The diffraction occurs at both the waveguide and glass modes during extraction into the radiation mode. However, in the case of diffraction of the waveguide mode, the induced pattern is indistinguishable to the naked eye because the distance between the emitted rays and the diffraction media is very short, i.e., hundreds of nanometers. On the other hand, diffraction of the glass mode travels a very long path of  $d$  between the nano-hole and the glass-air interface (the glass thickness in this case) which is about a few millimeters. The  $n^{\text{th}}$  order diffraction squares are  $2dntan\theta$  away from the active square according to the Bragg's law where  $\theta$  is the diffraction angle. Since  $2dntan\theta$  is large enough to be recognizable to the naked eye, it was possible to observe the diffraction pattern and the dispersing squares around the active area. The 6-fold symmetry pattern shown in Figure 4d is induced from the reflected rays at the glass-air interface, remote from the diffraction media. The hemisphere lens attached NHA-OLED did not show diffraction patterns because the light is extracted directly through the air by excluding the TIR at the glass-air surface.

#### 4.5.4. J-V-L characteristics of VNHA OLEDs

**Figure 4.7a** shows the luminance (L) with respect to the current density (J). Light power of NHA-OLEDs improved by a factor of 2.16. The profiles with or without NHA structure are represented in the inset of figure 5(a). **Figure 4.7b** shows the EL intensity depending on the viewing angle under the identical current injection. As expected, the EL intensity of the OLED on the bare glass is decreased as the viewing angle ( $\varphi$ ) is increased by factor of  $\cos \varphi$ , while the nano-hole array affects

the spectra of the NHA-OLEDs to change irregularly. All the spectra of the NHA-OLED over 50° viewing angle are larger than the maximum spectrum of the control device measured in the normal direction.

The radiation profiles for all the samples are shown in inset of figure 5a as well. On the other hand, one of the most important characteristics of electronics is electrical performance. The NHA embedded substrate used in this study is obtained by transferring the holes in  $\text{Si}_3\text{N}_4$  to the glass substrate and thereby bringing the roughness of the final substrate to the same level as that of the initial substrate. Silicon is used as a sacrificial layer in this study so that a substrate of angstrom roughness can be obtained. The J-V curves of the two devices with or without the nanostructure are exactly the same on the linear scale as shown in **Figure 4.7c**. J-V curve of the OLED on polymer nanostructure (PNA)/ $\text{Si}_3\text{N}_4$  system was plotted in **Figure 4.7d**. In our previous study, <sup>13</sup>  $\text{Si}_3\text{N}_4$  was deposited using PECVD in order to make a smooth surface. Although the obtained surfaces were very smooth with average roughness of a few nanometers, this level of roughness was still not sufficient for stable operation of OLEDs. Various electrical losses occurred due to the wavy and peaky surface of the anode, i.e., electrical leakages, non-uniform distribution of electric field, and concentration of electric fields led to organic damage.<sup>15, 17</sup>

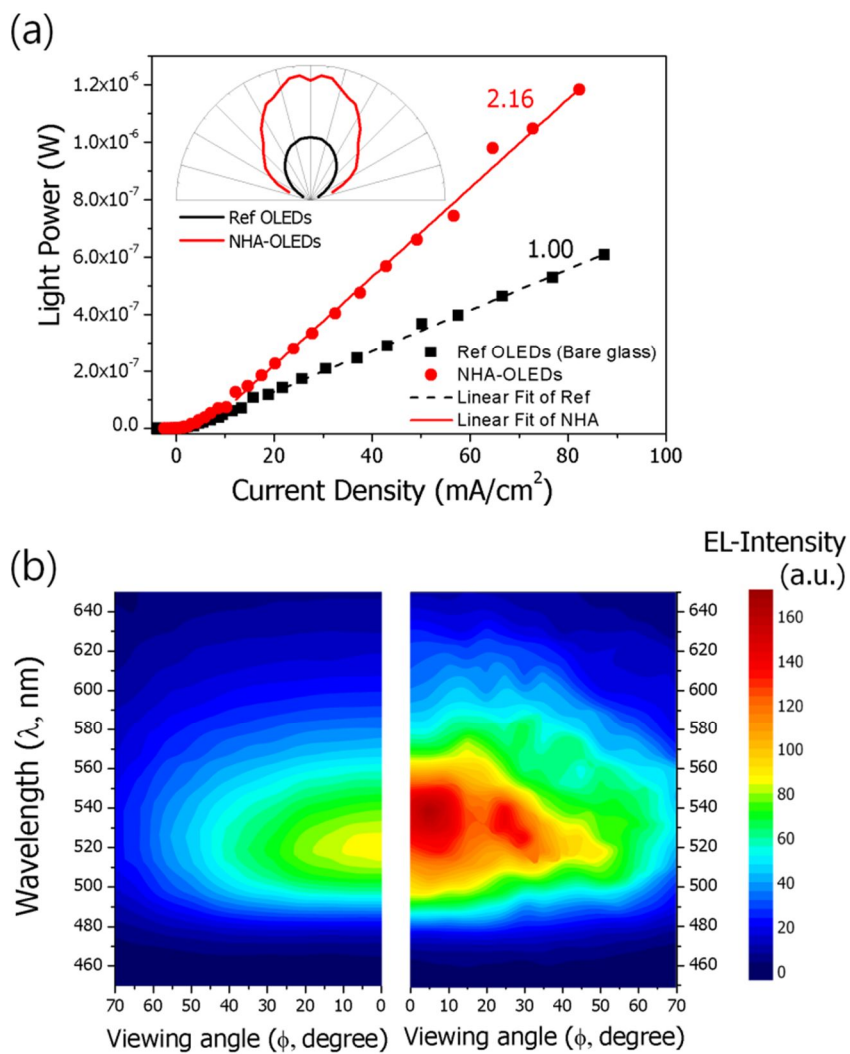


**Figure 4.7.** (a) J-L curves of the OLEDs on the bare glass and on the NHA substrate. Inset: Far field radiation profiles of the reference and the NHA-OLEDs. (b) EL intensity contours of the reference and NHA-OLEDs depending upon the wavelength and the viewing angle.

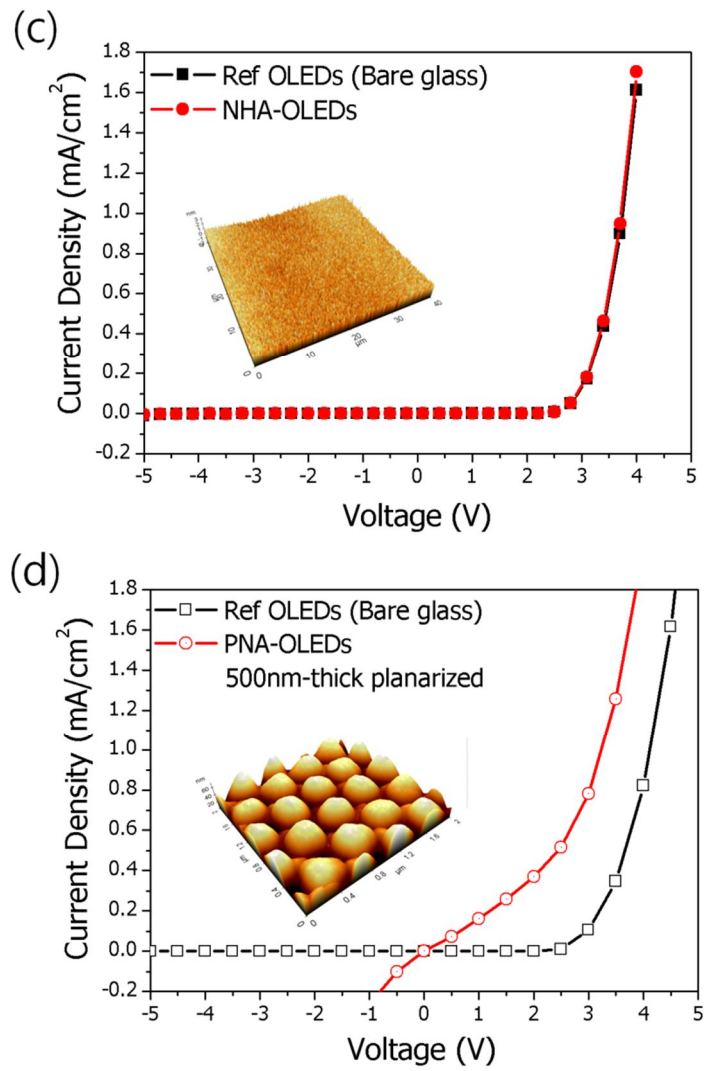


**Figure 4.7.** (c) J-V curves of the OLEDs on the bare glass and on the NHA substrate with angstrom level roughness. (d) J-V curve of the OLED fabricated on the polymer nanoarray (PNA)/Si<sub>3</sub>N<sub>4</sub> substrate that was covered by the successive planarization layer using PECVD.

## **4.6. Conclusions**

In conclusion, the NHA structure fabricated by R<sup>2</sup>T process is effective in extracting light into the air from the waveguide and glass loss modes. Light power of the NHA embedded OLEDs is improved by a factor of 2.16. Experimental results of the NHA-OLEDs were consistent with the FDTD simulation results such that the light emitted from both the vertical and horizontal dipoles is considerably improved. In addition to the optical advantages, the obtained surface has the roughness comparable to that of the Si wafer due to the transfer process, which leads to almost perfect electrical characteristics.

## 4.7. Bibliography

1. N. C. Greenham, R. H. Friend and D. D. C. Bradley, *Adv. Mater.*, 1994, **6**, 491-494.
2. S. Nowy, B. C. Krummacher, J. Frischeisen, N. A. Reinke and W. Brutting, *J. Appl. Phys.*, 2008, **104**, 123109.
3. T. Yamasaki, K. Sumioka and T. Tsutsui, *Appl. Phys. Lett.*, 2000, **76**, 1243-1245.
4. T. Tsutsui, M. Yahiro, H. Yokogawa and K. Kawano, *Adv. Mater.*, 2001, **13**, 1149-1152.
5. S. Moller and S. R. Forrest, *J. Appl. Phys.*, 2002, **91**, 3324-3327.
6. T. Nakamura, H. Fujii, N. Juni and N. Tsutsumi, *Optical Review*, 2006, **13**, 104-110.
7. Y. Sun and S. R. Forrest, *J. Appl. Phys.*, 2006, **100**, 073106.
8. S. Y. Hsu, M. C. Lee, K. L. Lee and P. K. Wei, *Appl. Phys. Lett.*, 2008, **92**, 013303.
9. Y. Sun and S. R. Forrest, *Nature Photonics*, 2008, **2**, 483-487.
10. S. M. Chen and H. S. Kwok, *Opt. Exp.*, 2010, **18**, 37-42.
11. Y. J. Lee, S. H. Kim, J. Huh, G. H. Kim, Y. H. Lee, S. H. Cho, Y. C. Kim and Y. R. Do, *Appl. Phys. Lett.*, 2003, **82**, 3779-3781.
12. Y. C. Kim, S. H. Cho, Y. W. Song, Y. J. Lee, Y. H. Lee and Y. R. Do, *Appl. Phys. Lett.*, 2006, **89**, 3779-3781.
13. S. Jeon, J. W. Kang, H. D. Park, J. J. Kim, J. R. Youn, J. Shim, J. H. Jeong, D. G. Choi, K. D. Kim, A. O. Altun, S. H. Kim and Y. H. Lee, *Appl. Phys. Lett.*, 2008, **92**, 223307.
14. W. J. Hyun, H. K. Lee, S. S. Oh, O. Hess, C. G. Choi, S. H. Im and O. O. Park, *Advanced Materials*, 2011, **23**, 1846-1850.
15. M. Fujita, T. Ueno, K. Ishihara, T. Asano, S. Noda, H. Ohata, T. Tsuji, H. Nakada and N. Shimoji, *Appl. Phys. Lett.*, 2004, **85**, 5769-5771.

16. K. Ishihara, M. Fujita, I. Matsubara, T. Asano, S. Noda, H. Ohata, A. Hirasawa, H. Nakada and N. Shimoji, *Appl. Phys. Lett.*, 2007, **90**, 111114.
17. A. O. Altun, S. Jeon, J. Shim, J. H. Jeong, D. G. Choi, K. D. Kim, J. H. Choi, S. W. Lee, E. S. Lee, H. D. Park, J. R. Youn, J.J. Kim, Y. H. Lee and J. W. Kang, *Org. Electron.*, 2010, **11**, 711-716.
18. W. H. Koo, S. M. Jeong, F. Araoka, K. Ishikawa, S. Nishimura, T. Toyooka and H. Takezoe, *Nature Photonics*, 2010, **4**, 222-226.
19. W. H. Koo, W. Youn, P. F. Zhu, X. H. Li, N. Tansu and F. So, *Adv. Func. Mater.*, 2012, **22**, 3454-3459.
20. J. M. Ziebarth and M. D. McGehee, *J. Appl. Phys.*, 2005, **97**, 064502.
21. H. H. Cho, B. Park, H. J. Kim, J. Shim, S. Jeon, J. H. Jeong and J. J. Kim, *Current Applied Physics*, 2010, **10**, E139-E142.
22. A. Berthold, L. Nicola, P. M. Sarro and M. J. Vellekoop, *Sensor Actuat. a-Phys*, 2000, **82**, 224-228.
23. K. Yee, *IEEE Transactions on Antennas and Propagation*, 1966, **14**, 302-307.
24. J. Frischeisen, D. Yokoyama, C. Adachi and W. Brutting, *Appl. Phys. Lett.*, 2010, **96**, 073302.

# **Part II**

## **Corrugated Organic Light Emitting Diodes**

# Chapter 5

## Corrugated Organic Light Emitting Diodes

---

### 5.1. Introduction

The power efficiency of organic light emitting diodes (OLEDs) is a critical issue in various practical applications. It is related to the light extraction efficiency and the operating voltage of the device. In a typical OLED, the light extraction efficiency is only about 20-30%.<sup>1-4</sup> Most of the light is lost in the waveguide modes. The light extraction efficiency can be improved using various methods such as random microstructures,<sup>5,6</sup> refractive index control,<sup>7</sup> micro-cavities<sup>8</sup> or two-dimensional (2D) photonic crystal (PhC) structures.<sup>9-19</sup>

Thus far, several studies have been done on single-layer PhC structured OLEDs (SPhC-OLEDs) that have a planarization layer coated onto the PhC structure before the deposition of an anode and organic layers. Coating a planarization layer is required to reduce the roughness of the anode, which is a major cause of electrical leakage. In SPhC-OLEDs, improvement of the light extraction characteristics occurs solely as a result of reducing the light losses in the substrate waveguide mode (Bragg diffraction).

When there is no planarization layer coated onto the PhC structure, the OLED layers are deposited in such a manner that each layer follows the patterned surface of the previously deposited layer. This accounts for the formation of a multi-layer PhC-structured corrugated OLED (simply corrugated OLED). This corrugated OLED results in a periodically corrugated metal cathode by which

important amount of surface plasmon mode associated with organic/metal interface can be Bragg reflected <sup>21, 22</sup> in addition to the Bragg diffraction coming from the periodic structure.

Recently, a 2D periodic corrugation is formed on the glass by direct thermal nanoimprint lithography (NIL) for OLED substrate and proved to be able to enhance light extraction and reduce the operating voltage <sup>13, 14</sup>. Laser interference lithography followed by physical plasma etching was also used to texture the anode and fabricate PhC structured OLEDs having various lattice constants and investigated the effect of the lattice constant of the periodic corrugation to the angular and spectral emissions <sup>19</sup>. These processes, however, require either very high pressure and temperature or vacuum process for the fabrication of the structure. It was also not very clear whether the enhancement is originated from the PhC effect or from the reflection from the corrugated metallic mirror or from the combined effects.

In this chapter, we report on corrugated OLEDs fabricated on polymer based PhCs to enhance the light extraction. The photonic crystals are fabricated using ultraviolet (UV)-NIL process at room-temperature and low-pressure, thereby it can be applied in large-area imprinting and in roll-to-roll fabrication process. Improvement of the efficiency in the corrugated OLEDs is achieved due to the coupling of the PhC effect on the polymer, anode and organic layers and the Bragg diffraction effect by the corrugated metallic mirror. The corrugated OLEDs with various PhC heights are fabricated and evaluated. FDTD calculation is carried out to understand the contribution of the coupling to PhC and the reflection from the corrugated metallic mirror to light extraction.

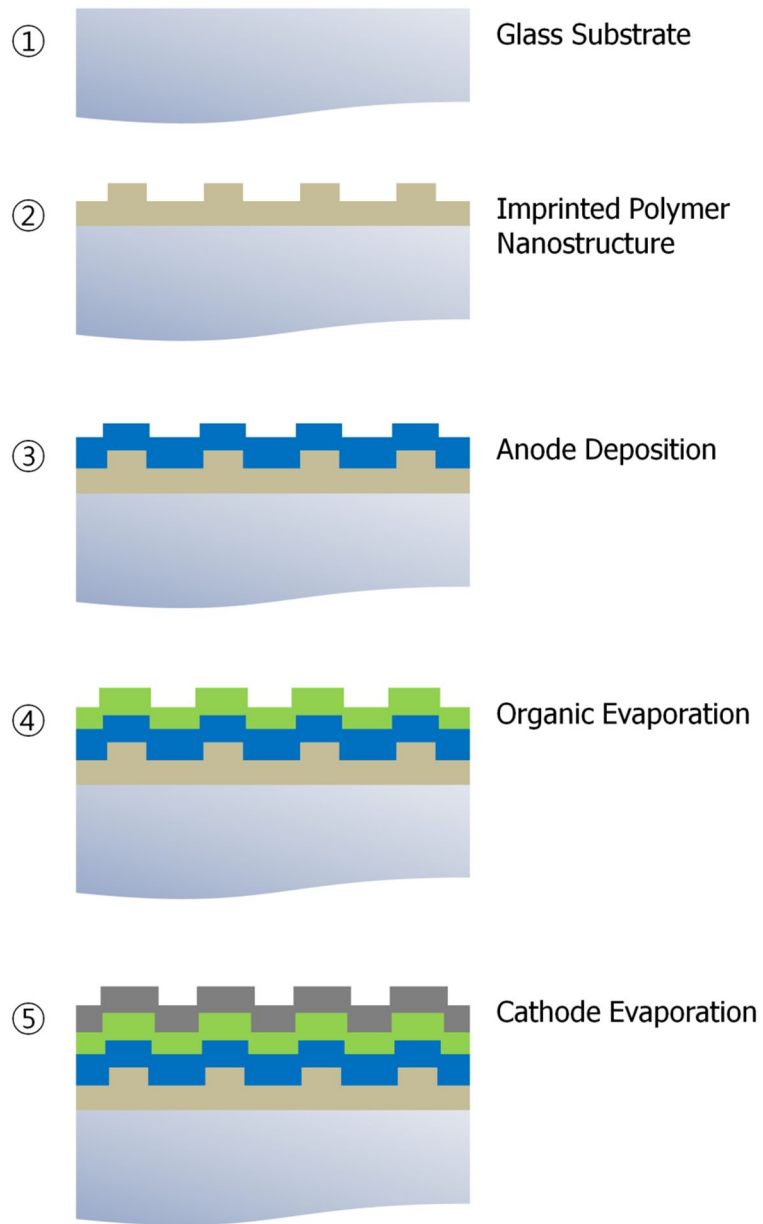


**Figure 5.1.** Fabrication process of corrugated OLEDs

## 5.2. Experimental

### 5.2.1. Corrugated OLEDs fabrication

Corrugated green emitting OLEDs were fabricated on PhC substrates and compared with a reference planar OLED without a PhC structure. The fabrication process is schematically represented in **Figure 5.1**. PhC patterns in silicon stamps were transferred to the polymer layer on glass substrates using UV-NIL. The silicon stamps were fabricated via DUV lithography and RIE. The lattice constant and diameter of the holes are 530 nm and 265 nm, respectively, and the depths of the holes are controlled by etching time to get 15 nm, 50 nm, 65 nm, 80 nm and 100 nm. The PhC patterns in the stamps have hexagonal lattice structures as shown in **Figure 5.2(a)**. The holes produce polymer circular pillars on the glass substrates by UV-NIL. OLEDs were fabricated on the PhC substrates by successively depositing a 300-nm-thick IZO layer by sputtering, 60-nm-thick 2TNATA (4,4',4''-Tris(N-(2-naphthyl)-N-phenyl-amino)-triphenylamine) as a hole injection layer, 20-nm-thick NPB (N,N'-diphenyl-N,N'-bis(1,1'-biphenyl)-4,4'-diamine) as a hole transporting layer, 60-nm-thick Alq<sub>3</sub> (tris-(8-hydroxyquinoline)-aluminum) as an emitting and electron transporting layer and 100-nm-thick LiF/Al as a cathode by thermal evaporation under high vacuum ( $\leq 10^{-7}$  torr), respectively. The current-voltage characteristics and the light-output power of the devices were measured using a Keithley 237 source measurement unit and a photodiode (Newport Model 818-UV) connected to an optical power meter (Newport Model 1835-C).

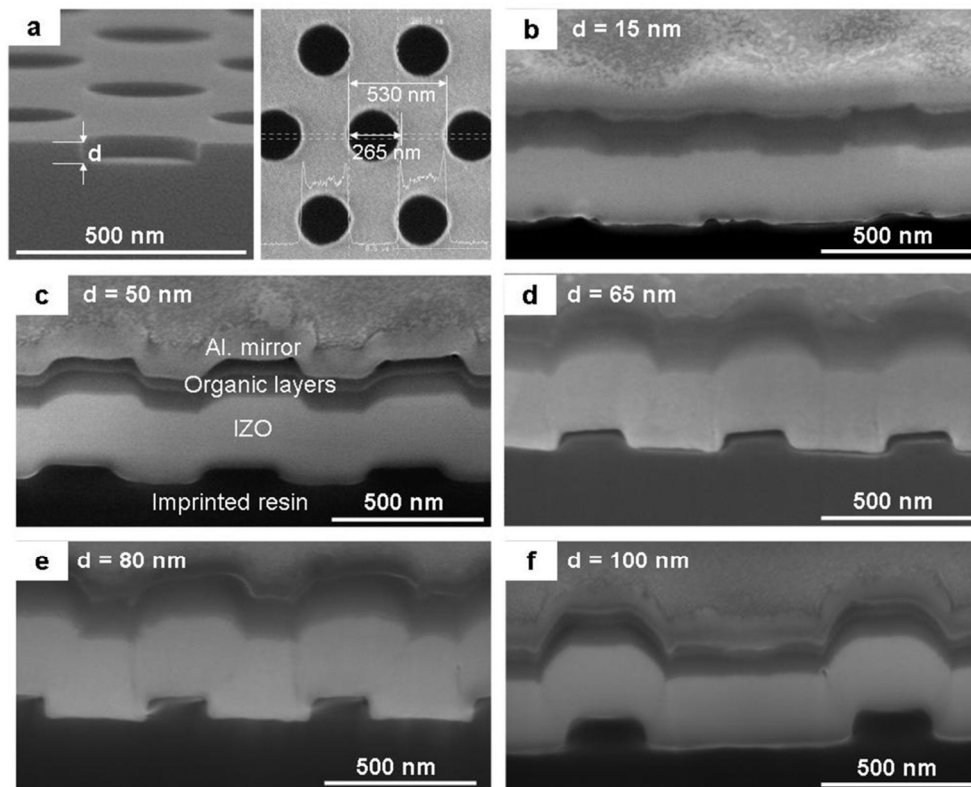


**Figure 5.2.** SEM image of one of the stamps used in the UV-NIL process (a), and DB-FIB images of the cross-sections of fabricated corrugated OLED samples with (b) 15 nm corrugation depth, (c) 50 nm corrugation depth, (d) 65 nm corrugation depth, (e) 80 nm corrugation depth and (f) 100 nm corrugation depth.

## 5.2.2. Characterization of corrugated OLEDs

**Figure 5.2** shows the cross-sectional images of the fabricated PhC structure of a stamp (a) and corrugated OLEDs (b-f). The images were obtained using high-resolution (field emission) ion imaging with dual-beam focused-ion-beam (DB-FIB) microscope (NOVA200). The images show multi-layers consisting of the PhC structures of the resin and the corrugated IZO, organic and aluminum layers. The OLEDs with pillar heights (corrugation depths) of 15 nm and 50 nm have perfectly conformal layers with the imprinted polymer pattern. On the other hand, the OLEDs fabricated on the PhC substrates with the pillars higher than 65 nm (Figure 5.2 (d-f)) showed cracks in the IZO layer and voids at the interface between the IZO and the organic layers. Void formation leads to unstable current distribution, resulting in a considerable decrease in the light emitting efficiency. Deposition of organic layers on the cracked IZO layer leads to the formation of sharp edges in the crevices, leading to high leakage current as described later. Therefore these high PhCs have larger electrical negative effect than optical advantage.

## 5.3. Electroluminescence Performance of Corrugated OLEDs

### 5.3.1. J-V-L characteristics of corrugated OLEDs

**Figure 5.3** displays the current-voltage (J-V) characteristics of the devices. The turn-on voltages of all the devices are approximately 3 V. It is interesting to note, however, that higher pillars in the PhC substrate result in higher current densities at a same voltage, and it is consistent with previous reports.<sup>13</sup> This is another important advantage of corrugated OLEDs to reduce the operating voltage and to improve the power efficiency. This phenomenon can be explained by the increase

of the interface area of the layers and by the enhancement of the electric-field intensity of the corrugated anode.<sup>14</sup>

### 5.3.2. Intensified CCD measurement

The electroluminescence (EL) intensities of the OLEDs were measured using an integrating sphere (Labsphere Co., 6" in diameter). The devices were attached to a port on the integrating sphere where the glass side faced the inside of the integrating sphere. A 20 mm hole in diameter was used as the port to collect all the forward emitted light including the diffracted light, which is larger than the active area ( $3\times 3\text{mm}^2$ ) of the devices. All the devices including the reference OLED were characterized using the same system. **Figure 5.4** shows the efficiency enhancement with respect to the current density and the electrical input power density. 49% enhancement of the light extraction with respect to the current density was obtained from the device having the corrugation depth of 50 nm. The improvement of the power efficiency is even higher. Remarkably high improvement of 93% was achieved with 50 nm pillars resulting from the decrease of the operating voltage as shown in Fig. 3. In our previous study, the improvement in the light extraction was 50% for SPhC-OLED with a corrugation depth of 265 nm having identical lattice constant and diameter.<sup>15</sup> The improvement in the power efficiency was almost the same as the luminous (current) efficiency, as there was no reduction in the operating voltage because of the existence of a planarization layer below the ITO layer. The superior power efficiency and the simple fabrication method of the corrugated OLEDs demonstrate that they are practically more meaningful than the SPhC-OLED.

### 5.3.3. Radiation profile of corrugated OLEDs

The variation of emission spectrum and intensity with viewing angle were measured using a rotating stage and optical fiber at the current of 1mA and are shown in **Figure 5.5(b)-(d)**. The reference OLED with planar substrate shows little change in the emission spectra and Lambertian pattern of emission intensity with viewing angle as expected. In contrast the OLED with the corrugation depth of 50 nm showed regularly fluctuated spectra and intensity with the angle.<sup>19</sup> Thereby the far-field radiation of the 50 nm corrugated OLED gets a profile similar to the shape of tulip as depicted in Figure. 5(d). The radiation profile of 10 nm-PhC OLED is almost the same as the Lambertian emission, but the diffraction wings are getting more apparent as the pillar height increases. In this way, the intensity at the angle about 30 degrees gets stronger and its shape becomes close to a butterfly wing which is consistent with our previous research.<sup>15</sup>

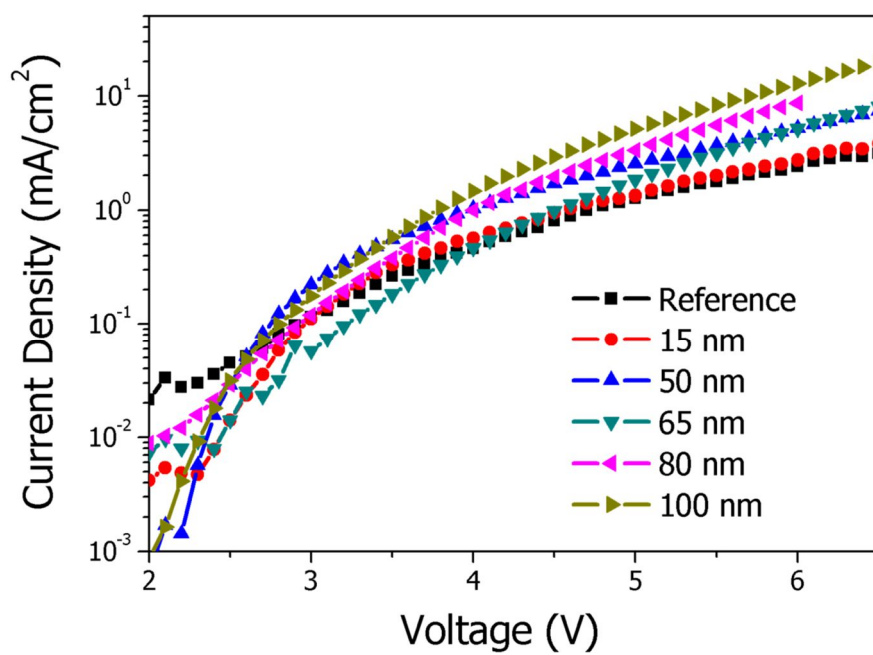


**Figure 5.3.** Voltage–current characteristics of the corrugated OLEDs with different corrugation depths.

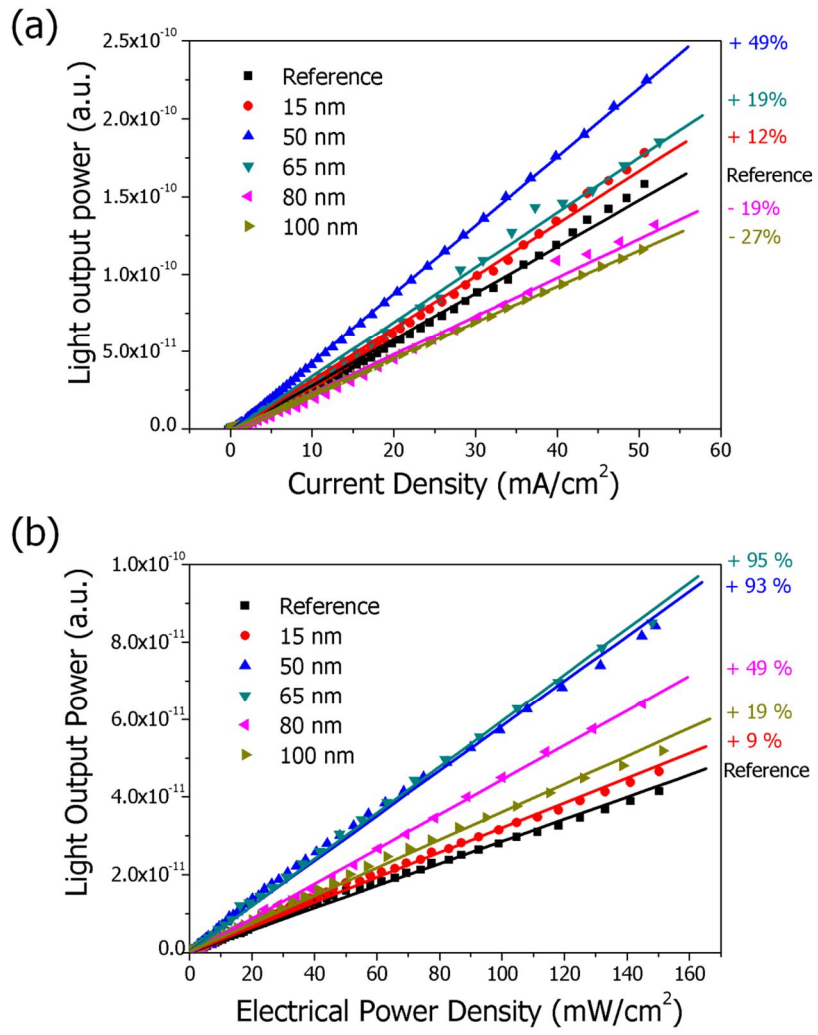


**Figure 5.4.** (a) Light-output power versus current density and (b) light-output power versus electrical input power density.

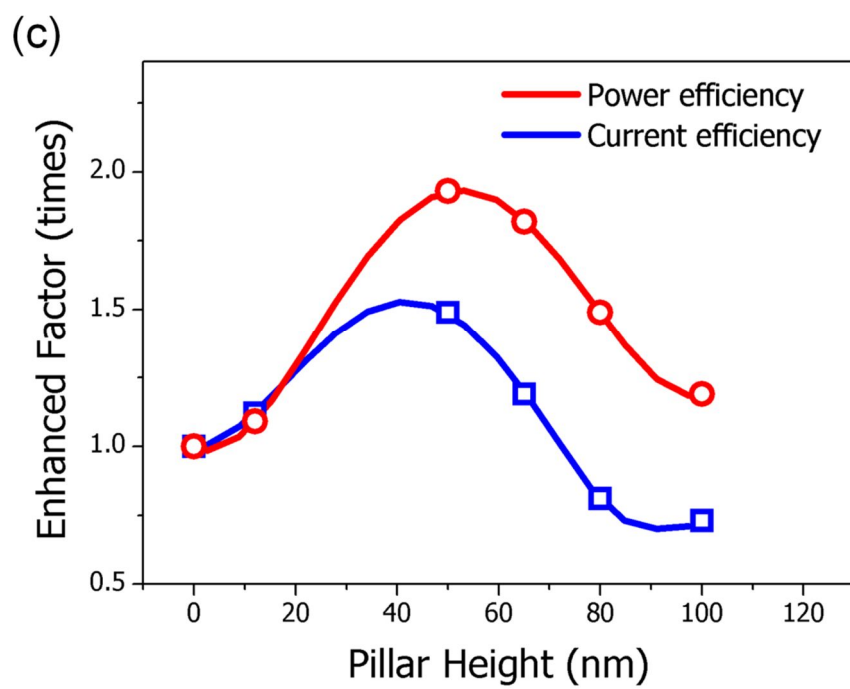


**Figure 5.4.** (c) The relative extraction efficiencies with respect to corrugation depth normalized to the OLEDs without pillars.

#### **5.3.4. Device stability and life time**

However, too high pillars resulted in uneven charge distribution and light emission induced from the uneven electrode as shown in **Figure 5.5**. The corrugated OLED fabricated on a 100 nm high PhC structure is not able to emit light uniformly. This effect may also accelerate the degradation of the OLED.

Device lifetime can be a significant issue in corrugated OLEDs because of the possibility of non-uniform film thickness, electric field distribution and current. It is true for large corrugation depth of 100 nm as displayed in Figure 5.5(a). Non-uniform distribution of emission intensities is apparent. In contrast, however, emission intensity of the OLED with the corrugation depth of 50 nm is uniform over the emission area. Moreover, the leakage current at low voltage is very low as displayed in Figure 5.3. These facts imply that the film thickness and the current are rather uniform without significant concentrated electric field if the corrugation depth is less than certain value, which turns out to be 50 nm in this study. Further study on the effect of corrugation depth on the device stability is going on and will be reported later.

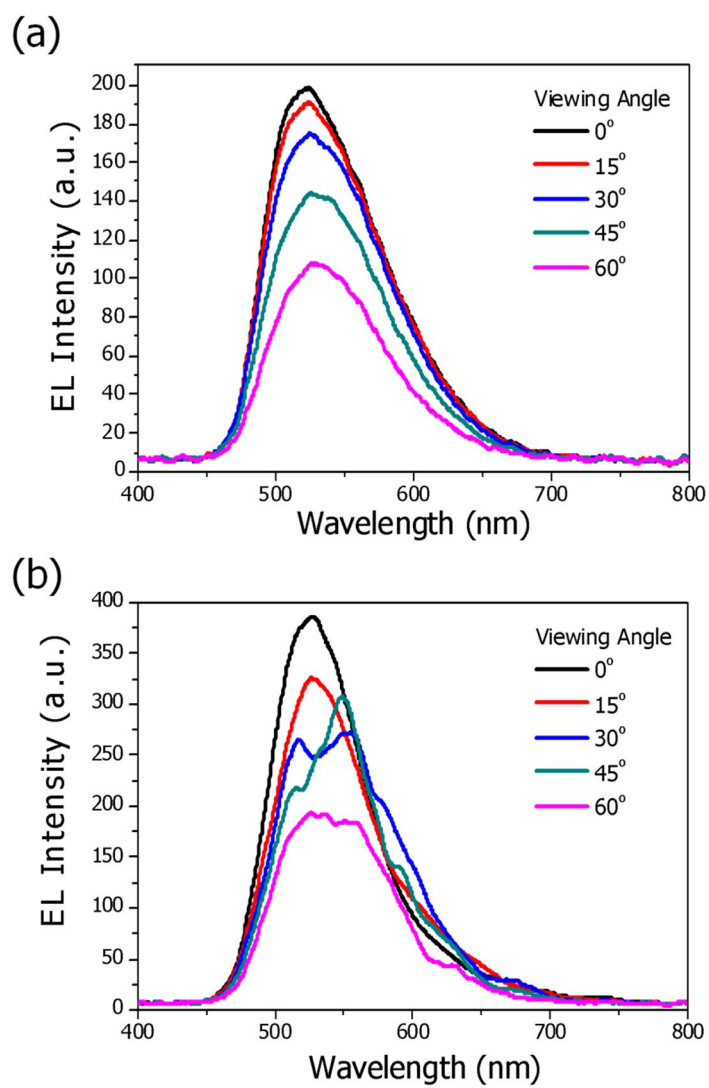


**Figure 5.5.** The angular emission characteristics of OLEDs with (a) planar and (b) 50 nm corrugated substrates.

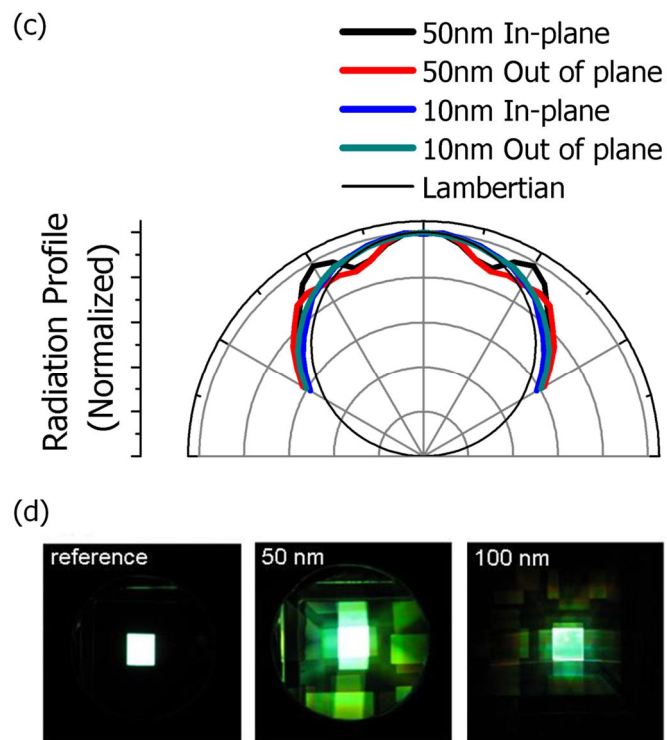


**Figure 5.5.** (c) The radiation profiles normalized by the EL intensity of reference device in the normal direction and (d) Photographs of the reference OLED and corrugated OLEDs with pillar heights of 50 nm and 100 nm.

## 5.4. FDTD Analysis

### 5.4.1. FDTD structure for Bragg gratings

In a corrugated OLED, as seen in Figure 5.2, the corrugation depth of the PhC layers and the metal grating can be considered as identical. However, as a future study, using certain planarization techniques, (such as sol-gel of high refractive index materials like  $\text{TiO}_2$  or  $\text{ZnO}$ ) according to the thickness of the coating layer and number of sol-gel steps a complete planarization can be attained as well as a partial planarization. In other words, PhC layers of the anode and organic layers can be designed to have a different corrugation depth from that of the metal grating. Therefore, it is important to have an insight on the relation of the corrugation depth with Bragg-diffraction and Bragg-reflection efficiencies, separately. Three sets of 3 dimensional (3D) FDTD simulations were performed using the structures shown in the inset of **Figure 5.6**. The first structure has a flat anode surface on a planarized PhC layer, i.e, single-layer PhC structured OLED having the effect of only Bragg-diffraction. The second set of the simulations was performed for the corrugated OLED with no polymer PhC structure to estimate the effect of the Bragg-reflection only. In this structure, the Bragg-diffraction effect on the anode and the organic layers must be negligible as the refractive index difference between the organic layers and the anode is very small. Finally, the simulations were performed for the multi-layer corrugated OLEDs. Corrugation depth was varied as a parameter in the simulations. Gaussian dipole sources were assumed to be located at the interface of NPB/Alq<sub>3</sub> with random distribution of dipole orientation. The number of dipoles was kept the same for all the structures in order to compare the extraction efficiencies from pure PhC effect and Bragg-diffraction even though the surface area of the emission layer in corrugated OLEDs increases as the corrugation depth increased.

## 5.4.2. Comparison FDTD and experimental results

**Figure 5.6** shows the result of simulations in which the improvement in the light extraction is compared in terms of corrugation depths. In the single layer PhC structured OLEDs, the light extraction efficiency increases linearly as the corrugation depth increases. This result indicates that large portion of emitted light can be extracted using high pillars if there is a method to fill up a gap with a high refractive and transparent material avoiding any void or defect. This is an expected result in accordance with previously reported findings.<sup>16</sup> The simulations were limited to corrugation depth below 300 nm in this device as the thickness of the anode was 300 nm. In the second case where the Bragg-reflection is the main factor in the improvement of the efficiency, the increase in the efficiency is substantial even at the corrugation depth of 50 nm and it reaches a peak value at the corrugation depth of 100 nm. Interestingly enough, however, the enhancement of the light extraction efficiency begins to decrease as the corrugation depth exceeds 100 nm. This simulation result can be explained as follows. When the corrugation depth exceeds a certain value, the deeper metal pit causes random phased electromagnetic waves due to multi-reflection and diffraction from the metal surface and side walls. Energy absorption by the surface plasmon from the metal surface leads to the reduction of the light extraction as well. These factors reduce the amount of Bragg-reflected light waves, resulting in less improvement of efficiency.<sup>22</sup> The light extraction in the third structure was further enhanced by the PhC structure. The enhancement of extraction is dominated by the Bragg-reflection from the corrugated organic and metallic layers if the height of nanostructure is below 100 nm. Combined effect of light extraction becomes the maximum at the corrugation depth of 100 nm. This result suggests that further improvement of the light extraction than 49% achieved in this experiment is possible by using the corrugated OLEDs with the corrugation depth of 100 nm if we can prevent the formation of cracks and sharp edges in IZO layer, thereby to have good electrical contact.

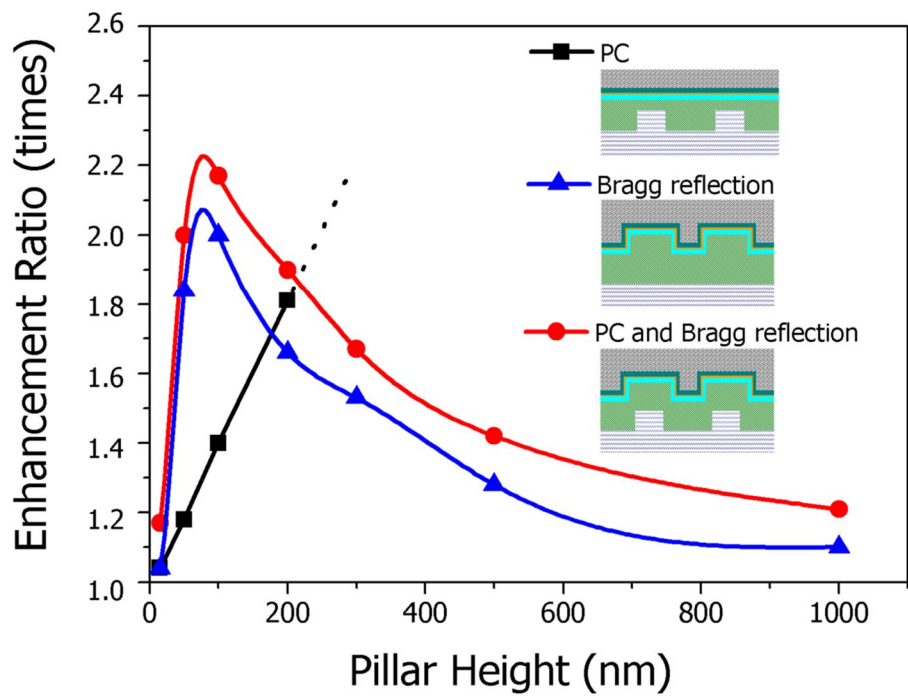


**Figure 5.6.** FDTD simulated relative light extraction efficiency versus the corrugation depth for three different structures shown in inset.

## 5.5. Conclusions

High-efficiency corrugated OLEDs were fabricated on PhC structured substrates using UV-NIL process at room-temperature and low-pressure. The Bragg-diffraction effect on the PhCs of substrate, anode and organic layers and the Bragg-reflection from the corrugated metal mirror result in high light extraction efficiency even with a sub-100 nm corrugation depth. Furthermore the corrugated anode structure reduces the operating voltage. As a result, 93% enhancement of the power efficiency was obtained from an OLED even with a very shallow corrugation depth of 50 nm compared to the reference OLED with planar structure. The roles of corrugated metal mirror and PhC layers on the efficiency enhancement were separately examined through FDTD analyses. The analyses showed that the increase in the efficiency reaches a peak value at a critical corrugation depth of 100 nm and the major enhancement comes from the Bragg-reflection by the corrugated metal mirror.

## 5.6. Bibliography

1. G. Gu, D. Z. Garbuzov, P. E. Burrows, S. Venkatesh, S. R. Forrest and M. E. Thompson, *Opt. Lett.* 22 (1997) 396.
2. N. C. Greenham, R. H. Friend and D. D. C. Bradley, *Adv. Mater.* 6 (1994) 491.
3. C. F. Madigan, M. H. Lu and J. C. Sturm, *Appl. Phys. Lett.* 76 (2000) 1650.
4. J. J. Wierer, M. R. Krames, J. E. Epler, N. F. Gardner, M. G. Craford, J. R. Wendt, J. A. Simmons and M. M. Sigalas, *Appl. Phys. Lett.* 84 (2004) 3885.
5. R. Windisch, P. Heremans, A. Knobloch, P. Kiesel, G. H. Dohler, B. Dutta and G. Borghs, *Appl. Phys. Lett.* 74 (1999) 2256.
6. I. Schnitzer, E. Yablanovitch, C. Canau, T. J. Gmitter and A. Scherer, *Appl. Phys. Lett.* 63 (1993) 2174.
7. T. Tsutsui, M. Yahiro and H. Yokogawa, *Adv. Mater.* 13 (2001) 1149.

8. R. H. Jordan, L. J. Rothberg, A. Dodabalapur and R. E. Slusher, *Appl. Phys. Lett.* 69 (1996) 1997.
9. A. Kock, E. Gornik, M. Hauser and K. Beinstingl, *Appl. Phys. Lett.* 57 (1990) 2327.
10. J. M. Lupton, B. J. Matterson, I. D. W. Samuel, M. J. Jory and W. L. Barnes, *Appl. Phys. Lett.* 77 (2000) 3340.
11. T. Kim, P. O. Leisher, A. J. Danner, R. Wirth, K. Streubel and K. D. Choquette, *IEEE Photonics Technol. Lett.* 18 (2006) 1876.
12. Y. C. Kim, S. H. Cho, Y. W. Song, Y. J. Lee, Y. H. Lee and Y. R. Do, *Appl. Phys. Lett.* 89 (2006) 173502.
13. K. Ishihara, M. Fujita, I. Matsubara, T. Asano, S. Noda, H. Ohata, A. Hirasawa, H. Nakada and N. Shimoji, *Appl. Phys. Lett.* 90 (2007) 111114.
14. M. Fujita, T. Ueno, K. Ishihara, T. Asano, S. Noda, H. Ohata, T. Tsuji, H. Nakada and N. Shimoji, *Appl. Phys. Lett.* 85 (2004) 5769.
15. S. Jeon, J. W. Kang, H. D. Park, J. J. Kim, J. R. Youn, J. Shim, J. H. Jeong, D. G. Choi, K. D. Kim, A. O. Altun, S. H. Kim and Y. H. Lee, *Appl. Phys. Lett.* 92 (2008) 223307.
16. Y. J. Lee, S. H. Kim, J. Huh, G. H. Kim, Y. H. Lee, S. H. Cho, Y. C. Kim and Y. R. Do, *Appl. Phys. Lett.* 82 (2003) 3779.
17. A.M. Adawi, R. Kullock, J.L. Turner, C. Vasilev, D.G. Lidzey, A. Tahraoui, P.W. Fry, D. Gibson, E. Smith, C. Foden, M. Roberts, F. Qureshi and N. Athanassopoulou, *Org. Elec.* 7 (2006) 222.
18. S. Fan, P. R. Villeneuve, J. D. Joannopoulos and E. F. Schubert, *Phys. Rev. Lett.* 78 (1997) 3294.
19. U. Geyer, J. Hauss, B. Riedel, S. Gleiss, U. Lemmer and M. Gerken, *Jour. Appl. Phys.* 104 (2008) 093111.
20. P. A. Hobson, S. Wedge, J. A. E. Wasey, I. Sage and W. L. Barnes, *Adv. Mater.* 14 (2002) 1393.
21. C. J. Yates, I. D. W. Samuel, P. L. Burn, S. Wedge and W. L. Barnes, *Appl. Phys. Lett.* 88 (2006) 161105.

# Chapter 6

## Corrugated OLEDs Embedding VNHA

---

### 6.1. Introduction

Organic Light Emitting Device (OLED) has been successfully applied to mobile devices and its applications are being extended to large-area light and displays. However, several problems still remain unsolved for the practical applications and the most important issues are the power consumption and lifetime.

The most effective way to solve all of the issues is the light extraction enhancement by inserting nano- and micro-scale structures. Accordingly, until now several studies have been done and those can be summarized in the three cases. In the first case, the microstructures such as micro lens array are attached on the top of glass substrate in order to decrease the light loss at the glass/air interface.<sup>1 2</sup> In the second case, the nano- and micro-scale structures as an intermediate layer, such as photonic crystal array, low-index grids and particles, are inserted into the OLED.<sup>3 4 5 6</sup> In those cases, the light wasted by substrate and waveguide modes decreases. In the third case, on the other hand, all layers of the OLED are corrugated by inserting nano- and micro-scale structures.<sup>7 8 9 10 11 12</sup> The losses caused by substrate mode, waveguide mode and surface plasmon polaritons on metal electrode are reduced. In addition, the light extraction efficiency increases due to Bragg reflection effect.

According to a finite difference time domain (FDTD) analysis, as the

corrugation pattern increases in depth, the light extraction efficiency increases. However, if the nanopattern height exceeds 50 nm, then the device lifetime could be decreased because of electrical instability between organic layers and electrodes.<sup>8 12</sup> In previous study, sub-100 nm deep nanopattern was used in general. In addition, the nanopattern depths of OLED layers could not be controlled individually for enhancing the light extraction, because the OLED layers were deposited in sequence on a patterned substrate.

In this chapter, we propose a multiple nano hole array embedded (MNHA) OLED for highly enhanced light extraction. The MNHA with asymmetric nanostructures is composed of vacuum nano-hole arrays (VNHA) in contact with substrate and corrugation nano-array (CNA) adjacent to transparent electrode. Especially it is investigated that the distorted metal surface due to CAN pattern strongly affects the enhancement by occurring the localized surface plasmon resonance (LSPR) around at the organic-metal interface.

## **6.2. Multiple Nano Patterned Substrate**

### **6.2.1. MNHA fabrication**

The MNHA is designed to maximize the light extraction by reducing dramatically the losses caused by substrate mode, waveguide mode and surface plasmon polaritons, and by increasing Bragg reflection effect as well as to maintain electrical stability. The vacuum NHA ( $n_{\text{low}}=1$ ) is embedded to extract effectively the light trapped in the waveguide mode into the air through maximizing RI contrast for the given background material,  $\text{Si}_3\text{N}_4$  ( $n_{\text{high}}=2.02$ ). The hole depth of the vacuum NHA is set to be several 100 nm-scale to maximize light diffraction. The CNA is formed for making a corrugated OLED in order to add Bragg

reflection effect and decrease the light lost by surface plasmon polaritons. The pattern depth of the CNA is set to be several 10 nm-scale to maintain electrical stability.

The MNHA was fabricated using a robust reverse-transfer (R<sup>2</sup>T) process and additional patterning process.<sup>13</sup> The R<sup>2</sup>T process is used for generating the vacuum NHA inside of the Si<sub>3</sub>N<sub>4</sub> slab and the CNA is formed over the Si<sub>3</sub>N<sub>4</sub> slab by using a conventional lithography.

**Figure 6.1a** shows a schematic diagram for fabrication of the MNHA embedded OLED (MNHA-OLED). First, an 800nm thick Si<sub>3</sub>N<sub>4</sub> film was deposited on the silicon substrate by means of plasma-enhanced chemical vapor deposition and then a hexagonal hole array was introduced on the silicon nitride film by using the KrF photolithography and dry etch process. The nano-hole embedded Si<sub>3</sub>N<sub>4</sub> on the silicon substrate and the glass wafer were bonded using the anodic bonding procedure and the bonded wafers were dipped in a KOH solution to remove the silicon substrate. Finally hexagonal hole array was formed over the Si<sub>3</sub>N<sub>4</sub> layer with the vacuum nano-hole array (NHA) by using the KrF photolithography and dry etch process. The MNHA fabrication process, to be almost a defect-free process, was based on the 8-inch wafer process, and then OLEDs devices were fabricated on diced substrate into 25×25 mm<sup>2</sup>. The following layers, consisting of inorganic (IZO(150 nm)), organic (2TNATA/NPB/Alq<sub>3</sub>(140 nm)) and metal (LiF/Al(1/100 nm)) materials, were deposited over the MNHA under high vacuum whose pressure was around 10<sup>-7</sup> Torr. In general, inorganic materials have a low gas permeability, thus it is expected that the nano-holes were at vacuum state, although it is not possible to measure the pressure directly in the nano holes. Furthermore, the RI (i.e. speed of light in the medium, wavelength) is not changed whether the nano holes are at vacuum state or filled with some gases. Subsequently, the extraction properties are not changed as well.

### 6.2.2. MNHA substrate characterization

Each layer thickness of the OLED device is determined by optimizing the control device (OLEDs integrated on the bare glass), and the extraction structure is examined and improved from the optimized control device which has high efficiency of 5.04 cd/A. **Figure 6.1b** shows Focused Ion Beam (FIB) images of the MNHA on a glass substrate and **Figure 6.1c-d** show the vertical structures of the MNHA embedded OLED (MNHA-OLED). Photoluminescence (PL) and electroluminescence (EL) experiments were analyzed by the three dimensional finite difference time domain (FDTD) simulation based on a small molecule bottom emitting OLED using the emitter, tris-(8-hydroxyquinoline) aluminum ( $\text{Alq}_3$ ) which has a random orientation of dipoles.

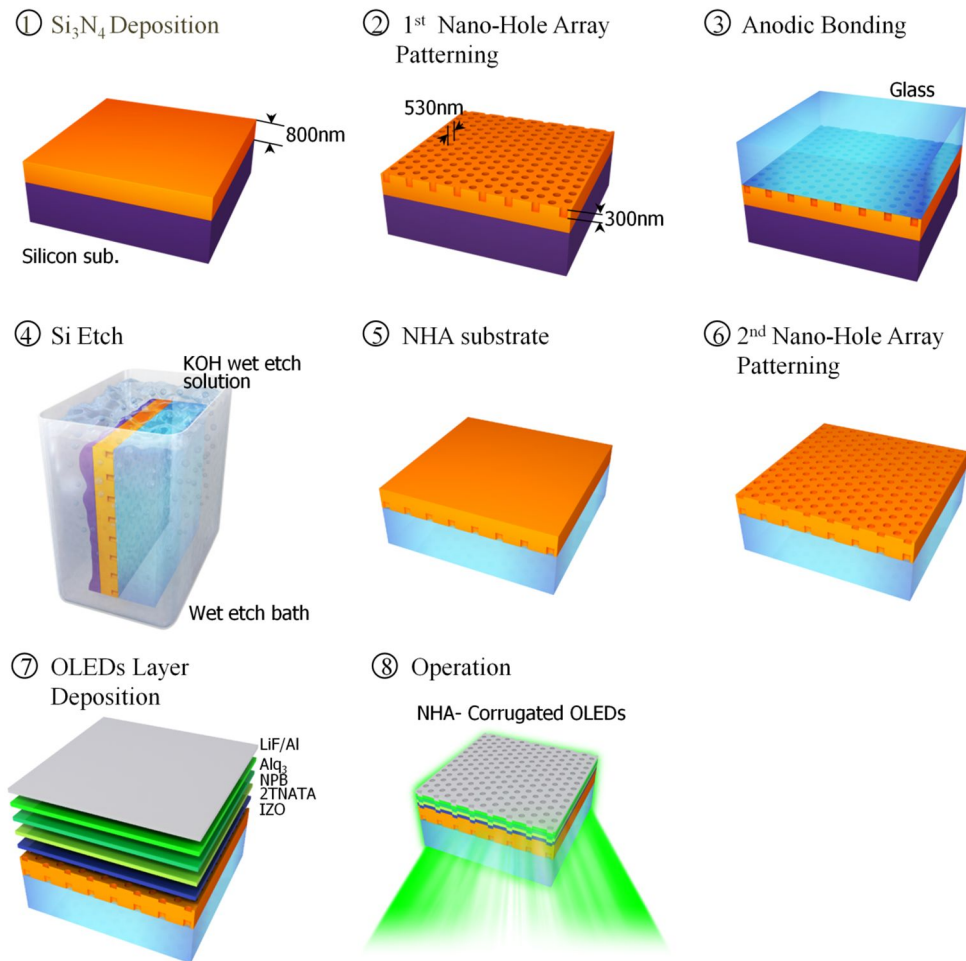


**Figure 6.1.** (a) A schematic diagram for fabrication of the Both-side Nano-hole Patterned Intermediate(MNHA) OLED using the R<sup>2</sup>T and following nanopatterning process.

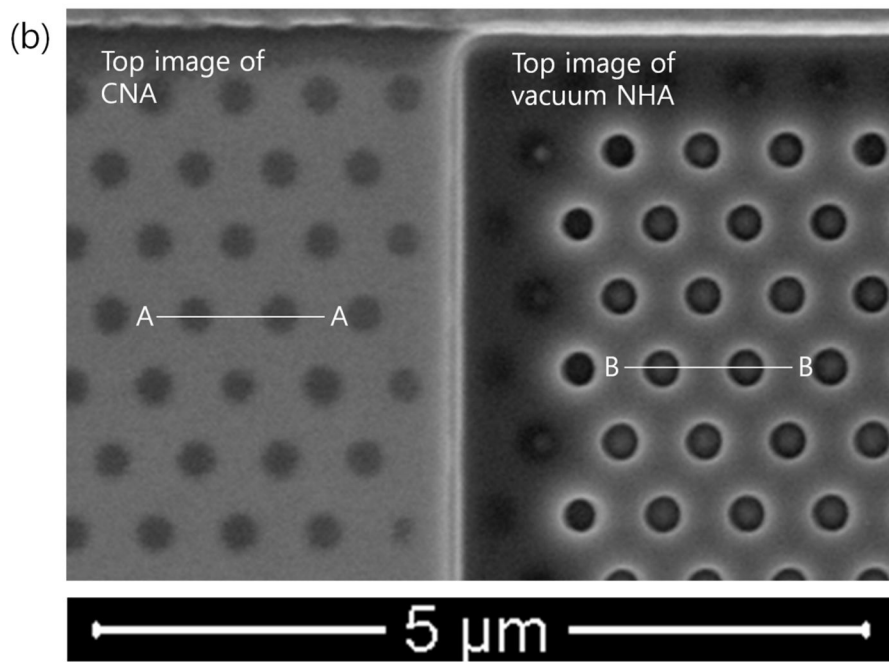


**Figure 6.1.** (b) Focused Ion Beam (FIB) images of the MNHA on a glass substrate.

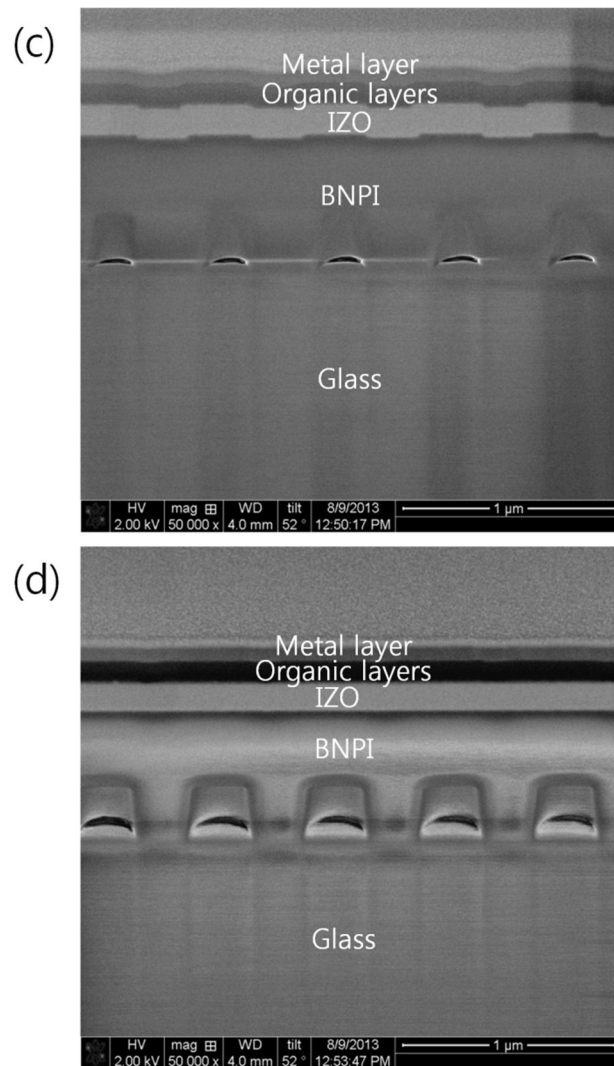


**Figure 6.1.** (c) cross sectional image of the MNHA embedded OLED (MNHA-OLED) along the line A-A'. and (d) cross sectional image of the MNHA-OLED along the line B-B'

## 6.3. FDTD Analysis

### 6.3.1. Corrugated OLEDs embedding VNHA

FDTD simulation was carried out to predict the extraction efficiency of the PC embedded OLEDs. The simulation is performed for the corrugated OLED structure, consisting of an Al cathode, organic material, anode, glass, and the inserted MNHA. The lattice constant ( $\Lambda$ ) of the vacuum NHA was set to be 530 nm, the same as the emission peak wavelength of Alq<sub>3</sub> photoluminescence (PL), because the extraction efficiency becomes largest when the lattice constant is similar to the vacuum wavelength. A hole diameter of  $0.5\Lambda$  and hole height of 300 nm of the vacuum NHA were chosen because the light extraction varied as a function of hole depth and was saturated when the hole depth reached the value of the height. The RI value of the  $n_{\text{low}}/n_{\text{high}}$  of the vacuum NHA is 1.0/2.02. A pitch of 530 nm and depth of 50 nm of the CNA were set, because the corrugated OLED with the depth of less than 50 nm is electrically stable.

The FDTD simulations are carried out to elucidate the surface plasmon polaritons. In general, surface plasmon changes when they propagate on metal surfaces that are periodically textured on the scale of the wavelength of light.<sup>14 15-</sup>  
<sup>19</sup> **Figure 6.2** shows results of the FDTD analysis. Each point represents the time integration values of the Poynting energy in the z direction ( $P_z$ ) obtained by dividing the spectrum of the MNHA-OLED by that of the reference (on bare glass) OLED. The Poynting energy is integrated over the xy-surface in glass. **Figure 6.3** shows contours of electric field intensities induced from the dipoles according to their relative distance from the metal pattern. The FDTD results verified that the localized surface plasmon resonance (LSPR)<sup>14 20</sup> strongly arises around at the metal pattern. The FDTD calculation was carried out for a vertical dipole because surface plasmon polaritons only exist for TM polarization.<sup>21</sup> One dipole is located right next to the metal pattern and the electric field is detected at 25 nm (middle of

the metal), 50 nm height (top of the metal) and 75 nm (in dielectric) from the metal bottom. The other dipole is located between the metal rods and the electric field is detected at 25 nm (middle of the metal), 50 nm height (top of the metal) and 75 nm (in dielectric) from the metal bottom. The Poynting energies with or without metal pattern were also calculated to confirm the contribution of LSPR structure. **Figure 6.4** represents FDTD results (a) in the case of no metal mirror and (b) in the case of corrugated metal mirror. It is useful to compare the FDTD and experimental results of photoluminescence and electroluminescence, and it will be dealt with later.

It should be noted that the glass substrate was not included in the FDTD simulation because the glass substrate has the thickness about three orders of magnitude larger than that of the other layers in the OLED device.

Figure 6.1b shows the top view images of VNHA and CNA. In Figure 6.2a, we can see the misalignment in the overlay alignment process of KrF lithography. The x and y deviations of nanohole centers were measured to be 35 nm and 117 nm, respectively. The grid for the FDTD analysis was generated by considering the misalignment. The x and y positions of the dipoles were determined based on CNA. Those are located at 50 nm away from the corrugated metal electrode in z direction. As shown in Figure 6.2a, the observed Poynting energy increases for all vertical dipole ( $d_z$ ) positions as the vacuum NHA and MNHA are embedded to the OLED. Especially, in the case of the MNHA, the Poynting energy induced from the vertical dipoles is most improved. The results show that the MNHA can be effectively used for enhancing the extraction of the OLED for general lighting.

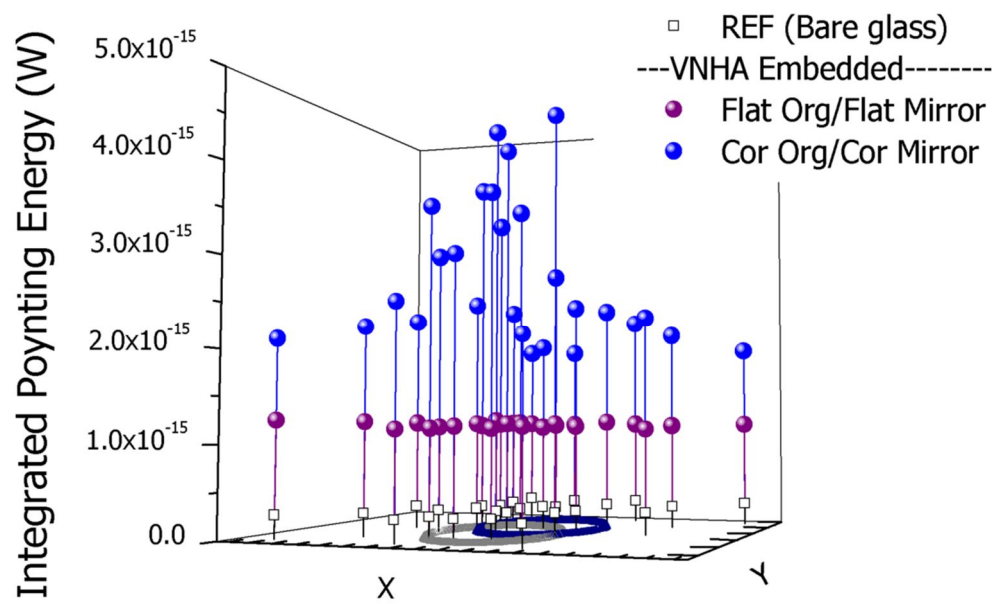


**Figure 6.2.** 3D graph of FDTD simulated integrated Poynting energies according to the substrate.

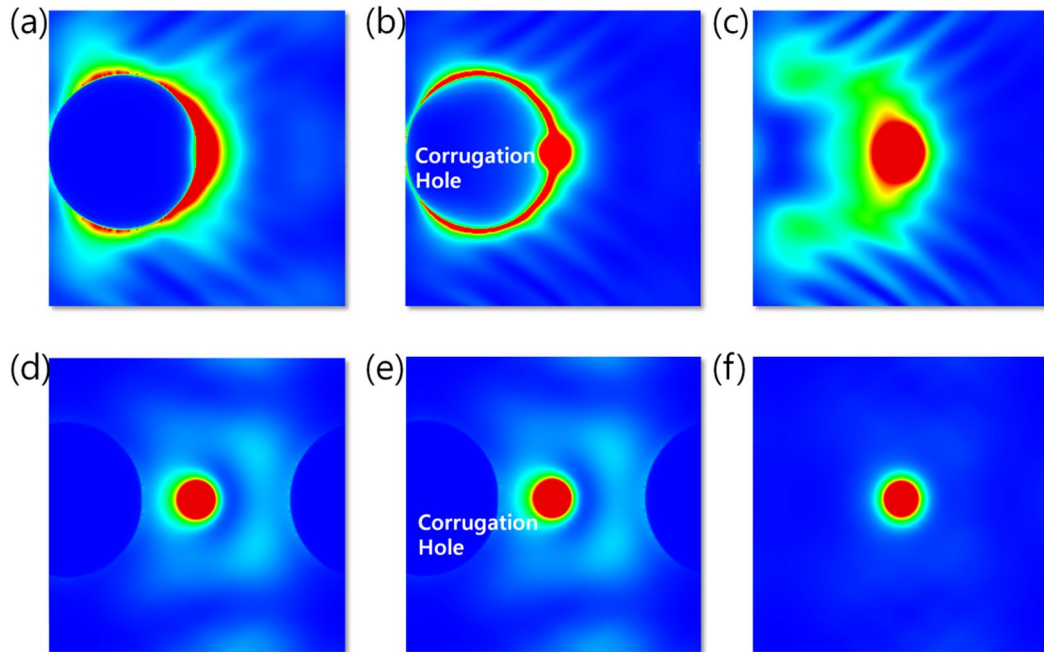


**Figure 6.3.** Contours of electric field intensities induced from the dipoles according to their relative distance from the metal pattern. One dipole is located right next to the metal pattern and the electric field is detected at (a) 25 nm (middle of the metal), (b) 50 nm height (top of the metal) and (c) 75 nm (in dielectric) from the metal bottom. The other dipole is located between the metal rods and the electric field is detected at (d) 25 nm (middle of the metal), (e) 50 nm height (top of the metal) and (f) 75 nm (in dielectric) from the metal bottom.

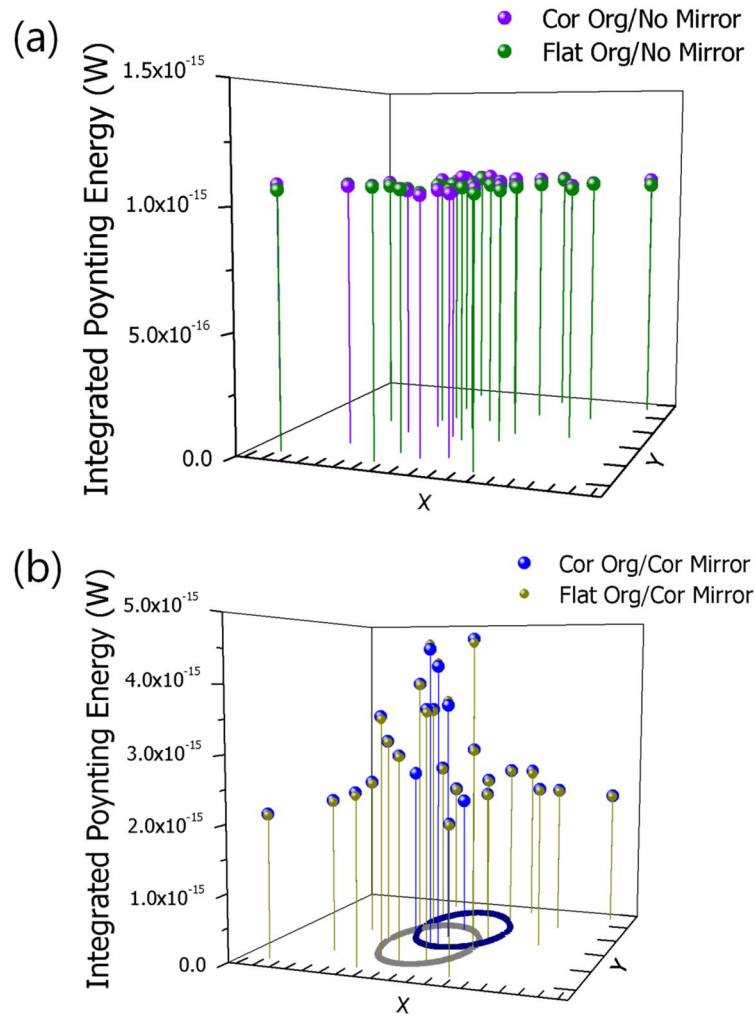


**Figure 6.4.** FDTD results (a) in the case of no metal mirror and (b) in the case of corrugated metal mirror.

### 6.3.2. The Poynting Energy depending on the Overlay Shift

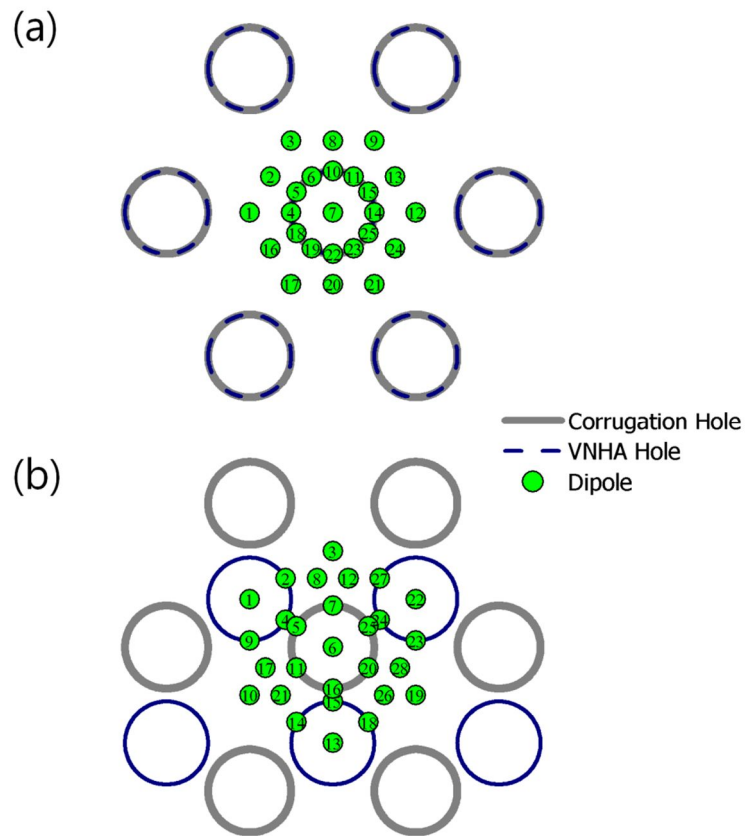


**Figure 6.5.** Schematic diagram of the VNHA and corrugated holes and the dipole position applying to the FDTD analysis according to overlay shift: (a) Eclipsed and (b) staggered positions.

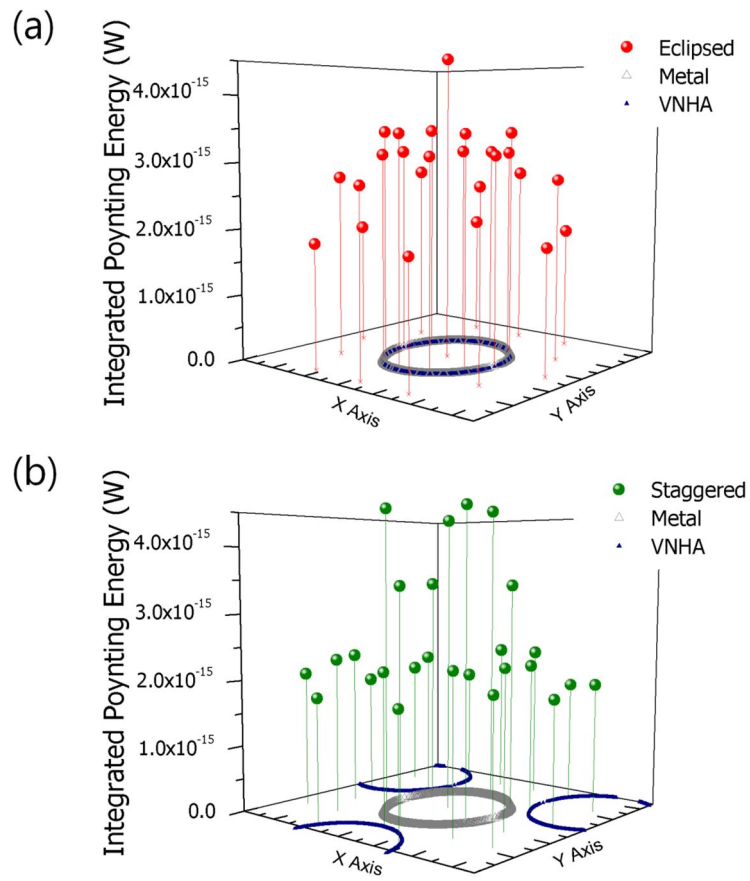


**Figure 6.6.** Integrated Poynting energy simulated by FDTD analysis according to overlay shift: (a) Eclipsed and (b) staggered positions.

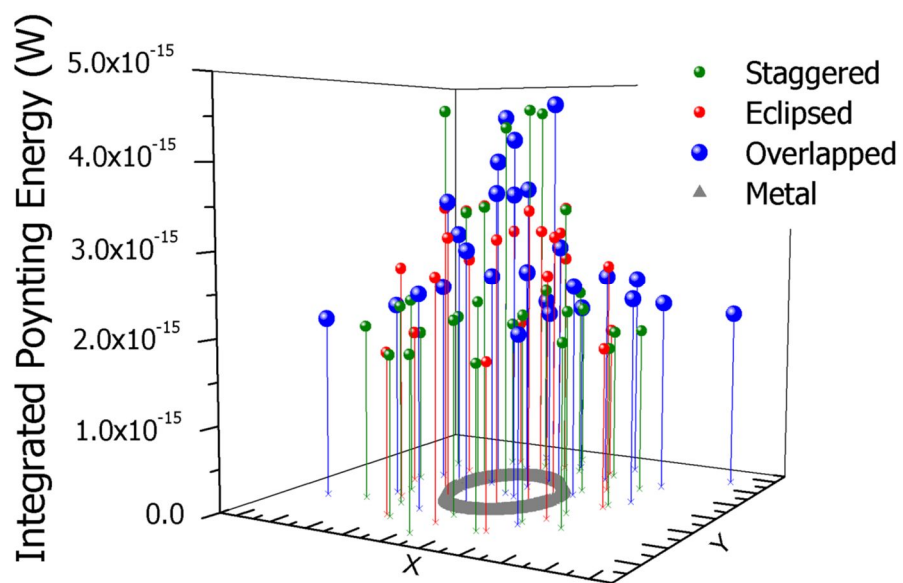


**Figure 6.7.** Integrated Poynting energy simulated by FDTD analysis according to overlay shift: Eclipsed/ Staggered/ Mismatched positions

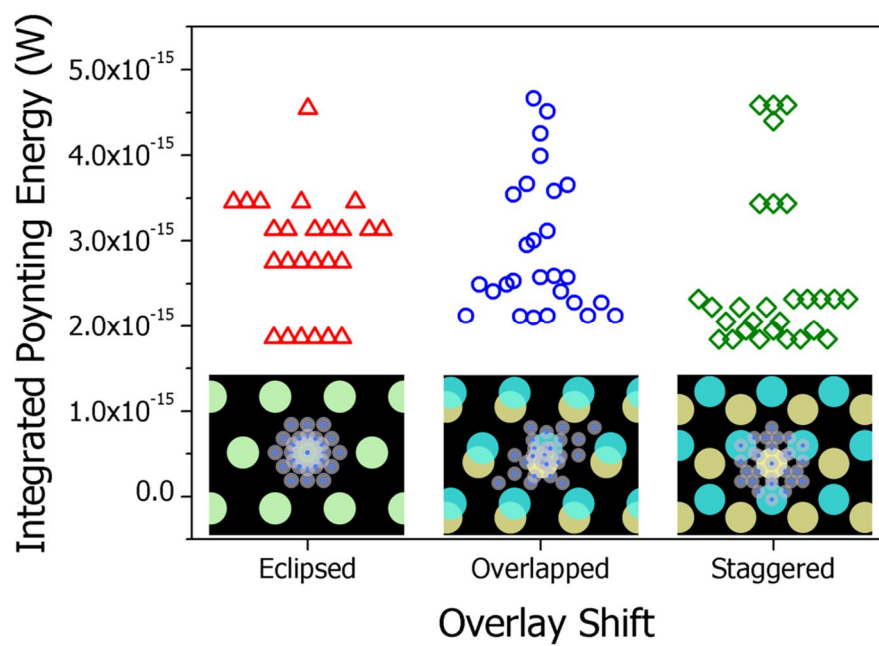


**Figure 6.8.** FDTD analysis results: (a) Integrated Poynting energies according to different dipole positions in the different MNHA substrates modeled by varying the overlay shift between CNA and VNHA

## 6.4. Angular Photoluminescence

Prior to fabricating the OLEDs, the angular dependence of the photoluminescence (PL) is measured and compared with the numerical simulation.<sup>22,23</sup> The schematic diagram of PL intensity measurement is illustrated in the supporting information. **Figure 6.9 and 6.10** show the p- and s-polarized light emission from the waveguide mode for the wavelength of 520 nm, corresponding to the PL peak wavelength of the organic molecules. It is meaningful that the measured PL intensity is compared with that of the FDTD simulation because both results showed improvement from the waveguide mode, not from the glass mode, and the results are consistent with each other.

In the case of the p-polarized light induced from the  $d_x$  and  $d_z$  dipoles for the MNHA-OLED, the PL intensities in in-plane and out-plane directions are significantly improved for most of viewing angles (over five times at most for certain angles), whereas the enhancement is smaller for the s-polarized light induced from the  $d_y$  dipole as shown in Figure 6.9 and 6.10. The results in Figure 6.9 are consistent with the FDTD analysis results.

On the other hand, Figures 3c-d show that the enhancements of MNHA-OLED are somewhat smaller than VNHA-OLED unlike the FDTD analysis results. It is because PL samples do not include any corrugated metal layer to play the role of an electrode and mirror. It is demonstrated that the 50-nm deep corrugation of transparent electrode and organic layers not only slightly affect on the light extraction, but rather could adversely affect.

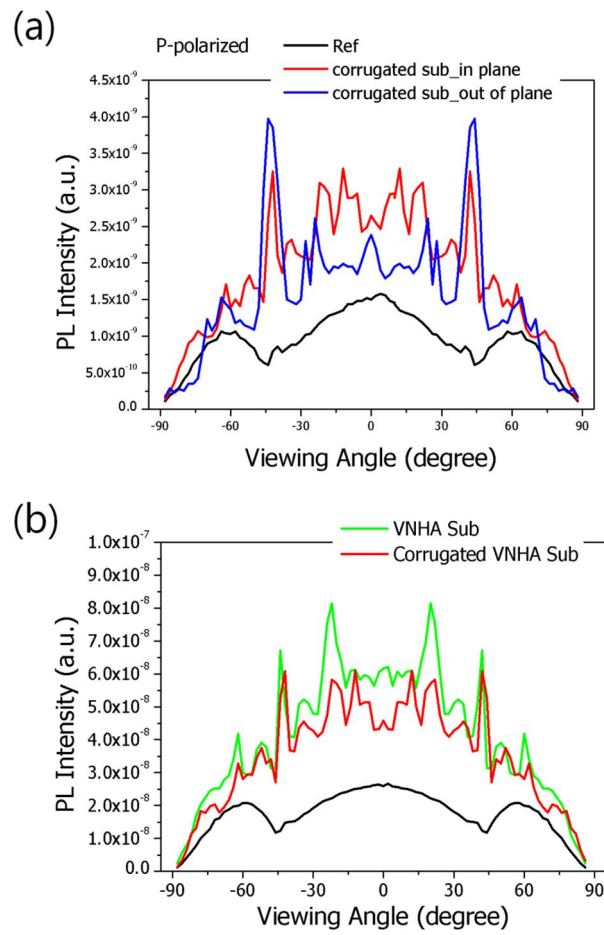


**Figure 6.9.** P-polarized angular PL intensity measured as a function of the viewing angle. (a) Corrugated VNHA substrate and (b) comparison with the VNHA and corrugated VNHA substrate.

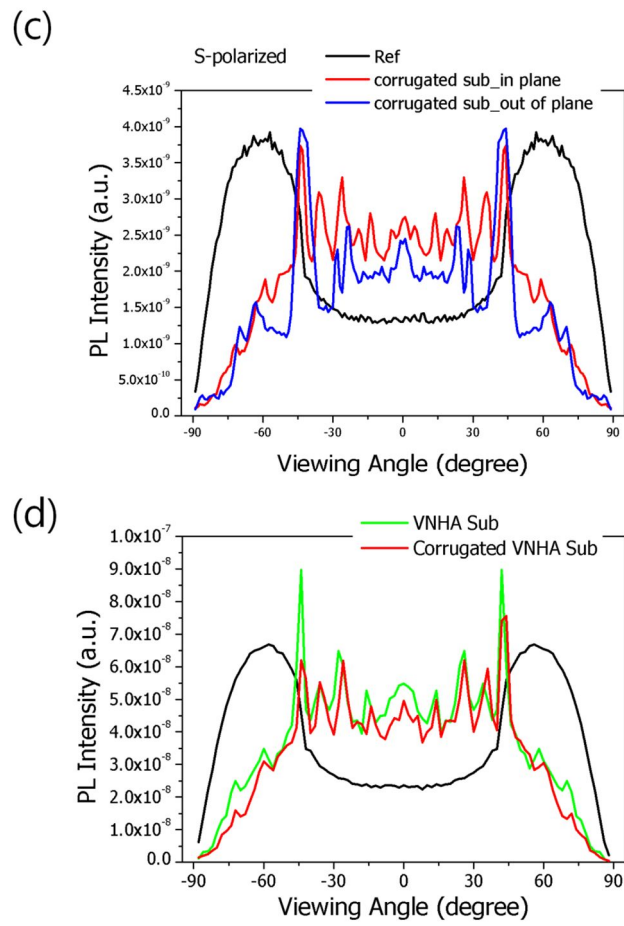


**Figure 6.10.** S-polarized angular PL intensity measured as a function of the viewing angle. (a) Corrugated VNHA substrate and (b) comparison with the VNHA and corrugated VNHA substrate.

## 6.5. Electroluminescence

### 6.5.1. Intensified CCD measurement

**Figure 6.11a** shows the device performance of the MNHA-OLED and reference OLED. The EL intensity of each device was measured using an integrating sphere to detect the light emitted into the air in all directions. The experimental data were obtained from the representative device selected among more than a dozen cells. The EL intensity of each device was measured using an integrating sphere to detect the light emitted into the air in all directions. The experimental data were obtained from the representative device selected among more than a dozen cells. The EL intensity is the spectra accumulated 100 times by controlling the recording system of the measurement. It was found by integrating over the entire wavelength range of 414 to 753 nm that the relative spectrum was improved by 2.22 times when the MNHA-OLED was compared with the reference one. The enhancement factor was obtained by dividing the spectrum of the MNHA-OLED by that of the reference at each wavelength. The maximum value of the enhancement factor is 2.61 and the maximum enhancement was obtained at the maximum peak of the spectrum, which means that the inserted MNHA did not cause a spectrum shift or a change of color coordinates. The results are summarized in **Table 6.1**.

The EL intensity was also measured for each device by attaching a 10 mm diameter hemisphere lens to the device. Insertion of a nanostructure between an anode and the glass substrate affects not only the emitted light from the organic layer but also the re-entering light due to total internal reflection (TIR) at the glass-air interface. The observed light in the air is the combination of the light extracted from the waveguide and glass modes into the air mode. Therefore, we can exclude TIR by attaching a hemisphere lens at the glass-air interface and making a spherical surface such that the light which reaches the glass directly should escape from the device. Magnitude of the waveguide loss, which is converted into light by

modifying the interface between the organic anode and the glass, can be determined quantitatively by comparing the two devices with hemisphere lenses attached. The relative values are represented in parentheses in Table 1 and the values in the parentheses mean that the extracted energy is increased by about 80% from the waveguide mode due to the nanostructure. When the wavelength gets closer to the maximum peak, both loss modes are converted into the radiation mode and thus the extraction enhancement is maximized at the peak wavelength.

The enhancement factor was calculated as a function of the wavelength by dividing the emission spectra of the MNHA-OLED by that of the OLED without the nanostructure in order to evaluate the wavelength dependence of the emission. As shown in **Figure 6.11b**, the enhancement factor has a maximum value at the same wavelength as the peak of the emission spectra and shape of the enhancement factor curve is similar to that of the emission spectra.

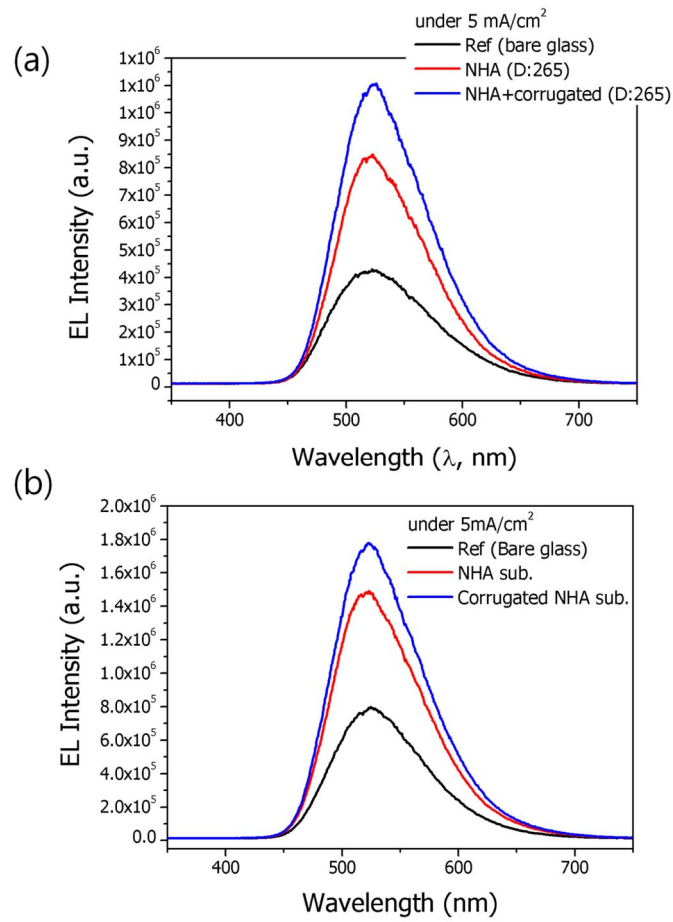


**Figure 6.11.** EL intensity measured for each device as a function of wavelength: (a) the EL intensity of the OLEDs measured using an integrating sphere. (b) The EL intensity was also measured for each device by attaching a 10 mm hemispherical lens to the OLEDs.

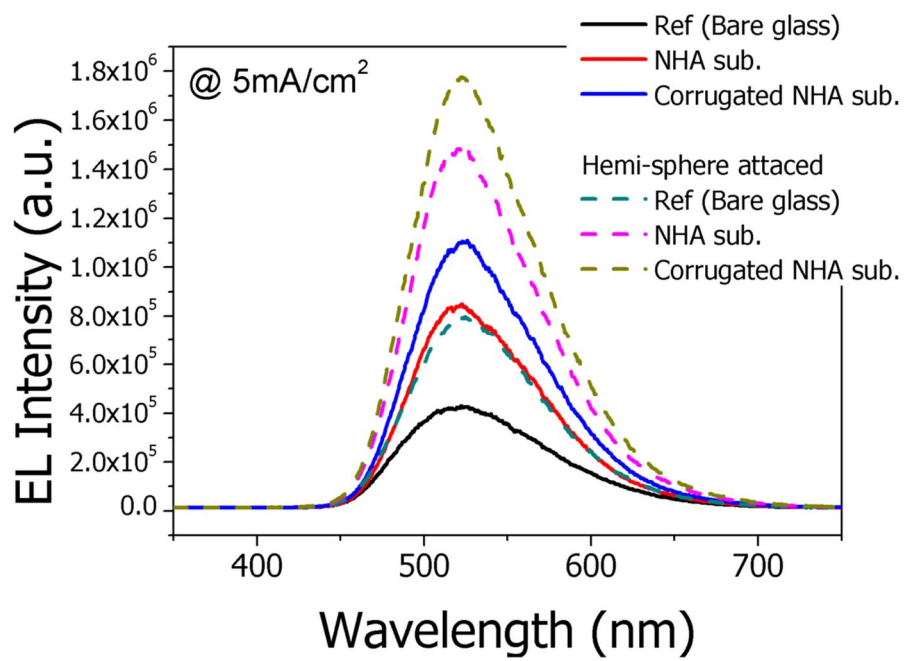


**Figure 6.12.** All of EL intensities measured at  $5 \text{ mA/cm}^2$  are represented in one graph for comparison.

**Table 6.1.** EL enhancement values for different wavelength ranges

	At 523 nm		480-582 nm		414-753 nm		Efficiency <sup>†</sup> (cd/A)
	Max. Peak		FWHM		Full Range		
Ref (Bare)	1.00		1.00		1.00		5.04
NHA	2.01		1.86		1.72		8.67
Corrugated NHA	2.61		2.41		2.22		11.21
HS-Ref (Bare)	1.88	<i>1.00</i>	1.76	<i>1.00</i>	1.66	<i>1.00</i>	8.37
HS-NHA	3.53	<i>1.88</i>	3.26	<i>1.85</i>	3.00	<i>1.81</i>	15.15
HS-Corrugated NHA	4.21	<i>2.24</i>	3.87	<i>2.20</i>	3.56	<i>2.14</i>	17.93

<sup>†</sup> Full Range 기준 Efficiency

## 6.5.2. J-V-L characteristics

**Figure 6.13a** shows the luminance (L) with respect to the current density (J). Light power of NHA-OLEDs improved by a factor of 2.54. The profiles of the reference OLED, NHA-OLED, and MNHA-OLED are represented in **Figure 6.14**. In addition, one of the most important characteristics of electronics is electrical performance. The MNHA used in this study has 30 nm deep CNA and the MNHA embedded OLED is electrically very stable. The J-V curves of the reference OLED, NHA-OLED, and MNHA-OLED are exactly the same on the linear scale as shown in **Figure 6.13b**.

**Figure 6.14** shows the EL intensity depending on the viewing angle under the identical current injection. As expected, the EL intensity of the OLED on the bare glass is decreased as the viewing angle ( $\varphi$ ) is increased by factor of  $\cos \varphi$ , while the vacuum NHA and CNA affect the spectra of the MNHA-OLEDs to change irregularly. All the spectra of the MNHA-OLED over  $40^\circ$  viewing angle are larger than the maximum spectrum of the control device measured in the normal direction.

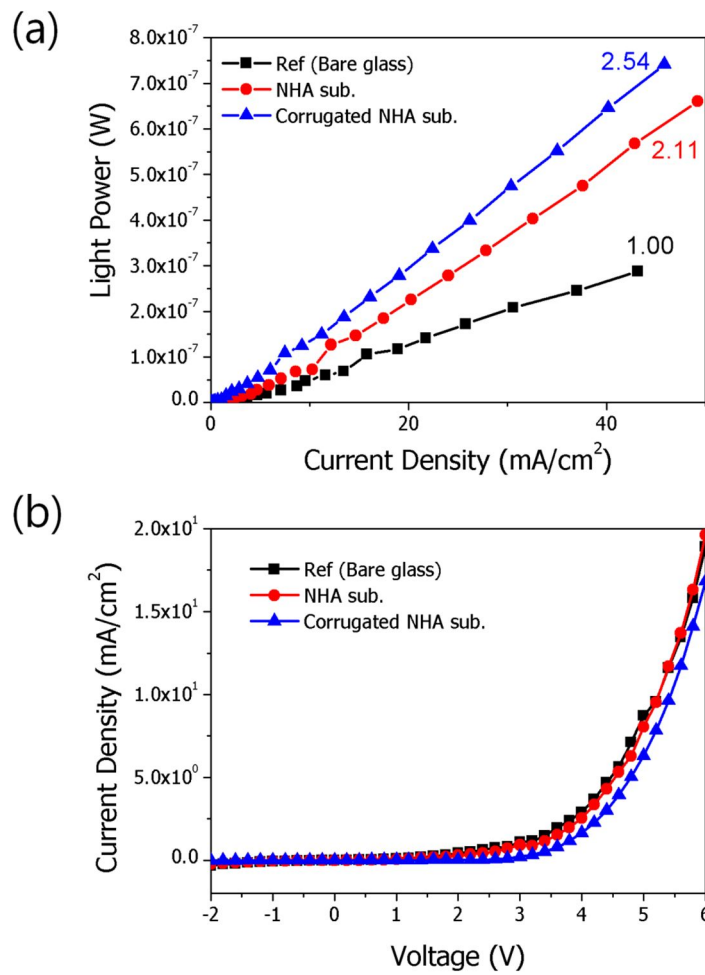


**Figure 6.13.** (a) J-L curves of the OLEDs on the bare glass and on the NHA and MNHA substrates. (b) J-V curves of the OLEDs on the bare glass and on the NHA and MNHA substrates. EL intensity contours of the reference.

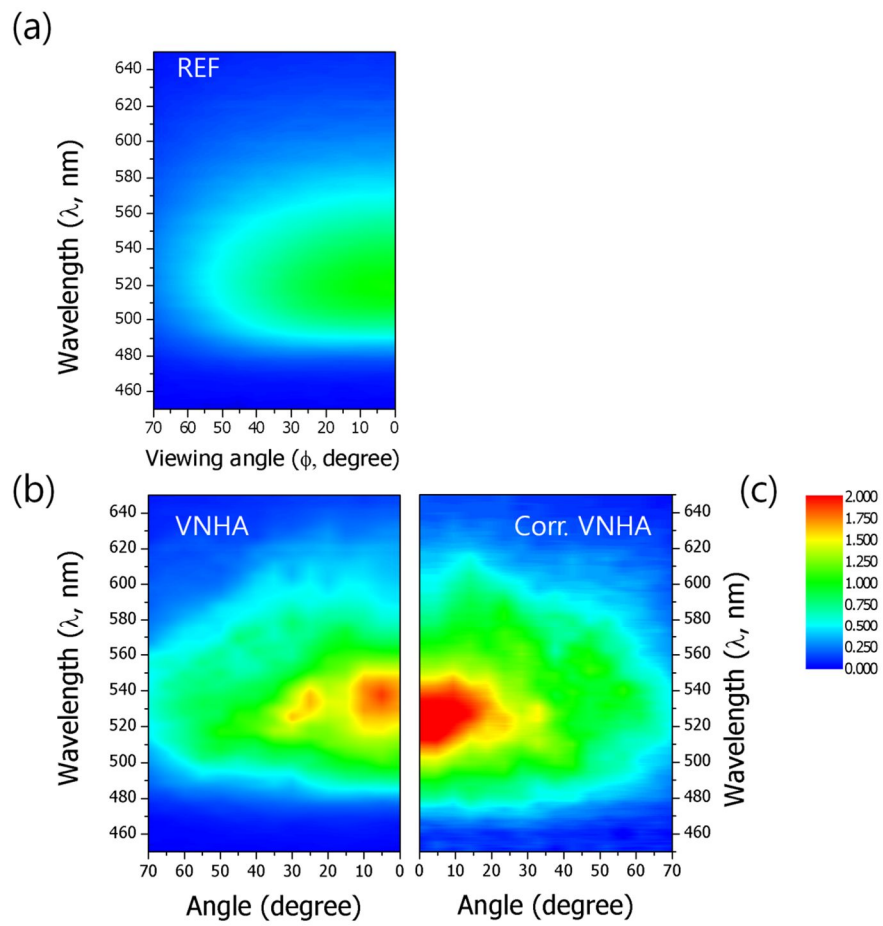


**Figure 6.14.** EL intensity contours of (a) the reference, (b) NHA-OLED and (c) MNHA-OLED depending upon the wavelength and the viewing angle.

## 6.6. Conclusions

In conclusion, the MNHA is proposed to dramatically enhance the light extraction by reducing the losses caused by substrate mode, waveguide mode and surface plasmon polaritons, and by increasing Bragg reflection effect as well as to maintain electrical stability. We fabricated successfully the MNHA embedded OLED. The MNHA was composed of the VNHA with the hole height of 300 nm and the CNA with the depth of 50 nm. The light extraction at full range spectrum (414-753 nm) was improved by 2.22 times with no electrical instability, when the MNHA-OLED was compared with the reference one. Especially, the enhancement factor is the maximum peak (523 nm) is 2.61. Experimental results of the MNHA-OLEDs were consistent with the FDTD simulation results such that the light emitted from the vertical dipoles is considerably improved.

## 6.7. Bibliography

1. S. Möller and S. R. Forrest, *Journal of Applied Physics*, 2002, 91, 3324.
2. J. B. Kim, J. H. Lee, C. K. Moon, S. Y. Kim and J. J. Kim, *Adv Mater*, 2013, 25, 3571-3577.
3. Y. R. Do, Y.-C. Kim, Y.-W. Song and Y.-H. Lee, *Journal of Applied Physics*, 2004, 96, 7629.
4. Y. Sun and S. R. Forrest, *Nature Photonics*, 2008, 2, 483-487.
5. T. Nakamura, H. Fujii, N. Juni and N. Tsutsumi, *Optical Review*, 2006, 13, 104-110.
6. Y.-J. Lee, S.-H. Kim, J. Huh, G.-H. Kim, Y.-H. Lee, S.-H. Cho, Y.-C. Kim and Y. R. Do, *Applied Physics Letters*, 2003, 82, 3779.
7. K. Ishihara, M. Fujita, I. Matsubara, T. Asano, S. Noda, H. Ohata, A. Hirasawa, H. Nakada and N. Shimoji, *Applied Physics Letters*, 2007, 90, 111114.

8. A. O. Altun, S. Jeon, J. Shim, J.-H. Jeong, D.-G. Choi, K.-D. Kim, J.-H. Choi, S.-W. Lee, E.-S. Lee, H.-D. Park, J. R. Youn, J.-J. Kim, Y.-H. Lee and J.-W. Kang, *Organic Electronics*, 2010, 11, 711-716.
9. W. H. Koo, W. Youn, P. Zhu, X.-H. Li, N. Tansu and F. So, *Advanced Functional Materials*, 2012, 22, 3454-3459.
10. M. Fujita, T. Ueno, K. Ishihara, T. Asano, S. Noda, H. Ohata, T. Tsuji, H. Nakada and N. Shimoji, *Applied Physics Letters*, 2004, 85, 5769.
11. W. H. Koo, S. M. Jeong, F. Araoka, K. Ishikawa, S. Nishimura, T. Toyooka and H. Takezoe, *Nature Photonics*, 2010, 4, 222-226.
12. X. L. Zhang, J. Feng, J. F. Song, X. B. Li and H. B. Sun, *Optics Letters*, 2011, 36, 3915-3917.
13. S. Jeon, J. H. Jeong, Y. S. Song, W. -I. Jeong, J. J. Kim and J. R. Youn, *Nanoscale*, 2013, DOI: 10.1039/c1033nr05331h.
14. W. L. Barnes, A. Dereux and T. W. Ebbesen, *Nature*, 2003, 424, 824-830.
15. E. Ozbay, *Science*, 2006, 311, 189-193.
16. S. H. Chang, S. K. Gray and G. C. Schatz, *Optics Express*, 2005, 13, 3150-3165.
17. K. L. Kelly, E. Coronado, L. L. Zhao and G. C. Schatz, *Journal of Physical Chemistry B*, 2003, 107, 668-677.
18. D. M. Schaadt, B. Feng and E. T. Yu, *Applied Physics Letters*, 2005, 86.
19. S. Gresillon, L. Aigouy, A. C. Boccard, J. C. Rivoal, X. Quelin, C. Desmarest, P. Gadenne, V. A. Shubin, A. K. Sarychev and V. M. Shalaev, *Physical Review Letters*, 1999, 82, 4520-4523.
20. S. A. Maier and H. A. Atwater, *Journal of Applied Physics*, 2005, 98.
21. S. A. Maier, *Plasmonics: Fundamentals and Applications*, Springer, USA, 2010.
22. J. Frischeisen, PhD, University of Augsburg, 2011.
23. J. Frischeisen, D. Yokoyama, C. Adachi and W. Brutting, *Applied Physics Letters*, 2010, 96.

# **Part III**

## **Ultrahigh-Efficiency Organic Light Emitting Diodes**

# Chapter 7

## VNHA Embedded OLEDs with Ultimate Efficiency: Phosphorescent Emitter

---

### 7.1. Introduction

OLEDs intrinsically provide high energy efficiency compared with other light sources, and the efficiency has been significantly increased by phosphorescent emitters, charge transport materials, and their vertical arrangement in device designed to realize nearly 100% charge balance. In this case, highly efficient OLED can be materialized with external quantum efficiency (EQE) of over 29% without any extra structures for light extraction.<sup>1, 2</sup> Recently, Park et al. demonstrated OLEDs with very high efficiency and low roll-off, which were produced by using an exciplex-forming co-host as the emitting layer (EML). The OLEDs have an ultrahigh EQE of 29.1%, which implies that the EQE of the OLEDs has nearly reached a theoretical limit.<sup>3</sup> To the best of our knowledge, this value is one of the highest EQEs for bottom-emitting green phosphorescent OLEDs. By adding a photonic structure to such a device, we tried to obtain further enhanced EQE, because 70% of the internal light is still wasted by the substrate, the organic layers, and the transparent electrode even in the case of the highest EQE of 29.1% corresponding to the internal efficiency of 100%. Indeed, although the internal

efficiency reaches almost 100%, OLEDs have a potential to further enhance the efficiency, which can lead to more common usages such as general lighting.

On the other hand, the loss modes can be converted into air by photonic structures inside/outside OLEDs. Thus far, various methods have been proposed to convert the waveguide and glass modes into the radiation mode, e.g., textured surfaces,<sup>4,5</sup> microlens arrays,<sup>6-8</sup> scattering medium,<sup>9</sup> Bragg gratings<sup>10,11</sup> and low-index grids,<sup>12</sup>. As a result, the extraction efficiency has been improved continuously. In general, the loss by glass substrate can be removed by modifying the glass surface, and the waveguide loss can be extracted by inserting a structure between glass and transparent anode.

Here, we demonstrated an extremely high efficiency OLEDs with over 50% of EQE and low roll-off by inserting vacuum nano hole array (VNHA) into phosphorescent OLEDs (PhOLEDs).

The extraction enhancement obtained is quantified in terms of EQE considering the results of the optical modeling analysis for the almost perfect electric characteristics of the device. In general, the OLED efficiencies are given by the following equation:<sup>13,14,15</sup>

$$\eta_{\text{EQE}} = \eta_{\text{int}} \times \eta_{\text{ext}} = \gamma \times \eta_{\text{S/T}} \times q_{\text{eff}} \times \eta_{\text{ext}} \quad (1)$$

The efficiencies of OLED are determined by complicated physics, and all the terms of the equation affect each other<sup>16,17</sup>. If  $\eta_{\text{int}}$  is 100% (that is, the electrical loss should be almost zero), it is useful to estimate the effect of VNHA structure and compare with results of the optical modeling. Therefore, the PhOLEDs with EQE of 29.1% used as a reference is a good platform to validate how much the VNHA structure contributes to the extraction enhancement. In addition, it is verified from comparison between experiment and optical modeling that the VNHA extracts the entire waveguide loss into the air.

## 7.2. Experimental

### 7.2.1. VNHA Fabrication

The VNHA substrate was fabricated by using the novel process called R<sup>2</sup>T. First, an 800nm thick Si<sub>3</sub>N<sub>4</sub> film was deposited on the silicon substrate by means of plasma-enhanced chemical vapor deposition, and then a hexagonal hole array was introduced on the silicon nitride film by using a conventional photolithography, the dry etch process. The nano-hole embedded Si<sub>3</sub>N<sub>4</sub> on the silicon substrate and the glass wafer were bonded using the anodic bonding procedure. The bonded wafers were dipped in a KOH solution to remove the silicon substrate. Consequently, a nanostructure slab was obtained as the OLED substrate that has vacuum (as low index material, actually the lowest index material) holes and Si<sub>3</sub>N<sub>4</sub> (as high index material) matrix alternately. Details on the method for fabricating VNHA structure were described in our previous study<sup>18</sup>

The R<sup>2</sup>T process was developed for confining the nano hole array in the vacuum state. In general, since a top-bottom process fills the generated hole with an upper layer material, it is impossible to obtain an empty state. The periodic nano hole array is inserted in the vacuum state to maximize the refractive index contrast of the PhC slab for a given background high-R.I. material. Thus, we transferred the periodic nano holes onto a glass substrate keeping the vacuum state. In addition, the substrate obtained by the R<sup>2</sup>T process has extremely smooth surface with the roughness of a few nanometer, comparable with that of a polished silicon wafer. Various methods were used in order to fabricate an even surface for the inserted nanostructure, i.e., the plasma-enhanced chemical vapor deposition (PECVD),<sup>19 20</sup> sol-gel spin-coating,<sup>21 22</sup> and doctor blade process.<sup>23</sup> However, those surfaces are found to be wavy and rough beneath the inserted structure. The wavy and rough surface can enhance the efficiency, because the significant light is lost at the organic-metal interface due to the Bragg reflection.<sup>24, 25, 26, 11, 27</sup> However, since the

rough surface necessarily changes both of the electrical and optical characteristics, it is not easy to identify where the origin of enhancement is from. Also, the VNHA surface obtained by the R<sup>2</sup>T process affects only the optical characteristics. Therefore, it is appropriate to figure out the device performance by adopting the results of optical analysis. Moreover, the surface roughness has a strong influence on the electrical characteristics of the device, and is directly related to the device efficiency, which will be dealt with in detail in the following sections.

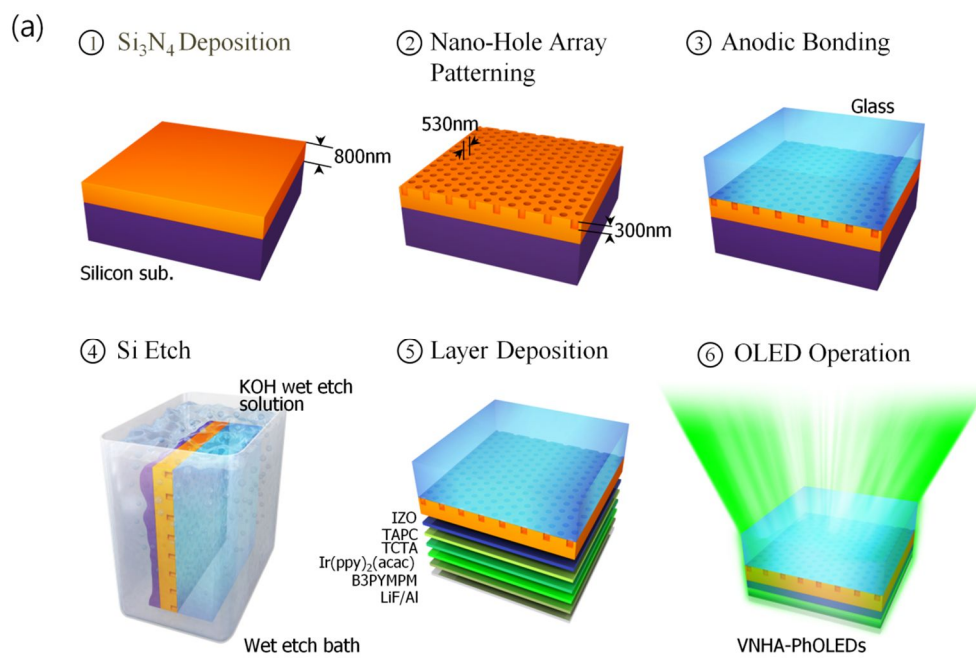


**Figure 7.1.** Schematic diagram for fabrication of the 2D nano-hole array with  $\text{Si}_3\text{N}_4$  as the high-index material and the novel process used in this fabrication is called  $\text{R}^2\text{T}$ .

## 7.2.2. PhOLEDs Fabrication

OLEDs were fabricated on the VNHA and bare substrates. **Figure 7.1** shows a schematic diagram of the R<sup>2</sup>T process, the device structure, and the energy levels of molecules. An IZO anode with a thickness of 70 nm<sup>28</sup> was sputtered on the substrate, and the organic and metallic layers were sequentially deposited by thermal evaporation in the following order: a hole injection layer of 75 nm thick 1,1-bis-(4-bis(4-methyl-phenyl)-amino-phenyl)-cyclohexane (TAPC), a hole transporting layer of 10 nm thick 4,4',4''-tri (N-carbazolyl) tri-phenylamine (TCTA), an emitting layer of bis(2-phenylpyridine)iridium(III)-acetylacetonate (Ir(ppy)<sub>2</sub>(acac)) doped TCTA:B3PYMPM [bis-4,6-(3,5-di-3-pyridylphenyl)-2-methylphyrimidine] and electron transporting layer of 40 nm thick B3PYMPM and a cathode of 1/100 nm thick LiF/Al. For a high efficiency, exciplex-co-host system was used; 4,4',4''-tri (N-carbazolyl) tri-phenylamine (TCTA) and bis-4,6-(3,5-di-3-pyridylphenyl)-2-methylphyrimidine (B3PYMPM) form an exciplex easily in an excited state. This exciplex-forming co-host system enables efficient singlet and triplet energy transfers from the host exciplex to the phosphorescent dopant because the singlet and triplet energies of the exciplex are almost identical.<sup>3</sup>

Park et al. demonstrated an extremely high efficiency green phosphorescent OLEDs using exciplex of the co-host system with the structure aforementioned. The device has a very simple structure consisting of three transport organic materials and one phosphorescent emitting dopant. The TCTA-B3PYMPM exciplex has very efficiently transport charge, which is recombined in the confining zone of the emitting dopant, Ir(ppy)<sub>2</sub>(acac). The electrical loss (including charge balance and exciton-polaron quenching) of the device is negligible. Therefore, the device is very useful to analyze the effect of photonic structure inserted for the extraction enhancement.

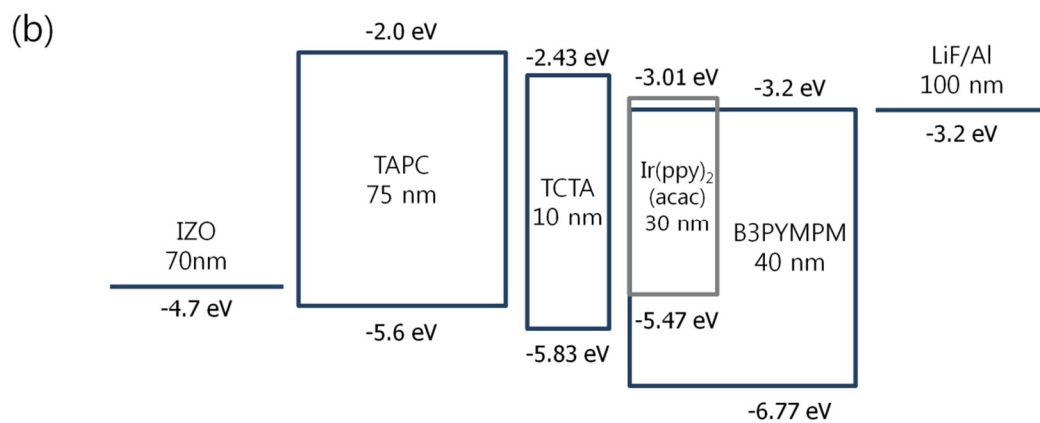


**Figure 7.2.** Device structure and the energy level of the OLEDs.

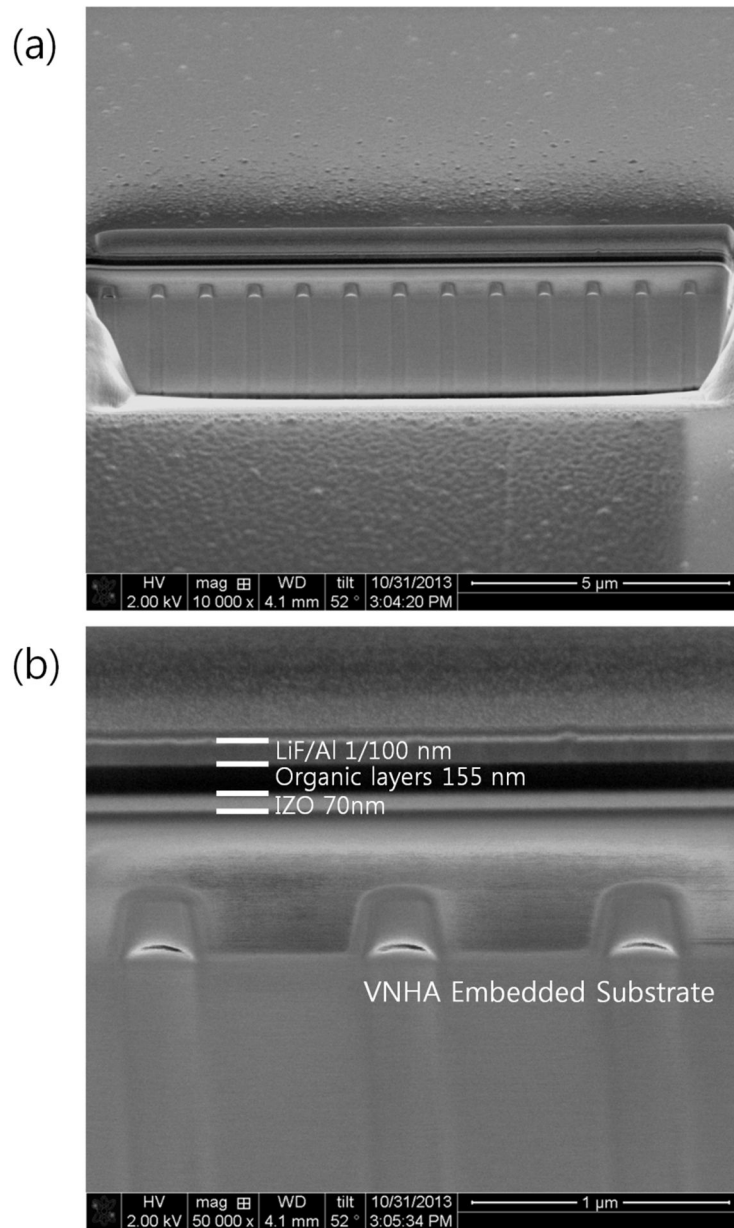


**Figure 7.3.** Focused Ion Beam (FIB) images of the VNHA substrate fabricated by R<sup>2</sup>T process and vertical structure of the VNHA-PhOLEDs.

### 7.2.3. VNHA PhOLEDs

As aforementioned, the electrical loss should be almost zero in order to compare with the results of optical modeling. The perfect device requires the following conditions: (i) the charge balance matched perfectly at the emission layer by selecting optimized device structure such as appropriate arrangement of charge transport materials and their thicknesses, (ii) low roll-off efficiency induced by 100% recombination over a large range of operation current and (iii) very smooth surface for lossless and stable operation of the device. As a reference, the PhOLEDs fabricated in this study already has a high efficiency, 29.1% EQE and the low roll-off indicating a perfect electron and hole balance in the EML layer over the entire operation condition. On the other hand, by transferring VNHA, we obtained the NHA embedded substrate of which top surface has extremely smooth surface comparable with a polished silicon wafer. Therefore we can assume that the electrical loss of VNHA PhOLEDs is negligible, which means that the experimental result can be compared with that of the optical modeling.

### 7.3. Mode Analysis

**Figure 7.4** shows the result of the mode analysis obtained from the classical dipole model.<sup>29, 30</sup> The charge balance was assumed to be unity, and the non-isotropic dipole orientation factor of the emitting dye, Ir(ppy)<sub>2</sub>(acac), was applied to the simulation.<sup>31</sup> The mode analysis was carried out changing the thickness of the electron transporting layer (ETL) which is the most important element of the cavity structure in determining layer thickness. Details of the method for calculating were described in literature.<sup>28, 32</sup> According to the result of the mode analysis, EQE is maximized at an ETL of 40 nm, leading to the air mode of 32.2%, and the others are lost by substrate, waveguide and surface plasmon modes of

23.5%, 12.5% and 24.0%, respectively. By inserting the VNHA structure, the wasted light by the waveguide and substrate modes can be extracted to the air. In what follows, the contribution of the modes will be classified using through empirical and theoretical methods.

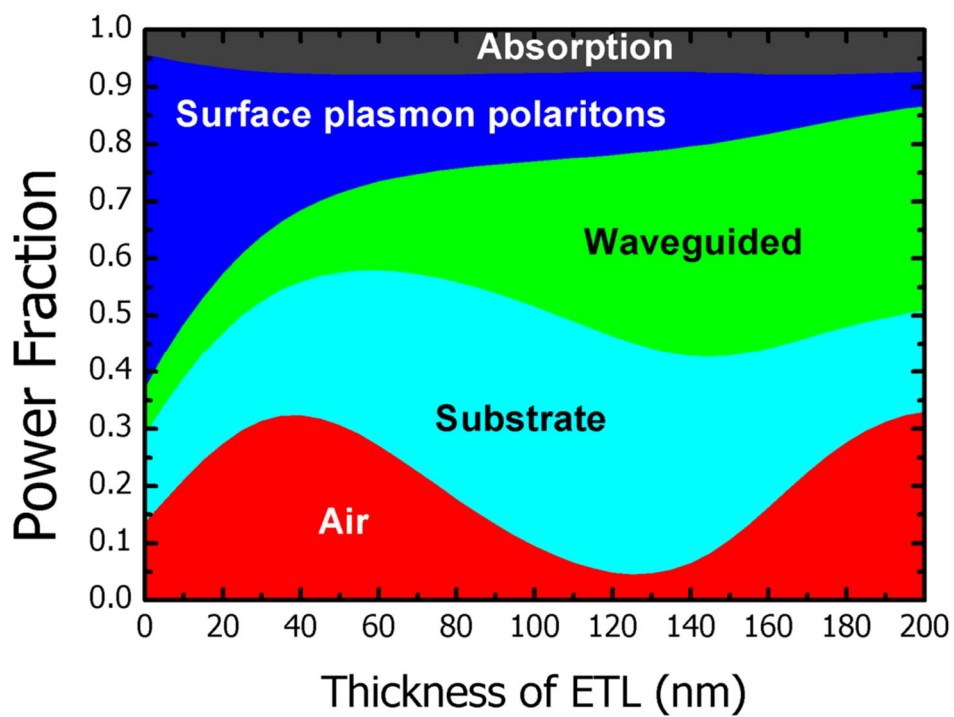


**Figure 7.4.** The mode analysis of exciplex forming co-host phosphorescent OLEDs. The power coupling ratio simulated using the classical dipole model for the bottom emission.

## 7.4. Photoluminescence Performance

To confirm the optical enhancement of the vacuum nanoarray, the angular dependence of the photoluminescence (PL) is measured as shown in **Figure 7.5**. By observing the polarized angular PL, the influences of the embedded structure on the horizontal ( $d_x$ ,  $d_y$ ) and vertical ( $d_z$ ) dipoles can be identified. The in-plane and out of plane PL are measured at every 30 degrees, and both of them should be increased to verify the enhancement effect of the inserted nanostructure. Otherwise, the enhancement of in-plane intensity (the enhancement in only one direction) is likely to indicate only the change of light path, not increment of the light extraction in the air.

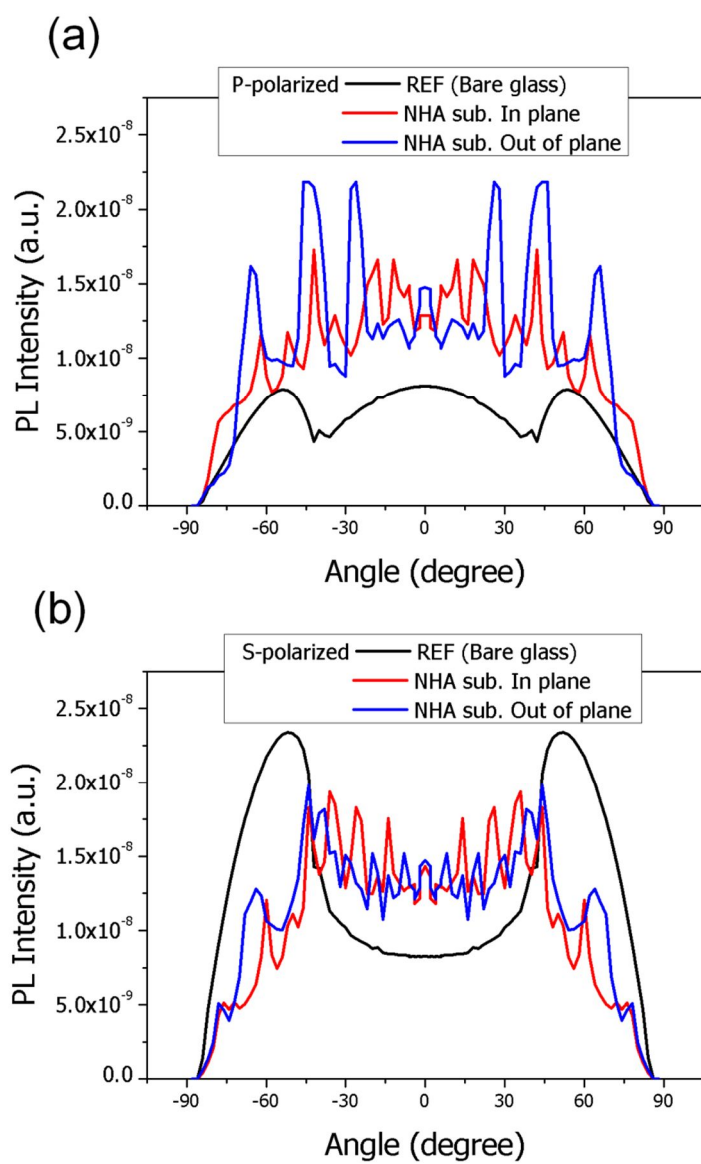
### 7.4.1. Polarized angular photoluminescence

Figure 7.5 shows the p- and s-polarized PL intensities depending on the viewing angle. The schematic diagram of the PL intensity measurement and details of the method are illustrated in the supporting information. The  $dy$ -dipoles emit only s-polarized light, whereas the  $dx$ - and  $dz$ -dipoles are responsible for the p-polarized emission.<sup>33</sup> Hence, the angle-dependent PL spectrum was measured for the analysis of the exact fraction of horizontal and vertical dipoles based on that of an isotropic molecule. It has been reported that the phosphorescent emitter, Ir(ppy)<sub>2</sub>(acac), has a horizontally preferred non-isotropic dipole orientation with a horizontal-vertical dipole ratio of 0.77:0.23 as compared with 0.67:0.33 in the isotropic random case.<sup>31</sup> Moreover, the analysis gives the enhancement by only waveguide mode resulting from the spherical interface between glass and air. This is attributed just to the optical effect of the VNHA structure rather than electrical effects, such as charge balance and surface plasmon polariton. The PL intensities of s- and p-polarized lights are significantly improved at the critical angle range of glass ( $n=1.47$ )/air

( $n=1.0$ ),  $\pm 41.8^\circ$ . Therefore, the proposed VNHA structure provides enhancement in the emission extraction induced by both the vertical and horizontal dipoles.

#### **7.4.2. Comparison of angular PL considering dipole orientations**

On the other hand, in our previous report the p- and s-polarized PL of the fluorescent isotropic dipole emitter, Alq<sub>3</sub>, were measured as well.<sup>18</sup> Although those two emitters are totally different in terms of molecule structures, PL efficiencies and emission types (fluorescent and phosphorescent), peaks are obtained at the same angle. This means that optical characteristics of the given photonic structure are determined by the wavelength of emitted light. However, the enhanced amounts are slightly different. Although the band gaps of Alq<sub>3</sub> and Ir(ppy)<sub>2</sub>(acac) are the same and their spectra are similar each other, Ir(ppy)<sub>2</sub>(acac) has horizontally preferred dipole. In this result, the enhancement of p-polarized intensity responsible for  $dz$  decreases as the horizontal dipoles increase.



**Figure 7.5.** PL intensity measured as a function of the viewing angle for (a) the p-polarized and (b) the s-polarized light emission with the wavelength of 520 nm.

## 7.5. Electroluminescence Performance

### 7.5.1. EQE and power efficiency of VNHA-PhOLEDs

**Figure 7.6** shows the EL performance of the VNHA inserted OLEDs. The phosphorescent OLED used as a reference has a very high efficiency of 29.1% corresponding to the internal quantum efficiency (IQE) of 100%. This efficiency is in a good agreement with the mode analysis result calculated without consideration of electrical factors. The extremely low roll-off indicates that the charge-balance factor must be close to unity over the broad range of current density and that electrical loss is negligible in this case. The reference OLEDs are ideal for a platform to analyze the extraction factor of the VNHA structure, and very useful to understand the result of the mode analysis. Moreover, as aforementioned the VNHA obtained from the R<sup>2</sup>T process possesses very smooth surface with a low roughness level, thereby leading to the negligible electrical loss. The enhancement of EL is estimated using an intensified CCD as shown in Figures 7.6(c) and 7.6(d). The relative spectra were measured using an integrating sphere to detect the light radiated in all directions under the same current, 1mA/cm<sup>2</sup> at which the EQE of the reference device became the maximum. The enhancement values and corresponding EQEs are summarized in Table 1. The spectra of hemi-sphere attached to each device are measured in order to identify the enhancement only by the waveguide mode, but not the glass mode. The relative spectrum of VNHA embedded green PhOLEDs was improved by 1.74 times, and the resulting EQE is 50.7%. This EQE is slightly larger than that of the hemi-sphere lens attaching reference OLEDs (HS-OLEDs), and which means that the VNHA OLEDs are brighter than the HS-OLEDs which have a maximum value by extracting all the trapped light in glass substrate. The EQE of VNHA OLEDs is obtained through the calibration using the relative spectra measured under the various current densities as shown in Figure 7.6(d).

### **7.5.2. Hemi-sphere attaching VNHA-PhOLEDs**

On the other hand, we can analyze the extraction of waveguide mode by attaching a hemi-sphere, which enables total internal reflection to be excluded. A 10mm diameter hemi-sphere is attached with index matching oil. As marked in table 1, the hemi-sphere attached VNHA OLEDs show about 17.17 % enhancement compared with the HS-reference, which is larger than the light loss by the waveguide mode. Therefore, the VNHA allows the entire waveguide mode to be extracted without a significant loss.

Recently, we reported the VNHA OLEDs employing a fluorescent molecule, Alq<sub>3</sub> as an emitter. The VNHA OLED shows larger enhancement than the case of using phosphorescent emitter by a factor of 1.89, of which value is a little larger than that of Ir(ppy)<sub>2</sub>(acac). Similar to the PL, the orientation of emitter molecule influences the enhancement factor. Since the perpendicular dipole to the plane is directly emitted into the air, the enhancement factor obtained by the inserted structure is decreased with an increase with the portion of horizontal dipole.

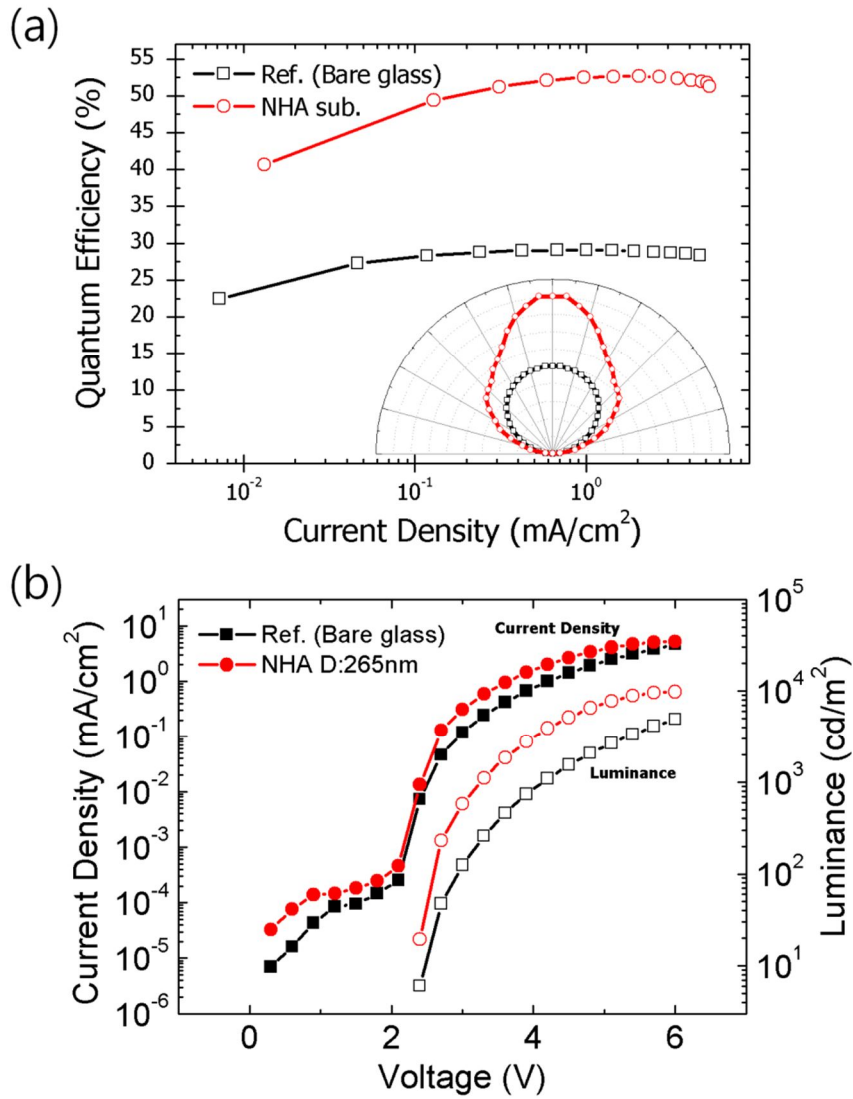


**Figure 7.6.** (a) External quantum efficiencies (Inset: angular dependent emission) and (b) power efficiencies of reference and VNHA PhOLEDs.

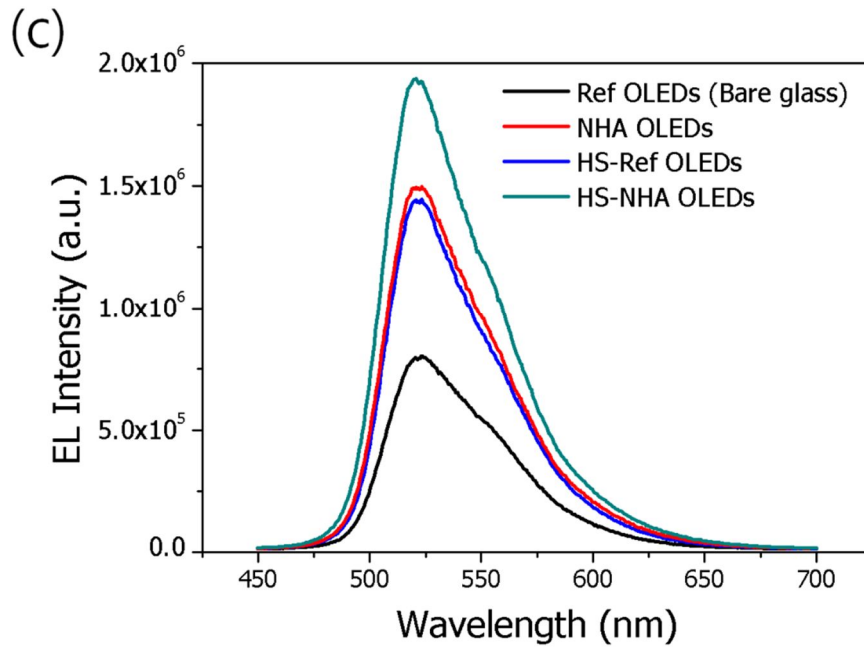


**Figure 7.6.** (c) EL intensity measured for each device as a function of wavelength. The EL intensity of the VNHA-PhOLED (red line) and the control (black line) device measured using an integrating sphere. The EL intensity was also measured for each device by attaching a 10 mm hemisphere lens to the VNHA-PhOLED (blue line) and the control device (green line).

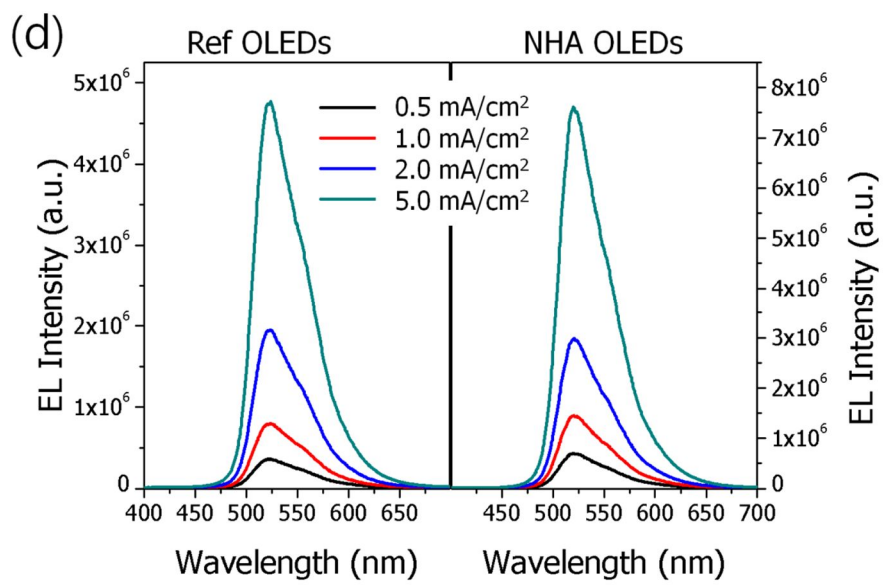


**Figure 7.6.** (d) EL intensity under the different current densities of 0.5, 1.0, 2.0 and 5.0 mA/cm<sup>2</sup>.

**Table 7.1.** EL enhancement values and EQEs for different wavelength ranges

	At 520 nm Max. peak	505-565 nm FWHM	280-700 nm Visible Range	EQE (%)
Reference	1.0	1.0	1.0	29.11
VNHA-OLEDs	1.86	1.80	1.74	50.65
HS-Reference	1.81	1.74	1.72	50.07
HS-VNHA-OLEDs	2.45	2.35	2.31	67.24

## 7.6. Conclusions

We obtained an extremely high efficiency OLEDs with over 50% of EQE and low roll-off by inserting vacuum nano hole array (VNHA) into phosphorescent OLEDs (PhOLEDs). The R<sup>2</sup>T process was developed for confining the nano hole array in the vacuum state. The periodic nano hole array is inserted in the vacuum state to maximize the refractive index contrast of the PhC slab for a given background high-R.I. material. This EQE is the highest EQEs for bottom-emitting OLEDs. The performance of the VNHA OLEDs was compared with the results of the optical modeling analysis, and it is verified that the VNHA extracts the entire waveguide loss into the air.

## 7.7. Bibliography

1. D. Tanaka, H. Sasabe, Y.-J. Li, S.-J. Su, T. Takeda and J. Kido, *Japanese Journal of Applied Physics*, 2007, **46**, L10-L12.
2. M. G. Helander, Z. B. Wang, J. Qiu, M. T. Greiner, D. P. Puzzo, Z. W. Liu and Z. H. Lu, *Science*, 2011, **332**, 944-947.
3. Y.-S. Park, S. Lee, K.-H. Kim, S.-Y. Kim, J.-H. Lee and J.-J. Kim, *Advanced Functional Materials*, 2013, **23**, 4914-4920.
4. J. Zhou, N. Ai, L. Wang, H. Zheng, C. Luo, Z. Jiang, S. Yu, Y. Cao and J. Wang, *Org Electron*, 2011, **12**, 648-653.
5. Y. H. Cheng, J. L. Wu, C. H. Cheng, K. C. Syao and M. C. M. Lee, *Appl Phys Lett*, 2007, **90**, 091102.
6. J. Lim, S. S. Oh, D. Y. Kim, S. H. Cho, I. T. Kim, S. H. Han, H. Takezoe, E. H. Choi, G. S. Cho, Y. H. Seo, S. O. Kang and B. Park, *Optics Express*, 2006, **14**, 6564-6571.
7. Y. Sun and S. R. Forrest, *J Appl Phys*, 2006, **100**, 073106.

8. J.-B. Kim, J.-H. Lee, C.-K. Moon, S.-Y. Kim and J.-J. Kim, *Advanced Materials*, 2013, **25**, 3571-3577.
9. R. Bathelt, D. Buchhauser, C. Gärditz, R. Paetzold and P. Wellmann, *Org Electron*, 2007, **8**, 293-299.
10. J. H. Jang, M. C. Oh, T. H. Yoon and J. C. Kim, *Appl Phys Lett*, 2010, **97**, 123302.
11. A. O. Altun, S. Jeon, J. Shim, J.-H. Jeong, D.-G. Choi, K.-D. Kim, J.-H. Choi, S.-W. Lee, E.-S. Lee, H.-D. Park, J. R. Youn, J.-J. Kim, Y.-H. Lee and J.-W. Kang, *Org Electron*, 2010, **11**, 711-716.
12. Y. Sun and S. R. Forrest, *Nature Photonics*, 2008, **2**, 483-487.
13. T. Tsutsui, E. Aminaka, C. P. Lin and D. U. Kim, *Philosophical Transactions of the Royal Society a-Mathematical Physical and Engineering Sciences*, 1997, **355**, 801-813.
14. W. Brütting, J. Frischeisen, T. D. Schmidt, B. J. Scholz and C. Mayr, *physica status solidi (a)*, 2013, **210**, 44-65.
15. M. Furno, R. Meerheim, S. Hofmann, B. Lussem and K. Leo, *Physical Review B*, 2012, **85**, 115205.
16. E. M. Purcell, *Physical Review*, 1946, **69**, 681-681.
17. S. H. Fan, P. R. Villeneuve, J. D. Joannopoulos and E. F. Schubert, *Physical Review Letters*, 1997, **78**, 3294-3297.
18. S. Jeon, J. H. Jeong, Y. S. Song, W. -I. Jeong, J. J. Kim and J. R. Youn, *Nanoscale*, 2013, DOI: 10.1039/c1033nr05331h.
19. Y.-J. Lee, S.-H. Kim, J. Huh, G.-H. Kim, Y.-H. Lee, S.-H. Cho, Y.-C. Kim and Y. R. Do, *Appl Phys Lett*, 2003, **82**, 3779.
20. S. Jeon, J.-W. Kang, H.-D. Park, J.-J. Kim, J. R. Youn, J. Shim, J.-h. Jeong, D.-G. Choi, K.-D. Kim, A. O. Altun, S.-H. Kim and Y.-H. Lee, *Appl Phys Lett*, 2008, **92**, 223307.
21. H. H. Cho, B. Park, H. J. Kim, J. Shim, S. Jeon, J. H. Jeong and J. J. Kim, *Current Applied Physics*, 2010, **10**, E139-E142.

22. Y.-C. Kim, S.-H. Cho, Y.-W. Song, Y.-J. Lee, Y.-H. Lee and Y. R. Do, *Appl Phys Lett*, 2006, **89**, 173502.
23. W. J. Hyun, H. K. Lee, S. S. Oh, O. Hess, C. G. Choi, S. H. Im and O. O. Park, *Advanced Materials*, 2011, **23**, 1846-1850.
24. W. H. Koo, S. M. Jeong, F. Araoka, K. Ishikawa, S. Nishimura, T. Toyooka and H. Takezoe, *Nature Photonics*, 2010, **4**, 222-226.
25. C. J. Yates, I. D. W. Samuel, P. L. Burn, S. Wedge and W. L. Barnes, *Appl Phys Lett*, 2006, **88**, 161105.
26. P. A. Hobson, S. Wedge, J. A. E. Wasey, I. Sage and W. L. Barnes, *Advanced Materials*, 2002, **14**, 1393-1396.
27. X. L. Zhang, J. Feng, J. F. Song, X. B. Li and H. B. Sun, *Optics Letters*, 2011, **36**, 3915-3917.
28. S. Y. Kim and J. J. Kim, *Org Electron*, 2010, **11**, 1010-1015.
29. R. R. Chance, A. Prock and R. Silbey, in *Advances in Chemical Physics*, John Wiley & Sons, Inc., 2007, pp. 1-65.
30. J. A. E. Wasey and W. L. Barnes, *Journal of Modern Optics*, 2000, **47**, 725-741.
31. P. Liehm, C. Murawski, M. Furno, B. Lussem, K. Leo and M. C. Gather, *Appl Phys Lett*, 2012, **101**, 253304.
32. W. I. Jeong, S. Y. Kim, J. J. Kim and J. W. Kang, *Chemical Physics*, 2009, **355**, 25-30.
33. J. Frischeisen, D. Yokoyama, C. Adachi and W. Brutting, *Appl Phys Lett*, 2010, **96**, 073302.

## Appendix A. VNHA Substrate Fabrication and Characterization

In order to maximize the refractive index contrast of PhCs for a given background material, we propose that the low vacuum nanohole array be transferred to the glass substrate in the PhC slab using the robust reverse transfer ( $R^2T$ ) process. **Figure A.1a** and **A.1b** are SEM images of the NHA substrate and the OLEDs integrated on the NHA substrate. The subsequent layers were evenly deposited on the NHA substrate. On the other hand, the PNA substrate, which was planarized through plasma enhanced chemical vapor deposition (PECVD) on the polymer array, has a wavy surface and peak points. As a result, the above layers also have wavy and peaky surfaces along the surface of the substrate.

The robust reverse-transfer method was based on the 8-inch wafer process in this study, and then OLEDs devices were fabricated on the substrate diced into  $25 \times 25 \text{ mm}^2$ . Furthermore, the  $R^2T$  bonding is almost a defect-free process over the entire region of an 8-inch wafer as shown in **Figure A.2**. Figure A.2a shows the wafer after anodic bonding process between the nano-holes patterned  $\text{Si}_3\text{N}_4$  on silicon wafer and glass wafer, and then dipping KOH solution the bonded wafer, the final substrate is obtained by removing silicon wafer as shown in figure A.2b. In order to increase the number of samples, the wafer is fully patterned by step and repeat photolithography as shown in figure A.2c.

The AFM images of the NHA substrates are shown in **Figures A.3a** and **A.3b**. The  $R_a$  values were on the order of sub-nano scale, which is the same level as that of the polished Si wafer roughness, as represented in the table below. Meanwhile, the  $R_a$  values of the PNA substrate are tens of times larger than those of the NHA substrates, as shown in **Figure A.4**. Especially,  $R_{pv}$  has a critical effect on the performance of electrical devices, because electric fields are focused on a peaky point, and, as such, a concentrated electric field can permanently damage organic materials. By proposing this  $R^2T$  process, we can achieve an NHA substrate that not only has a sub-nano level of roughness to its surface but also maximizes the RI contrast of the PhC structure.

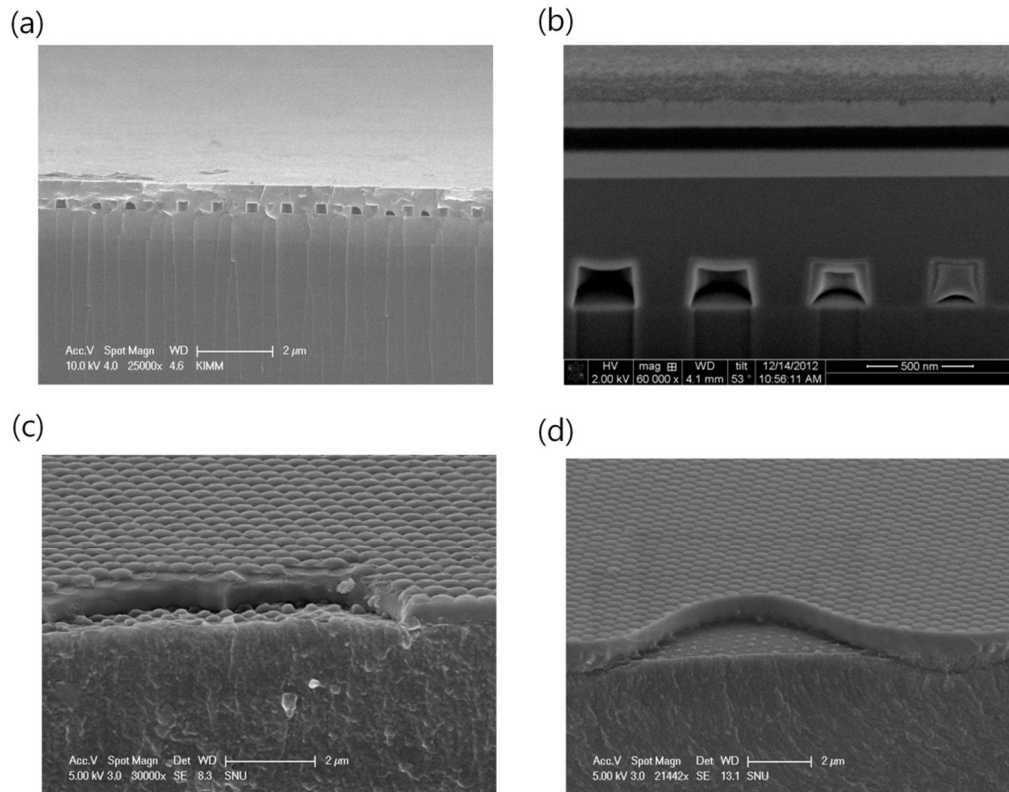


**Figure A. 1.** SEM images of (a) the nano-hole array substrate. The trapped low vacuum state was periodically arranged by R<sup>2</sup>T process. (b) OLEDs integrated on the NHA substrate. (c) and (d) The Si<sub>3</sub>N<sub>4</sub>/polymer nanoarray (PNA) substrate. The 500 nm (c) and 800 nm (d) planarized dielectric material (Si<sub>3</sub>N<sub>4</sub>) deposited using PECVD.

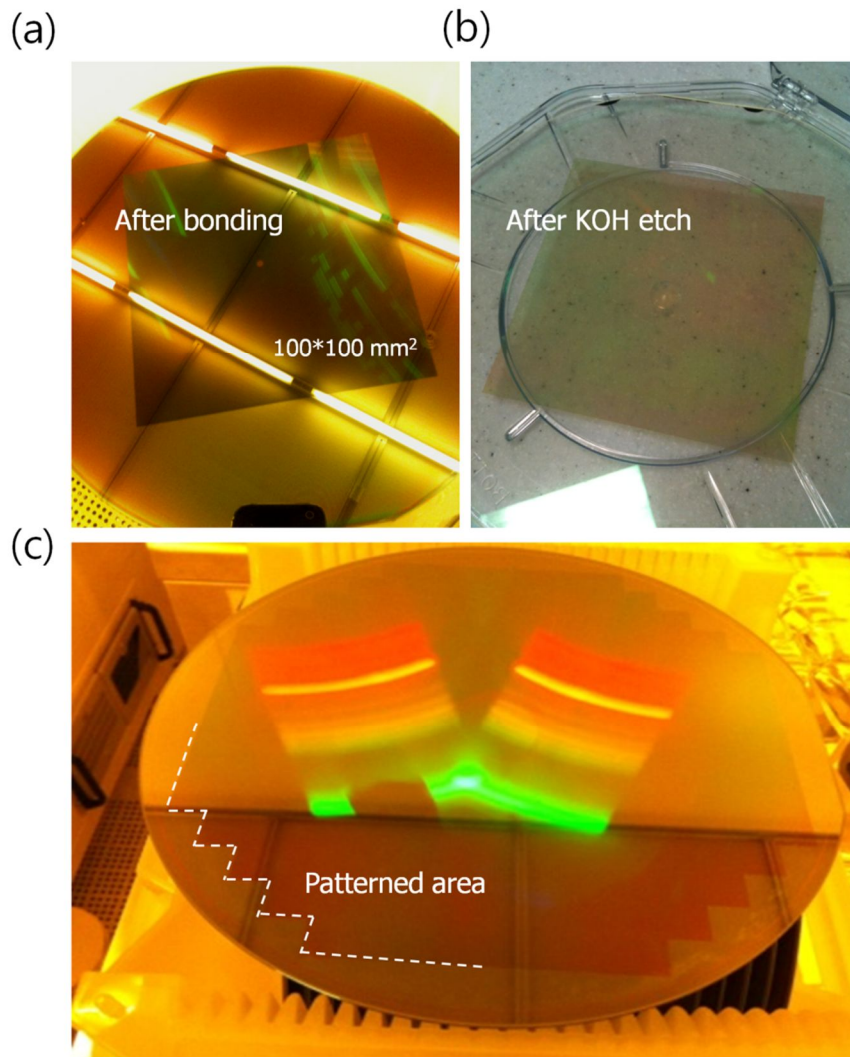


**Figure A. 2.** The photographs (a) after anodic bonding, and (b) after removing silicon by dipping KOH solution. The periodic hole is defined over 100\*100 mm<sup>2</sup> on 8-inch silicon wafer. and (c) Fully patterned wafer in order to increase the number of samples.

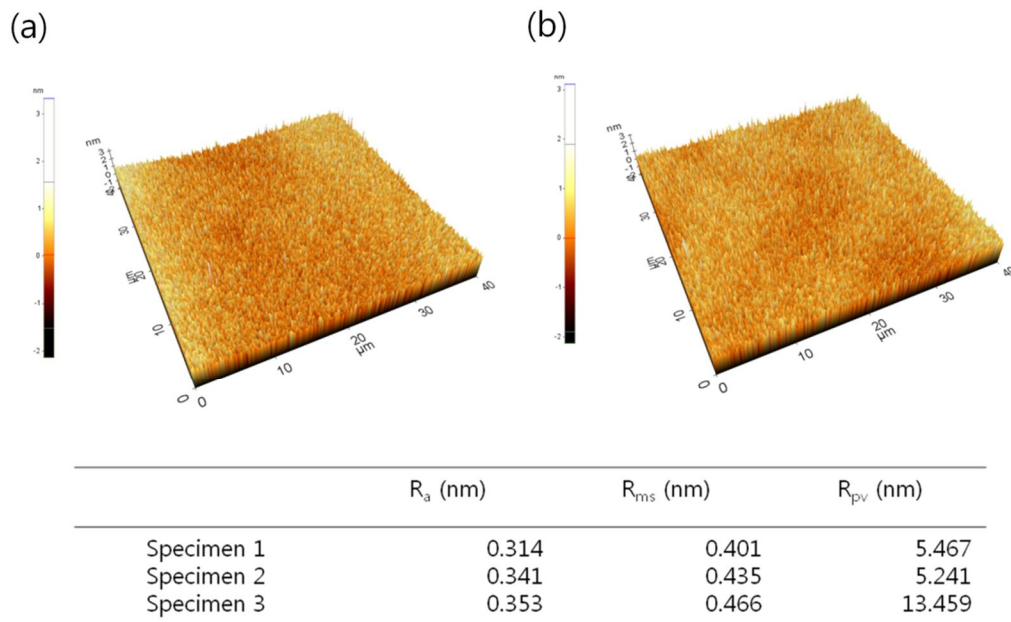
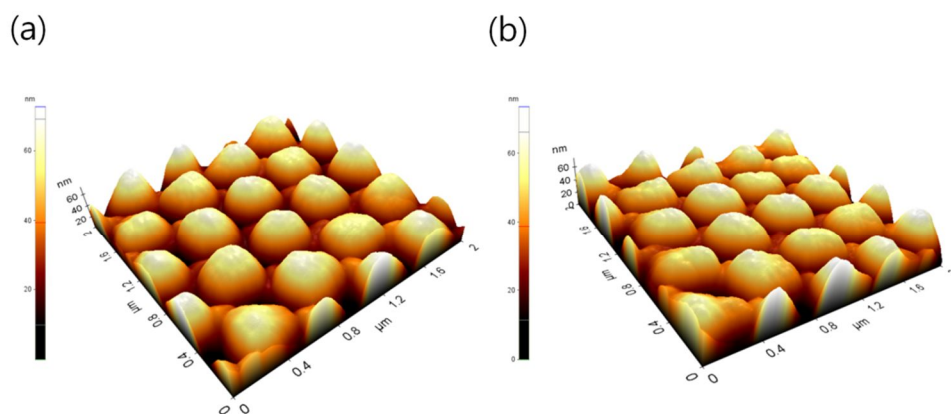


**Figure A. 3.** (a) and (b) AFM images of the NHA substrates. The roughness data of several NHA substrates are summarized in the table below.



The PNA substrate	$R_a$ (nm)	$R_{ms}$ (nm)	$R_{pv}$ (nm)
Specimen 1	13.398	15.801	57.434
Specimen 2	11.211	13.451	47.381
Specimen 3	12.590	15.138	55.217

Electrode on the PNA substrate	$R_a$ (nm)	$R_{ms}$ (nm)	$R_{pv}$ (nm)
Specimen 1	13.153	15.210	51.057
Specimen 2	10.838	13.492	54.542
Specimen 3	9.476	11.463	43.310

**Figure A. 4.** AFM images of (a) the PNA substrates and (b) an electrode surface after sputtering 150 nm-thick ITO layers on the PNA substrates. The roughness data for the PNA substrates and for the electrode on the PNA substrates are summarized in the table below.

## Appendix B. FDTD Simulation Details

The simulation is performed for a structure identical to the experimental structure. The domain size of the numerical calculation was  $8000 \times 8000 \times 1950 \text{ nm}^3$  which included the actual device: the anode, organic materials, cathode, and corresponding nanostructure layer. Point dipole sources were placed inside of the organic layer at the Alq<sub>3</sub>/NPB interface and located at the center of the plane. The wavelength and FWHM (full width at half maximum) were set to be the same as those of PL, 520 nm and 50 nm, respectively. The simulated Poynting energy was detected by the monitor inside the glass and the distance from the dipole source was fixed at the same value. The energy passing through the monitor was obtained by integrating the simulated Poynting energy over time, area, and frequency.

To observe the dependence of the dipole location on the Poynting energy, we estimated the extracting energies that propagated from each dipole at the 16 different positions in the unit cell, and around the unit cell's circumference, as shown in **Figure B.1a**. **Figure B.1b** shows the time integrated Poynting energy according to the polarization of the transverse magnetic (TM) and transverse electric (TE) dipoles at each point: the extracting Poynting energy is the same regardless of the dipole locations. Therefore, we can reduce the calculation time, since it is possible that only one dipole will be sufficient to describe the emission source.

On the other hand, the lattice constant of PhC varies from 460 to 620 nm according to visible wavelength range because the extraction efficiency becomes largest when the lattice constant is close to the vacuum wavelength, as discussed in the main text. FDTD simulations were performed by varying dipole angles for various designs of PhC structures and colors of light sources according to each combination of the three different lattice constants and the three different wavelengths. As shown in **Figure B.2**, the integrated Poynting energies were almost identical regardless of the lattice constant or the wavelength of the dipole

sources. As mentioned in the main text, it is confirmed that the crucial factor is the RI difference between  $n_{\text{low}}$  and  $n_{\text{high}}$ , rather than the lattice constant of the PhCs.

Meanwhile, FDTD simulation was carried out by varying the hole depth of the nanoarray. The Poynting energy as a function of hole depth was saturated until the hole depth reached 300 nm, so the depth was set at 300 nm.

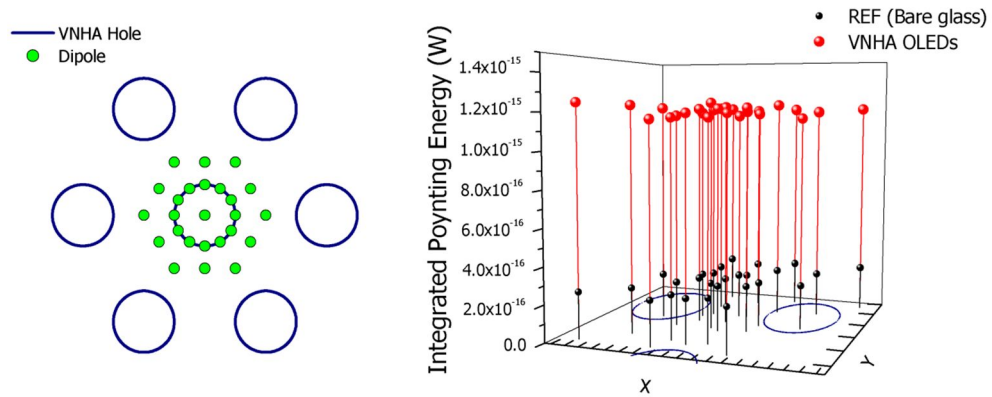


**Figure B. 1.** A unit cell of a hexagonal nanostructure. The integrated Poynting energy was estimated according to the position of dipoles.

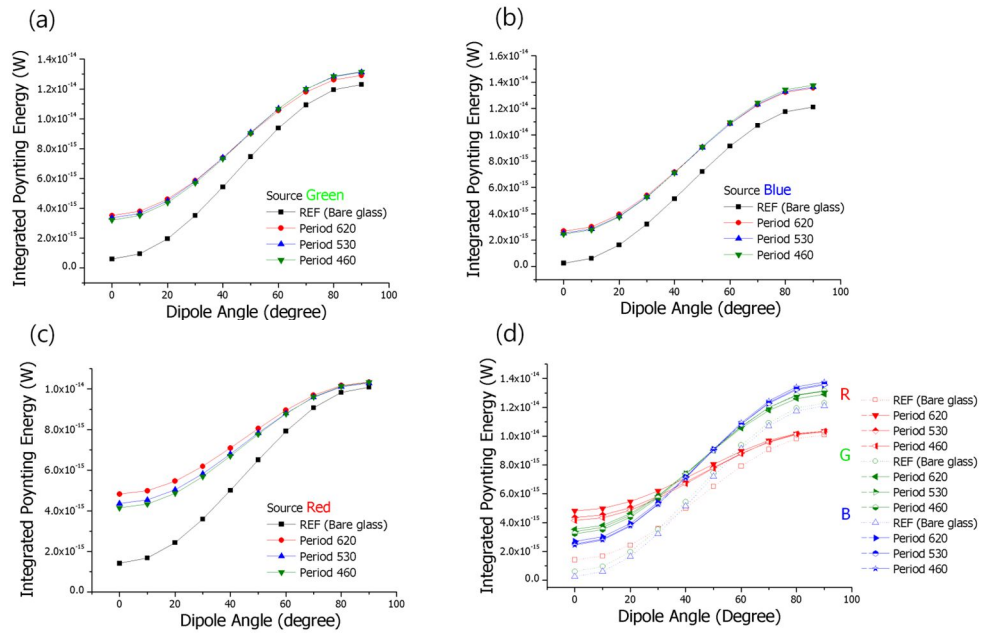


**Figure B. 2.** FDTD analysis according to the lattice constants for green (a), blue (b), and red (c); all of the results are shown in one graph (d).

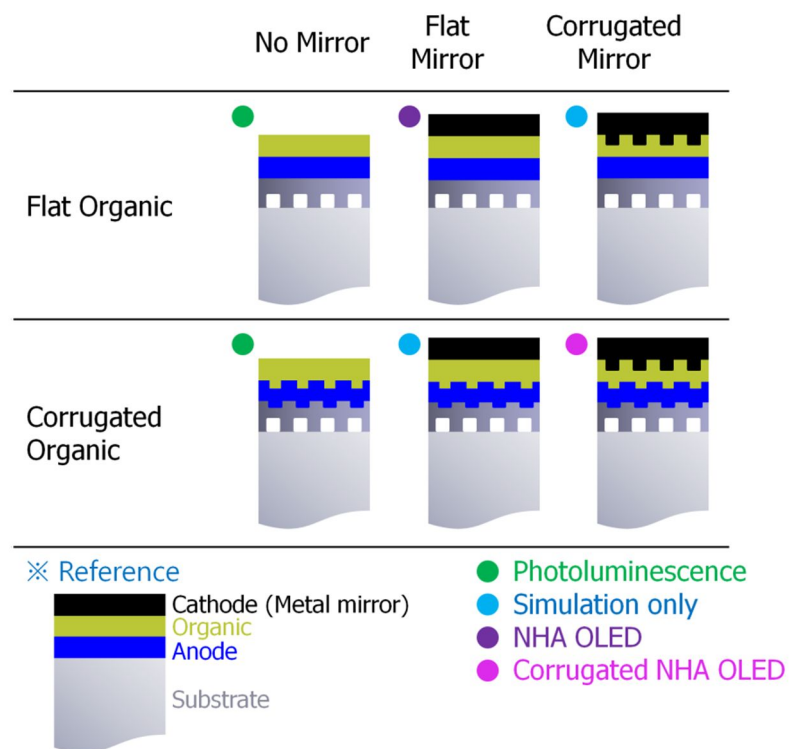


**Table B. 1.** Classification for FDTD analysis. The combination of flat /corrugated organic layer and no/flat/corrugated metal mirrors.

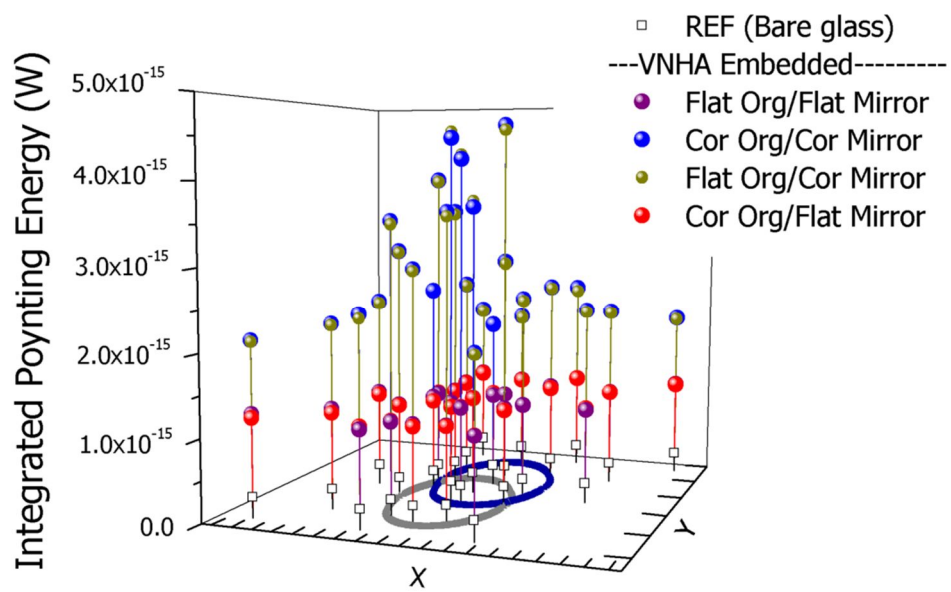


**Figure B. 3.** FDTD results of the combination of flat /corrugated organic layer and flat/corrugated metal mirrors.

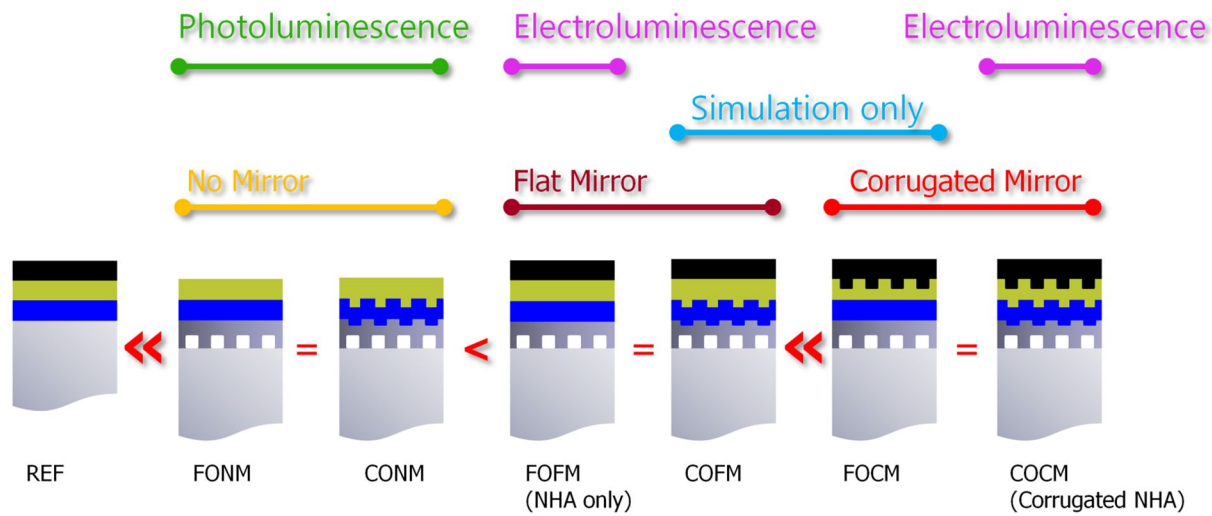


**Figure B. 4.** Summary of the FDTD results .

## Appendix C. Angular PL Characteristics

### C. 1. Angular PL specimen fabrication

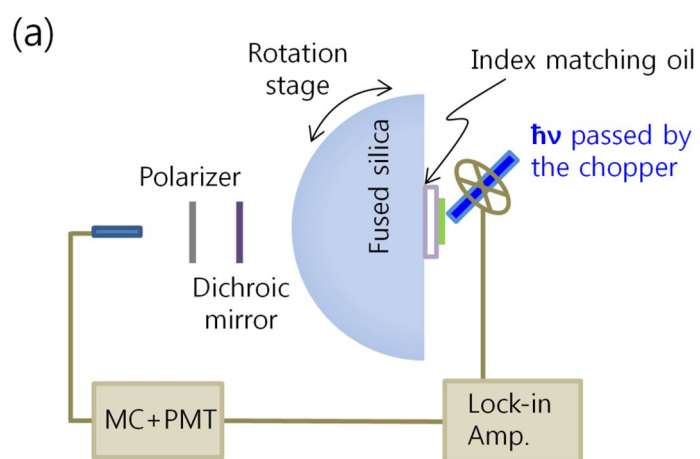
To obtain Angular PL samples, 50nm thick 1% C545T doped Alq<sub>3</sub> was deposited on the NHA and bare substrates (fused silica) by thermal evaporation. The dopant, 1% C545T, was co-evaporated because the PL intensity of Alq<sub>3</sub>, induced by 325 laser, was too weak to catch its signal and the dopant just made the PL intensity strong but did not change the dipole orientation.

### C. 2. Angular PL measurement set-up

**Figure C.1** shows the angle dependent PL measurement set-up.<sup>1</sup> To measure the angle dependence of PL, the PL specimens were scanned through the  $\Gamma$ M direction corresponding to the constructive plane as the viewing angle was varied with the interval of one degree. A 100 mm diameter fused silica half-cylinder was attached to the PL specimen using index matching oil. The PL emission through the half-cylinder was measured using the photo-detector linked with a monochromator, chopper, and lock-in amplifier. Those signals were amplified using a photo multiplier tube (PMT). The measurement set-up is illustrated in the Figure C.1 of the supporting information. The linear polarized continuous wave laser diode ( $\lambda=325$  nm) is used as an optical exciting source. The optical source is injected through the sample tilted at 45° with respect to the substrate surface in order to excite the entire dipoles equally regardless of dipole orientation.

By using index matching oil, the PL sample is attached on a fused silica half cylinder with a diameter of 100 mm. The emission light can directly escape

and, due to the spherical surface, does not experience TIR at the interface between the glass and air, so we can easily compare these results to those of the PL experiment and to the FDTD simulation results. A 325 nm wavelength laser source was injected at an angle of 45-degrees to the PL sample surface in order to excite all the dipoles regardless of their orientation. In addition, the source parts of the angle dependent PL measurement set-up were put on a rotation stage, and so the intensities can be measured as a function of the viewing angle. The light is transmitted by a linear polarizer before reaching the detector. The s- and p-polarizers separate the light induced from the  $d_y$  dipoles and the  $d_x/d_z$  dipoles, respectively.



(b)

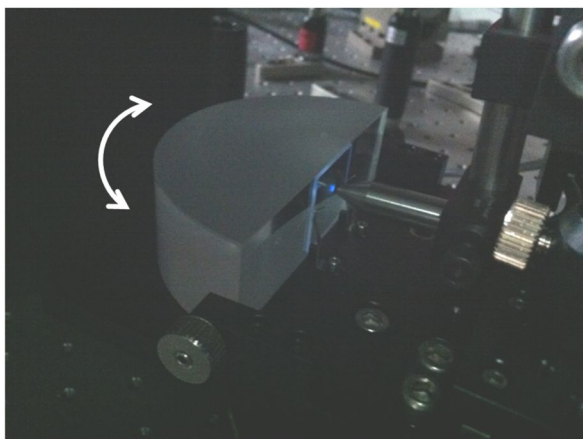


**Figure C.1.** (a) Schematic diagram and (b) photograph of the angle dependent PL measurement set-up.

## **Appendix D. EL measurement Set-up**

The current-voltage characteristics and the light output power of the devices were measured using a source measurement unit (Keithley 237) and a photodiode (Newport Model 818-UV) connected to an optical power meter (Newport Model 1835-C). Electroluminescence intensity of each sample was measured using an integrating sphere (Labsphere Co., 6" diameter) in order to detect all the light emitted in the forward direction from the device. The device was attached to a port of the integrating sphere where the glass side was facing toward the inside of the integrating sphere. The angle dependence of the EL intensity was measured by a photo-spectrometer (PR650) in every 5 degrees of the viewing angle.

## 초 록

유기발광다이오드는 다양한 모바일 전자기기에 성공적으로 응용되고 있다. 유기발광다이오드의 내부 효율은 많은 연구를 통해 이론적 한계치인 100%에 이르고 있지만 추출 효율은 20-30%에 머무르고 있어 조명, 일반 전자제품 등 유기발광다이오드의 상용화를 위해서는 추출 효율 향상을 위한 연구가 필요하다.

본 연구에서는 투명 전극과 기판 사이에 나노구조물을 삽입하는 방법을 통해 웨이브가이드로 인한 손실모드를 추출함으로써 유기발광다이오드의 효율을 향상시키고자 하였다. 적용된 나노구조물은 실린더 형태의 저굴절률 물질이 주기적으로 배열되어 있고 고굴절률 물질이 그 사이를 채우고 있어 굴절률이 다른 두 물질의 규칙적인 반복으로 이루어지는 광결정층이다. 이런 굴절률의 주기적인 반복은 유기발광다이오드 내부에서 발생한 빛을 산란시켜 소자 내부에서 사라지는 빛을 공기 중으로 나올 수 있게 한다. 유기발광다이오드의 효과적인 광추출에는 광결정층의 회절세기가 가장 지배적인 역할을 하는데 회절세기를 극대화하기 위해서 굴절률이 가장 낮은 상태인 진공 상태의 주기 배열을 사용하였다. 일반적인 과정으로는 유전물질에 진공 상태의 주기 배열을 형성할 수 없기 때문에 먼저 고굴절률 물질에 주기 구조를 형성하고 최종적으로 사용될 기판에 트랜스퍼하는 방식을 새롭게 개발하여 회절세기가 극대화된 광결정층을 성공적으로 구현하였다. 한편 소자의 전극 특성은 표면 상태에 민감하므로 낮은 표면 조도는 전기적인 특성에 매우 중요하다. 본 연구에서 개발된 방법은 극대화된 회절 세기를 가질 뿐 아니라 동시에 수 옴스트롱 스케일에 이르는 매끄러운 표면 조도를 갖는 광결정층을 형성한다. 이러한 광결정층이 적용된 유기 발광 다이오드는 전기적인 특성을 변화시키지 않으면서 약 2배에 이르는 효율 향상을 보였으며 광결정층의 효율 향상 효과는 각도별 광발광 측정과 유한 요소 시간 영역법을 이용한 맥스웰 방정식 계산에 의하여 분석되었고 각 분석 방법들은 일관된 결과를 보였다. 또한

광결정층이 적용된 효율 향상 효과는 형광 발광체와 인광 발광체에 모두 효과적이었으며 이를 통하여 현재 보고된 배면 유기발광다이오드 중 가장 높은 효율을 얻을 수 있었다. 일반 소자의 2배에 이르는 효율 향상을 보이는 광결정의 특성은 추출 효율이 낮은 일반 유기발광다이오드의 문제점을 극복하고 여러가지 정보 전달 장치뿐 만 아니라 일반 조명에도 이용가능한 해결점을 제시한다.

**주요어:** 유기발광다이오드(OLEDs), 광결정, 나노주기구조, 추출효율향상, 유한요소시간영역법(FDTD)

**학 번:** 2010-30181